43509

National Library of Canada
Bibliothèque nationale du Canada

CANADIAN THESES ON MICROFICHE

THÈSES CANADIENNES SUR MICROFICHE

NAME OF AUTHOR/*NOM DE L'AUTEUR* BENJAMIN ANOSIKE NWACHUKWU

TITLE OF THESIS/*TITRE DE LA THÈSE* FLOW AND EROSION NEAR GROYNE-LIKE STRUCTURES

UNIVERSITY/*UNIVERSITÉ* UNIVERSITY OF ALBERTA

DEGREE FOR WHICH THESIS WAS PRESENTED/ *GRADE POUR LEQUEL CETTE THÈSE FUT PRÉSENTÉE* PhD

YEAR THIS DEGREE CONFERRED/*ANNÉE D'OBTENTION DE CE GRADE* 1979

NAME OF SUPERVISOR/*NOM DU DIRECTEUR DE THÈSE* DR. N. RAJARATNAM

Permission is hereby granted to the NATIONAL LIBRARY OF CANADA to microfilm this thesis and to lend or sell copies of the film.

The author reserves other publication rights, and neither the thesis nor extensive extracts from it may be printed or otherwise reproduced without the author's written permission.

L'autorisation est, par la présente, accordée à la BIBLIOTHÈQUE NATIONALE DU CANADA de microfilmer cette thèse et de prêter ou de vendre des exemplaires du film.

L'auteur se réserve les autres droits de publication; ni la thèse ni de longs extraits de celle-ci ne doivent être imprimés ou autrement reproduits sans l'autorisation écrite de l'auteur.

DATED/*DATÉ* July 12 1979 SIGNED/*SIGNÉ*

PERMANENT ADDRESS/*RÉSIDENCE FIXÉ* IFE-EZINIHITTE, VIA NBAWSI
IMO STATE, NIGERIA

NL-91 (3-74)

National Library of Canada
Cataloguing Branch
Canadian Theses Division
Ottawa, Canada
K1A 0N4

Bibliothèque nationale du Canada
Direction du catalogage
Division des thèses canadiennes

NOTICE

The quality of this microfiche is heavily dependent upon the quality of the original thesis submitted for microfilming. Every effort has been made to ensure the highest quality of reproduction possible.

If pages are missing, contact the university which granted the degree.

Some pages may have indistinct print especially if the original pages were typed with a poor typewriter ribbon or if the university sent us a poor photocopy.

Previously copyrighted materials (journal articles, published tests, etc.) are not filmed.

Reproduction in full or in part of this film is governed by the Canadian Copyright Act, R.S.C. 1970, c. C-30. Please read the authorization forms which accompany this thesis.

THIS DISSERTATION
HAS BEEN MICROFILMED
EXACTLY AS RECEIVED

AVIS

La qualité de cette microfiche dépend grandement de la qualité de la thèse soumise au microfilmage. Nous avons tout fait pour assurer une qualité supérieure de reproduction.

S'il manque des pages, veuillez communiquer avec l'université qui a conféré le grade.

La qualité d'impression de certaines pages peut laisser à désirer, surtout si les pages originales ont été dactylographiées à l'aide d'un ruban usé ou si l'université nous a fait parvenir une photocopie de mauvaise qualité.

Les documents qui font déjà l'objet d'un droit d'auteur (articles de revue, examens publiés, etc.) ne sont pas microfilmés.

La reproduction, même partielle, de ce microfilm est soumise à la Loi canadienne sur le droit d'auteur, SRC 1970, c. C-30. Veuillez prendre connaissance des formules d'autorisation qui accompagnent cette thèse.

LA THÈSE A ÉTÉ
MICROFILMÉE TELLE QUE
NOUS L'AVONS REÇUE

NL-339 (3/77)

THE UNIVERSITY OF ALBERTA

FLOW AND EROSION NEAR GROYNE-LIKE STRUCTURES

by

© BENJAMIN A. NWACHUKWU

A THESIS
SUBMITTED TO THE FACULTY OF GRADUATE STUDIES
AND RESEARCH IN PARTIAL FULFILMENT OF
THE REQUIREMENTS FOR THE DEGREE OF
DOCTOR OF PHILOSOPHY

DEPARTMENT OF CIVIL ENGINEERING
UNIVERSITY OF ALBERTA
EDMONTON, ALBERTA

FALL, 1979

UNIVERSITY OF ALBERTA

FACULTY OF GRADUATE STUDIES AND RESEARCH

The undersigned certify that they have read, and recommend to the Faculty of Graduate Studies for acceptance, a thesis entitled, "FLOW AND EROSION NEAR GROYNE-LIKE STRUCTURES", submitted by BENJAMIN A. NWACHUKWU in partial fulfilment of the requirements for the degree of Doctor of Philosophy.

Dr. N. Rajaratnam, Supervisor

Professor A.W. Peterson

V. Galay
Dr. V. Galay

J Shaw.
Dr. J. Shaw

Ben C Yen
Dr. B.C. Yen
External Examiner
University of Illinois
Urbana, Illinois

Date 10 July 1979

ABSTRACT

Groynes are widely used in various tasks of river training but adequate knowledge of the flow characteristics near the structure is very much lacking. In this work which is exploratory and experimental in nature, the characteristics of the time averaged flow near a groyne placed in a rectangular, fixed bed channel, is studied. The erosion process near the groyne is also studied in the hope of relating the erosion phenomenon to the observed flow characteristics.

The velocity and shear stress fields near the groyne were satisfactorily mapped using a three-tube yaw probe. The velocity field was analysed by splitting it into a deflected region and a shear layer. In the deflected region, the velocity profiles were treated as a skewed turbulent boundary layer and analysed by the polar plot model of Johnston. The velocity defects for the profiles were found to be similar and the scales for this similarity profile were empirically determined. The boundary of the shear layer was not vertical; it was tilted inwards from the upper to the lower flow levels. However, all the shear layer profiles were satisfactorily analysed by the similarity technique.

The shear stress showed a considerable increase near the nose and immediate neighbourhood of the groyne. The maximum shear stress amplification, τ_o/τ_{oo} occurred at the groyne nose and the value depended on the constriction, b/B. For $b/B = 0.17$, $\tau_o/\tau_{oo} \simeq 5.0$, and for $b/B = 0.08$, $\tau_o/\tau_{oo} \simeq 3.0$. The shear stress field was analysed also by the similarity technique.

Maximum depth of scour occured near the groyne nose. The development of scour depth was shown to be similar in time when expressed in proper dimensionless forms. For larger part of their growth $\varepsilon_m \alpha \log t$. The scour progressed to the zone of low shear stress upstream of the groyne, by the process of undermining and slumping.

It is recommended that further experiments be carried out to cover a wider range of b/B.

ACKNOWLEDGEMENTS

The author wishes to express his sincere gratitude to Dr. N. Rajaratnam who suggested this topic, guided the research and made available, many hours for discussions with the author on technical matters relating to this work.

The data acquisition scheme was designed by R. Gitzel. Professor A.W. Peterson provided the initial interest in developing the data acquisition scheme and supported it financially through a grant from the National Research Council and the Department of Civil Engineering, University of Alberta. Contributions by S. Lovell, A. Muir and B. Klein in the design and construction of electronic and mechanical works is recognized. Other laboratory equipments were constructed by S. Lovell, and D. McGowan and maintained by them throughout the course of study. J. Lewis, B. Berry and P. Steffler assisted with the computer programming.

The author received financial support from the National Research Council through a grant to Dr. Rajaratnam and also from the Alberta Environment. These are gratefully acknowledged.

TABLE OF CONTENTS

		Page
TITLE PAGE		i
APPROVAL SHEET		ii
ABSTRACT		iii
ACKNOWLEDGEMENTS		v
TABLE OF CONTENTS		vi
LIST OF FIGURES		ix
LIST OF TABLES		xii
NOTATIONS		xiii
CHAPTER 1	INTRODUCTION	1
1.1	General	1
1.2	Previous Studies on Flow Near Groynes	4
1.3	Aim of Present Work	7
1.4	Form of Presentation	7
CHAPTER 2	EQUIPMENT AND EXPERIMENTAL PROCEDURE	9
2.1	General	9
2.2	The Flume	9
2.3	Velocity Measurements	13
2.4	Shear Stress Measurment	16
2.5	Equivalent Grain Roughness, k_s	23
2.6	Preston Tube in Pressure Gradient Flows	24
2.7	Instrument Correction	25
2.8	Yaw Probe Used as Preston Tube	25
2.9	Other Measuring Devices	28
2.10	Data Acquisition System	28
2.11	Test Procedure	32
2.12	Outline of Experimental Conditions	43

Page
2.13 Dimensional Analysis 43
CHAPTER 3 EXPERIMENTAL RESULTS AND ANALYSIS 46
3.1 Experimental Results 46
3.1.1 Velocity Data 46
3.1.2 Shear Stress Data 54
3.1.3 Shear Layer Data 62
3.1.4 Water Surface Data 62
3.2 Analysis of Experimental Results 68
3.2.1 Approach Flow 68
3.2.2 The Skewed Boundary Layer 70
3.2.2.1 The Polar Plot Model 70
3.2.2.2 The Velocity Defect 77
3.2.2.3 The Upper Potential Flow Layer 77
3.2.3 Bed Shear Stress Field 85
3.2.3.1 Similarity of Shear Stress Curves 85
3.2.3.2 Shear Stress Amplification Along Various Transverse Locations 86
3.2.3.3 Angle of the Shear Stress 89
3.2.4 The Shear Layer 89
3.2.4.1 Geometry of the Eddy Zone 92
3.2.4.2 Similarity of Velocity Profiles in the Shear Layer 95
3.2.5 Effect of Groyne Shape 99
3.3 Energy Consideration 102
3.4 Summary 103

Page

CHAPTER 4 AN EXPLORATORY STUDY OF EROSION NEAR GROYNES 104

4.1 Introduction and Literature Review 104

4.2 Regime-Type Formulas 105

4.3 Formulas Based on Dimensional Analysis 106

4.4 Analogy to Long Constriction 107

4.5 Aim of Present Work 108

4.6 Experimental Equipment 109

4.7 Experimental Procedure 110

4.8 Experimental Results 113

4.9 Visual Observation of Scour Process 120

4.10 Analysis of Experimental Results 121

4.10.1 Variation of ε_m with Time 121

4.10.2 Cross-Section and Geometry of the Scour Hole 123

4.10.3 The Equilibrium Depth of Erosion, $\varepsilon_{m\infty}$ 127

4.11 Summary 128

CHAPTER 5 CONCLUSIONS AND RECOMMENDATIONS 131

5.1 Summary 131

5.2 Conclusions 131

5.3 Recommendations 133

LIST OF REFERENCES 135

APPENDIX A THEORETICAL FREE STREAM LINE THEORY 141

LIST OF FIGURES

Figure Page

1.1 Schematic Illustration of Flow Around Obstructions 2

1.2 Design Variations for Groynes 3

1.3 Schematic Velocity Profiles for Three-Dimensional Boundary Layer 6

2.1 No. 36 Wet-or-Dry Aluminum Oxide Cloth 11

2.2 Rubber Hemisphere Roughness 12

2.3(a & b) Yaw Probe and its Calibration Curves 14

2.4 Calibration Curves for Preston Tube 22

2.5 Calibration Curves for Yaw-Type Preston Tube 27

2.6 The Traverse System 30

2.7 Recording Units 31

2.8 Data Acquisition System Block Diagram 33

2.9 Data Acquisition - Applications Program (TCOS) 34

2.10 Documentation of the Applications Program 36

2.11 Definition Sketch and Test Stations 41

3.1 Velocity Profiles in the Approach Flow 47

3.2(a) Velocity Profiles Near a Groyne (Expt. A1, Upstream) 48

(b) Velocity Profiles Near a Groyne (Expt. A1, Downstream) 49

3.3(a) Vertical Distribution of the Angles of Velocity Vector (Expt. A1, Upstream) 50

(b) Vertical Distribution of the Angles of Velocity Vector (Expt. A1, Downstream) 51

3.4 Polar Plots in Skewed Boundary Layer (Expt. A1) 53

Figure Page

3.5(a) Bed Shear Stress Plots (Series A Expts.) 55
(b) Bed Shear Stress Plots (Series B, C, D Expts.) 56
(c) Bed Shear Stress Plots (Series E Expts.) 57
3.6(a & b) 58
Variation of τ_{ox} and τ_{oz} (Expt. A1)
3.7(a) Contour Plot for τ_o (Expt. A1) 59
(b) Contour Plot for τ_o (Expt. D1) 60
(c) Contour Plot for τ_o (Expt. E1) 61
3.8 Velocity Profiles in Shear Layer (Expt. A1) 63
3.9 Detailed Velocity Profiles in Shear Layer (Expt. A4) 64
3.10 Velocity Profiles in Shear Layer (Expts. C1, D1) 65
3.11 Typical Water Surface Profile 66
3.11b Water Surface Topography 67
3.12 Dimensionless Velocity Profiles for the Approach Flow 69
3.13 Stream Lines Near a Groyne 71
3.14 Law of the Wall in the Inner Layer 73
3.15 Velocity Defect Profiles in Skewed Flow 74
3.16 Behaviour of the Characteristic Angles in Skewed Flow 75
3.17 Turning Angle of Shear Stress 76
3.18 Behaviour of the Velocity Defect Scale 78
3.19 Velocity of the Upper Layer (Series A) 80
3.20 Combined Upper Layer Velocity Profiles 81
3.21 Velocity of the Upper Layer (Series B) 82
3.22 Angle of the Deflected Flow (Series A) 83
3.23 Angle of the Deflected Flow (Series B) 84
3.24 Behaviour of Excess Bed Shear Stress 87

Figure Page

3.25 Similarity Curves and Scales for Excess Bed Shear Stress 88

3.26 (a to c) Turning Angles for the Bed Shear Stress 90

3.26(d) Variation of Maximum Turning Angle of Bed Shear Stress 91

3.27 Definition Sketch for Shear Layer 93

3.28 Boundaries of the Shear Layer 94

3.29(a) Similarity of Velocity Profiles for the Shear Layer (Upper Layer) 96

(b) Similarity of Velocity Profiles for the Shear Layer (Lower Layer) 97

3.30 Width of the Shear Layer 98

3.31(a) Velocity Profile (Expt. E1, Upstream) 100

(b) Velocity Profiles (Expt. E1, Downstream) 101

4.1 Scour Profile - Sample Output from X-Y Recorder 111

4.2 Velocity Profiles for the Approach Flow 114

4.3 Dimensionless Velocity Profiles 115

4.4 Variation of Scour Depth with Time 116

4.5 Time Sequence of Scour Development (Expt. 6) 117

4.6 Scour Hole Contour at Equilibrium State 118

4.7 Profiles of Scour Hole at Equilibrium State 119

4.8 Similarity of Scour Depth Development 122

4.9 Time Scale for Scour Depth Development 124

4.10 Similarity and Scale of Scour Profiles $\varepsilon_{\infty z}$ 125

4.11 Similarity of Scour Profiles $\varepsilon_{\infty x}$ 126

4.12 Criterion for Equilibrium Scour Depth 129

A1 Transformation for Flow Through a Nozzle 142

A2 Theoretical Free Stream Lines 144

LIST OF TABLES

Table		Page
2.1	Summary of Experiments on Rigid Bed	42
4.1	Summary of Scour Experiments	112

NOTATIONS

B - width of channel

constant in logarithmic velocity equation

B_s - constant in logarithmic velocity equation for Nikuradse's equivalent sand grain roughness

b - length of groyne

b_* - length scale

c - coefficient

c^* - empirical constant

D - median size of particle

d - probe diameter

F - Froude number

F_b - Blench's bed factor

f - general functional relation

- Lacey's silt factor

g - acceleration due to gravity

h - height of groyne

- total head

h_o - piezometric head

Δh - differential head; $(h - h_o)$

K - coefficient

k - height of roughness elements

k_s - Nikuradse's equivalent sand grain roughness

m - exponent

N - limit of $u_* k_s/\nu$

n - exponent

p - total pressure

p_o - static pressure

Δp - differential pressure $(p - p_o)$

Δp_* - dimensionless pressure parameter $\frac{\Delta p\ d^2}{4\rho\nu^2}$

Q - total discharge

Q' - discharge for a stream tube

q - unit discharge

q_s - unit sediment discharge

R - Reynold's number

r - exponent

t - time

t_* - time scale

U - velocity of the upper flow layer in the deflected region

- local velocity in the shear layer

U_d - velocity defect

U_{dm} - maximum value of U_d

U_m - maximum value of U for shear layer analysis $[U-(-u_b)]$

U_o - velocity of the upper flow layer for the approach flow

u - time averaged local velocity in x-direction

u_* - shear velocity

u_{*c} - critical shear velocity

u_{*o} - value of u_* in the approach length

u_b - maximum value of backward velocity

V - mean approach velocity

w - fall velocity

w - transverse component of velocity in z-direction

x - coordinate in longitudinal direction

x_m - location of maximum shear stress

x' - $x - x_m$

$(\frac{x'}{b})_{1/2}$ - length scale

$\overline{x}'$ - distance from groyne to upstream lip of scour hole

y - coordinate direction normal to bed

y_o - depth of flow

y_* - value of y at the apex of polar plot.

$y_{,}$ - distance from hypothetical datum to top of roughness element

z - coordinate direction normal to wall

z_i - distance from flume side wall to the inner edge of shear layer

z' - transverse distance from groyne nose $(z - b)$

$\overline{z}$ - transverse distance from the outer edge of shear layer

$\overline{z}'$ - wide of scour hole along z - direction

$\overline{z}_o$ - length scale for shear layer

α - constriction ratio $\frac{B-b}{b}$

- deflection angle of the upper flow layer

α_m - maximum deflection angle

α_* - empirical constant

β - angle of the defect velocity

ε - scour depth

ε_m - maximum scour depth (transient state)

$\varepsilon_{m\infty}$ - maximum scour depth (equilibrium state)

ε_∞ - scour depth at equilibrium state

γ - unit weight of water

ρ - mass density of water

ρ_s - mass density of sediment particle

$\Delta\rho$ - $\rho_s - \rho$

Δ - parameter $(\nu/\rho\ u_*^3$

κ - Von Karman's coefficient

μ - dynamic viscosity of water

ν - kinematic viscosity of water

δ - boundary layer thickness

τ_c - critical shear stress

τ_{oo} - approach bed shear stress

τ_o - bed shear stress in the deflected flow region

τ_{om} - maximum bed shear stress

τ_{ox} - longitudinal component of shear stress

τ_{oz} - transverse component of shear stress

τ_{o*} - dimensionless shear stress $\frac{\tau_o d^2}{4\rho\nu^2}$

$\Delta\tau_o$ - $\tau_o - \tau_{oo}$

$\Delta\tau_{om}$ - $\tau_{om} - \tau_{oo}$

η_τ - dimensionless length $\frac{x'/b}{(x'/b)_{1/2}}$

η_z - dimensionless length $\bar{z}/\bar{z}_o$

θ - angle of the velocity vector with x-direction

ω - angle of the inner layer

ψ - stream line

ϕ - energy dissipation rate

CHAPTER 1

INTRODUCTION

1.1 General

Groynes are structures projecting from the bank into a stream. They have been used for many years to guide flows, improve navigation channels and to protect banks from erosion caused by flow concentration. Other names often adopted for the structure are "spurs","spur dykes","jetties" or "transverse dykes". The existing knowledge on the flow pattern near a groyne-like obstruction in shear flows is largely qualitative. As shown in Figure 1.1, the flow approaching the structure tends to separate from the wall at some upstream point SP under the influence of an adverse pressure gradient generated by the obstruction. The separated flow is reattached to the structure but separates again from the boundary. The location of this second separation point is influenced by the obstruction geometry. If the obstruction has a sharp edge, such as a groyne made by sheet piling, the flow separates at the tip [Figure 1.1(b)]; for other groyne geometries the flow separates anywhere on the body surface before the rear stagnation point [Figure 1.1(a)]. At some downstream location RP, the flow reattaches to the wall again. The zone enclosed by the separated flow surface and the bank or flume wall is referred to as the "eddy zone". Outside the eddy zone, in the immediate neighbourhood of the groyne, the flow is speeded up as a result of channel constriction, and tends to be strongly three-dimensional. The disturbance thus caused by the obstruction could result in local scour in some flow zones, and siltation in the eddy zone. River engineering literature shows many and varied groyne designs. Common design variations

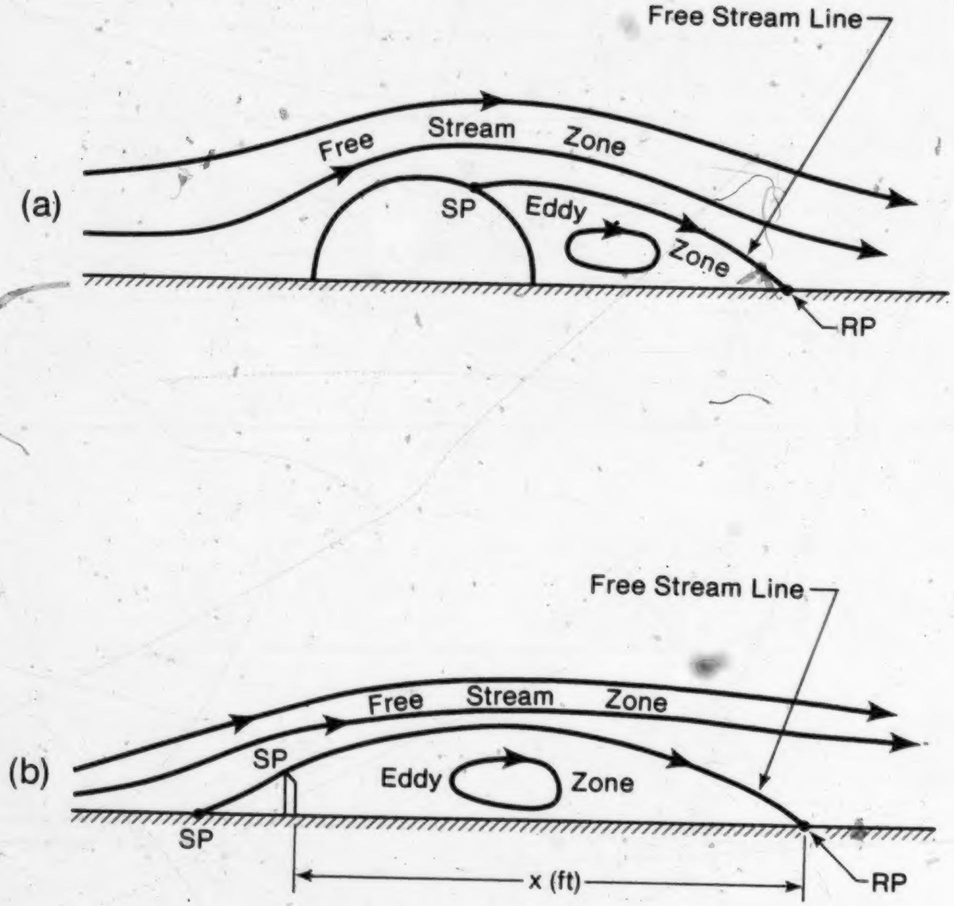
Free Stream Line
Free
Stream
Zone
(a)
SP
Eddy
Zone
RP
Free Stream Line
Free
Stream
Zone
(b)
SP
Eddy
Zone
SP
x (ft)
RP

Figure 1.1 Schematic Illustration of Flow Around Obstructions

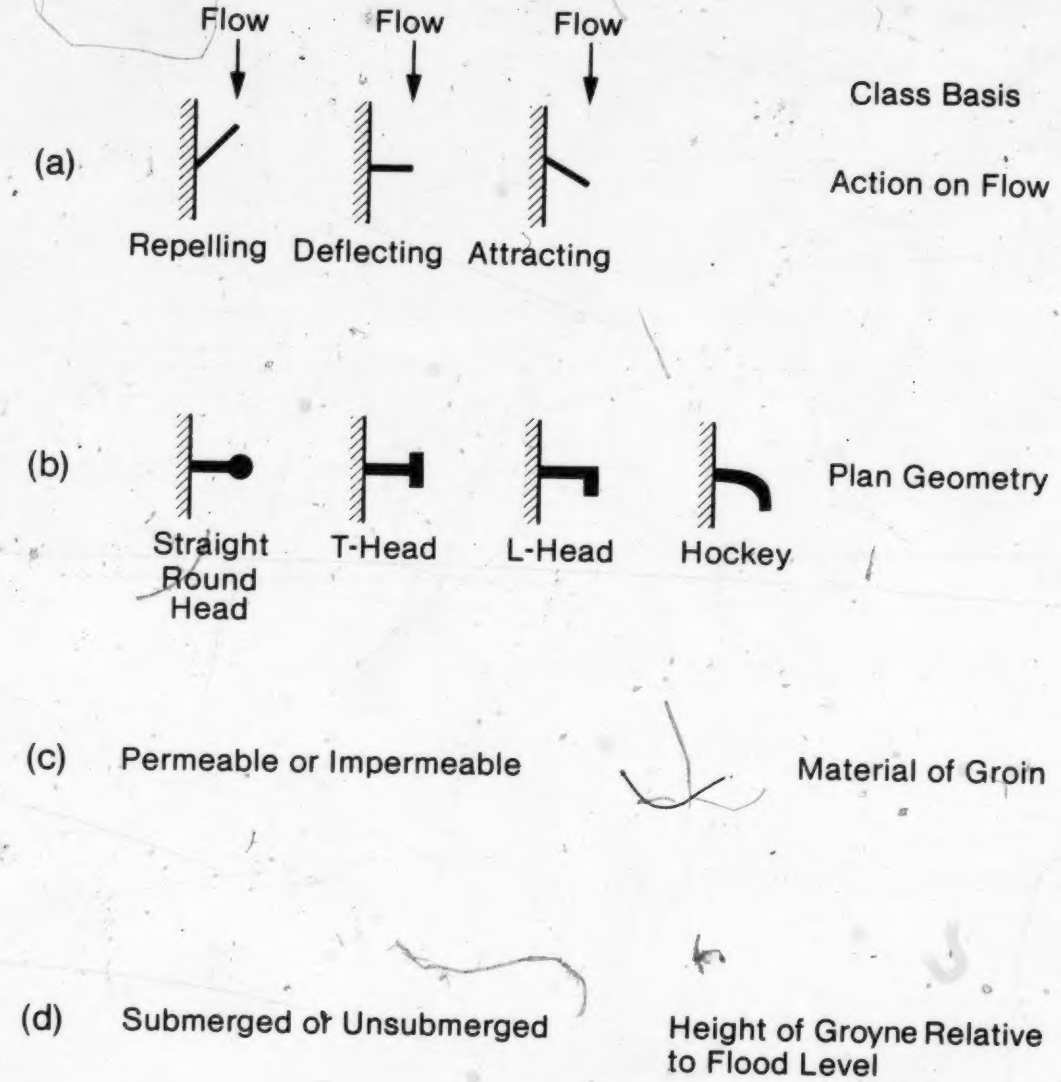
Flow
Flow
Flow
Class Basis
(a)
Action on Flow
Repelling
Deflecting
Attracting
(b)
Plan Geometry
Straight Round Head
T-Head
L-Head
Hockey
(c)
Permeable or Impermeable
Material of Groin
(d)
Submerged or Unsubmerged
Height of Groyne Relative to Flood Level

Figure 1.2 Design Variations for Groynes

are shown in Figure 1.2. Beckstead (1978) presented an excellent summary of the rational for the different designs. It would appear that the different orientations and plan geometry are attempts to control the scour and siltation patterns near the structure.

Even though many experimental studies have been performed to observe the erosion near groynes and express the results in dimensionless forms thereby developing empirical methods of predicting scour in the vicinity of groynes, comparatively very little work appears to have been done to understand the nature and structure of the turbulent flow near groynes. Consequently, the design of groynes has been an empirical art and relies very much for their success on the experience of the designer.

The impact on the river due to the presence of groynes is a question often imposed on the engineer by both environmentalists and owners of properties near a groyne project. The purely empirical methods available for the design of groyes cannot provide full answers to these concerns. Better understanding of the nature of the flow near groynes will help develop not only more general methods of predicting the erosion or deposition around groynes but also will throw more light on flow and erosion around other structures like bridge piers and abutments, and provide a sound basis for assessing the impact of groynes on the river system.

1.2 Previous Studies on Flow Near Groynes

In general, very little has been done to understand the characteristics of flow near obstructions (such as bridge piers, abutments or groynes) in rivers. Recently however, some effort has been made towards mapping the velocity, pressure and shear stress fields near bridge piers. Hjorth (1975) and Melville (1975) presented some interesting experimental results for the flow near bridge piers. Some observations of flow pattern in the eddy zone behind groynes were undertaken by Francis, Pattanaik and Wearne (1968) in a study to account for accretion near a similar structure projecting from an estuary bank. Zaghloul and McCorquodale (1973) presented a mathematical model for the vorticity distribution near a groyne.

The structure of flow around obstructions has been studied to some extent in wind tunnels. It is well recognized that the boundary layer near obstructions behaves three-dimensionally. The methods that have been used to solve these three-dimensional boundary layer problems could possibly be divided into two general groups. In the first group, the Navier-Stokes equations of motion are adopted with simplifying assumptions. Even in their simplified forms, the equations of motion contain many unknown variables. The behaviour of these variables is assumed in order to solve the equations. This method has not been very successful because it entails many unverified assumptions. In the second group, the velocity profiles are studied and described in terms of fundamental parameters such as bed shear stress, pressure distribution, fluid properties and boundary layer thickness. Figure 1.3(a) shows a typical isometric representation of a three-dimensional mean velocity profile. A two-dimensional representation of the velocity profiles can be made by separately plotting the magnitude and direction (relative to x-direction), of the velocity vectors as in Figure 1.3(b).

Johnston (1960) presented a "polar plot" of the three-dimensional boundary layer mean velocity profile. For this model, the velocity

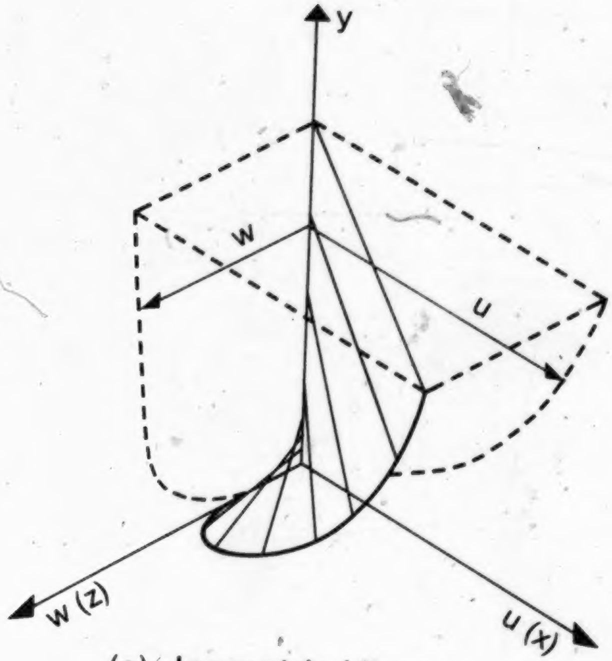

(a) Isometric View

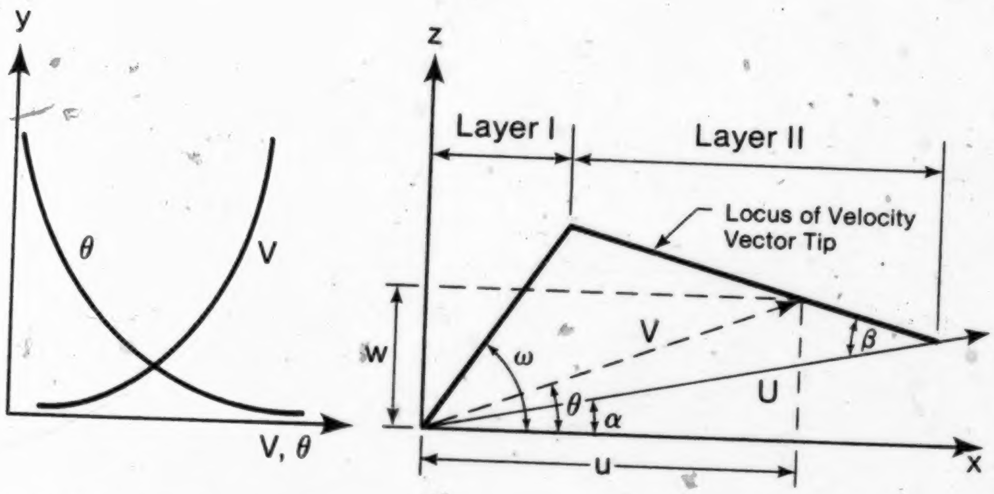
y
θ
V
V, θ
z
Layer I
Layer II
Locus of Velocity Vector Tip
w
ω
V
β
θ
α
U
u
x

(b) 2-Dimensional Plot

(c) The Triangular Model of Johnston

Figure 1.3 Schematic Velocity Profiles for Three-Dimensional Boundary Layer

vector (w) in the z-direction is plotted against the velocity vector (u) in the longitudinal x-direction. He found that the tip of the velocity vectors follows two straight lines as shown schematically in Figure 1.3(c). In a thin layer close to the bed (Layer 1) the velocity vectors are collinear and in the direction of the bed shear stress. Above this layer, the velocity vectors continuously turn relative to the wall shear vector. Referring to Figure 1.3(c), Johnston found that $\beta = 2\alpha$ and that at the apex of the triangle $yu_*/\nu \approx 16$, where u_* is the shear velocity. Johnston's model has been found to be valid for a three-dimensional boundary layer near a circular cylinder. (Hornung and Joubert, 1963).

1.3 Aim of Present Work

The principal aim of this study is to explore experimentally the characteristics of the time-averaged turbulent flow near thin plate groynes projecting perpendicularly into a fully developed turbulent flow in a long rectangular channel. A secondary objective is to study the process of erosion near a groyne and to explain it in the light of the observed flow characteristics.

1.4 Form of Presentation

Chapter 2 of this thesis outlines the experimental procedure, measurement techniques and data acquisition scheme developed for the study.

In Chapter 3, the experimental results and analyses for all measurements in the fixed bed flume are presented.

Chapter 4 deals with scour near groynes. It contains a short review of past studies, data obtained for the present study, and analyses based on the present and readily available data from the literature.

General summary, conclusion and recommendation for further study are given in Chapter 5.

CHAPTER 2

EQUIPMENT AND EXPERIMENTAL PROCEDURE

2.1 General

This chapter describes the experimental procedures, equipment and an automatic data acquisition system developed for the study. The experiments were conducted in the T Blench Hydraulics Laboratory at the University of Alberta.

Initial experiments were performed manually but it soon became obvious that the manual operation would be very difficult and time consuming. Consequently, a totally automatic scheme was developed. Most of the experimental data were collected by the latter scheme. Experiments were carried out in both rigid and mobile beds using the same flume.

2.2 The Flume

The experiments were conducted in a straight tilting rectangular flume, 120 feet long, 3 feet wide and 2-1/2 feet deep. The side walls and floor of the flume were made of plywood. Plexiglass windows for visual observation were provided at intervals along the side walls. The floor and inside walls were covered with a smooth layer of fibreglass resin. Test reach was located in the downstream half of the flume.

The flume was mounted on six pairs of synchronized screws which were driven by an electric motor for slope adjustment. At the downstream end of the flume, a tail gate was installed which could be cranked up and down to regulate the depth of flow. Flow in the system was pumped from an underlying sump into the flume head tank through a 12-inch diameter delivery pipe. A regulating valve and flow measuring device were included in the delivery line. The flow measuring device consisted of an 8-inch Foxboro magnetic flow meter with a continuous recorder. This device was found convenient for assessing flow fluctuations during a run which often lasted several days.

Fixed Bed Tests

The objectives of these tests were:

1. To map the velocity and shear fields near an obstruction projecting from a side wall.
2. To determine the longitudinal and transverse extent of the eddy zone behind the obstruction.
3. To measure the afflux and drop in water level near the obstruction. This information could be used to assess the pressure field induced by the cantilevered obstruction.

Bed Roughness

Most of the testing was done in the flume with a plywood bed. To determine the effect of roughness, some runs were made in a bed covered with prefabricated uniform roughnesses. Two roughness sizes were used. These were:

1. No. 36 aluminium oxide wet-or-dry cloth manufactured by the 3M Company. Hollingshead (1972) determined the medium grain size for the cloth to be 0.00183 feet (0.56 mm.). The plan and sectional view of the cloth are

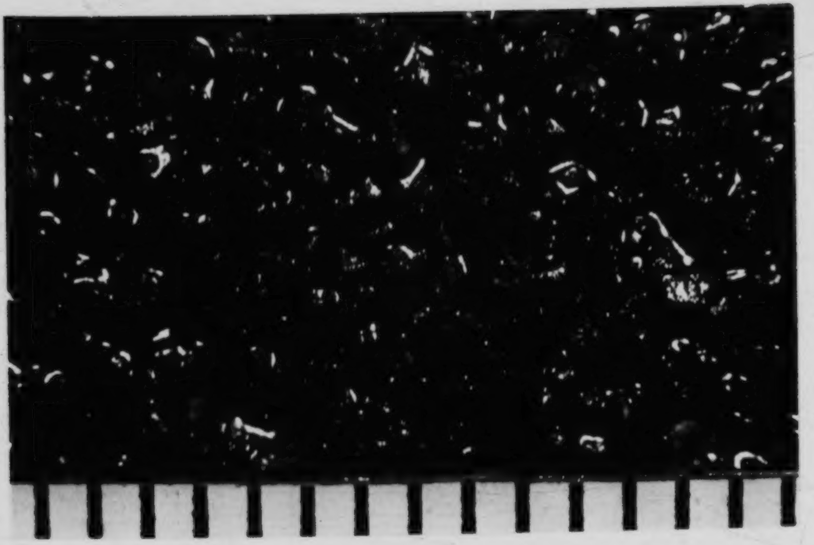

(a) Plan View (Scale in mm)

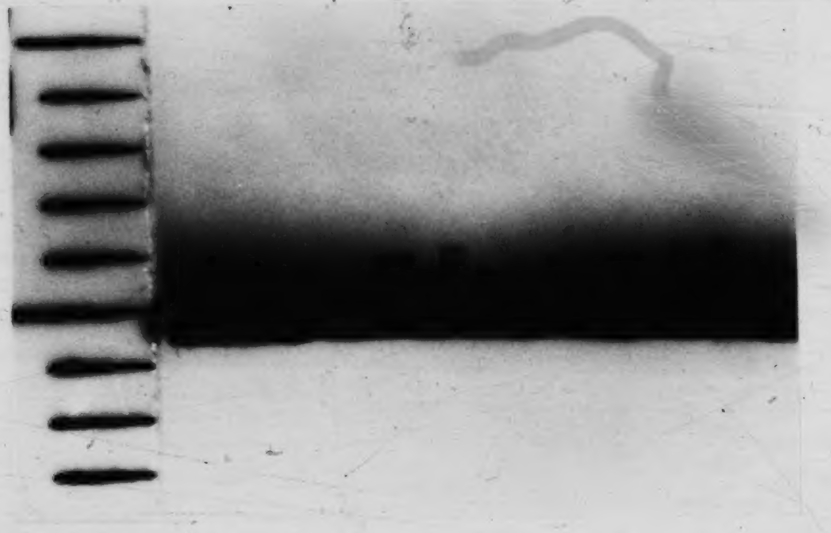

(b) Section View (Scale in mm)

Figure 2.1 No. 36 Wet-or-Dry Aluminum Oxide Cloth

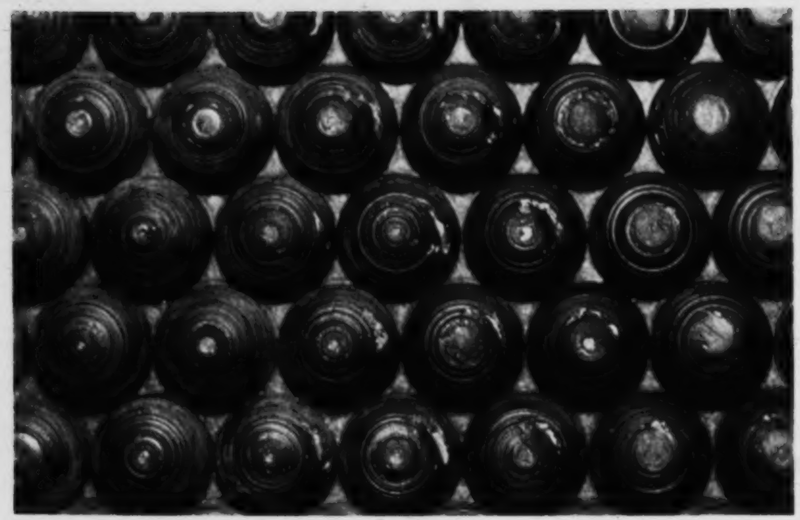

(a) Plan View

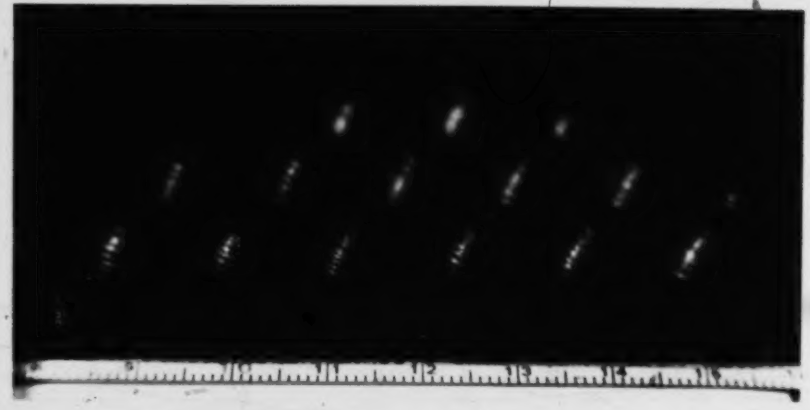

(b) Section View (Scale in cm)

Figure 2.2 Rubber Hemisphere Roughness

shown in Figure 2.1.

2. Closely packed half inch diameter hemispheres molded from hard rubber into rectangular sheets. The roughness height was 0.0208 feet (0.63 cm.). The plan and sectional view is shown in Figure 2.2.

2.3 Velocity Measurements

Flow velocities were measured using a three-tube yaw probe. This instrument was selected because it measured both the magnitude and direction of the velocity vector in the horizontal plane and the calibration curves for it were available in the laboratory. Rajaratnam and Muralidhar (1967) determined the calibration curves for this probe in a uniform velocity field and found the calibrations to be applicable in some shear flows.

The yaw probe was made of three lengths of stainless steel tubing of 3 mm. outer diameter/1.8 mm. inner diameter. The three tubes were rigidly soldered together and the vertical stem was further stiffened for added stability. The centre tube had a flat nose while the side tubes were chamferred at an angle of 45° as shown schematically in Figure 2.3(a).

Principles of the Yaw Probe

Consider a two-dimensional flow where the velocity vector, V, is in the horizontal plane at an angle of θ from a fixed reference direction. The total head indicated by the three tubes of the yaw probe could be written as:

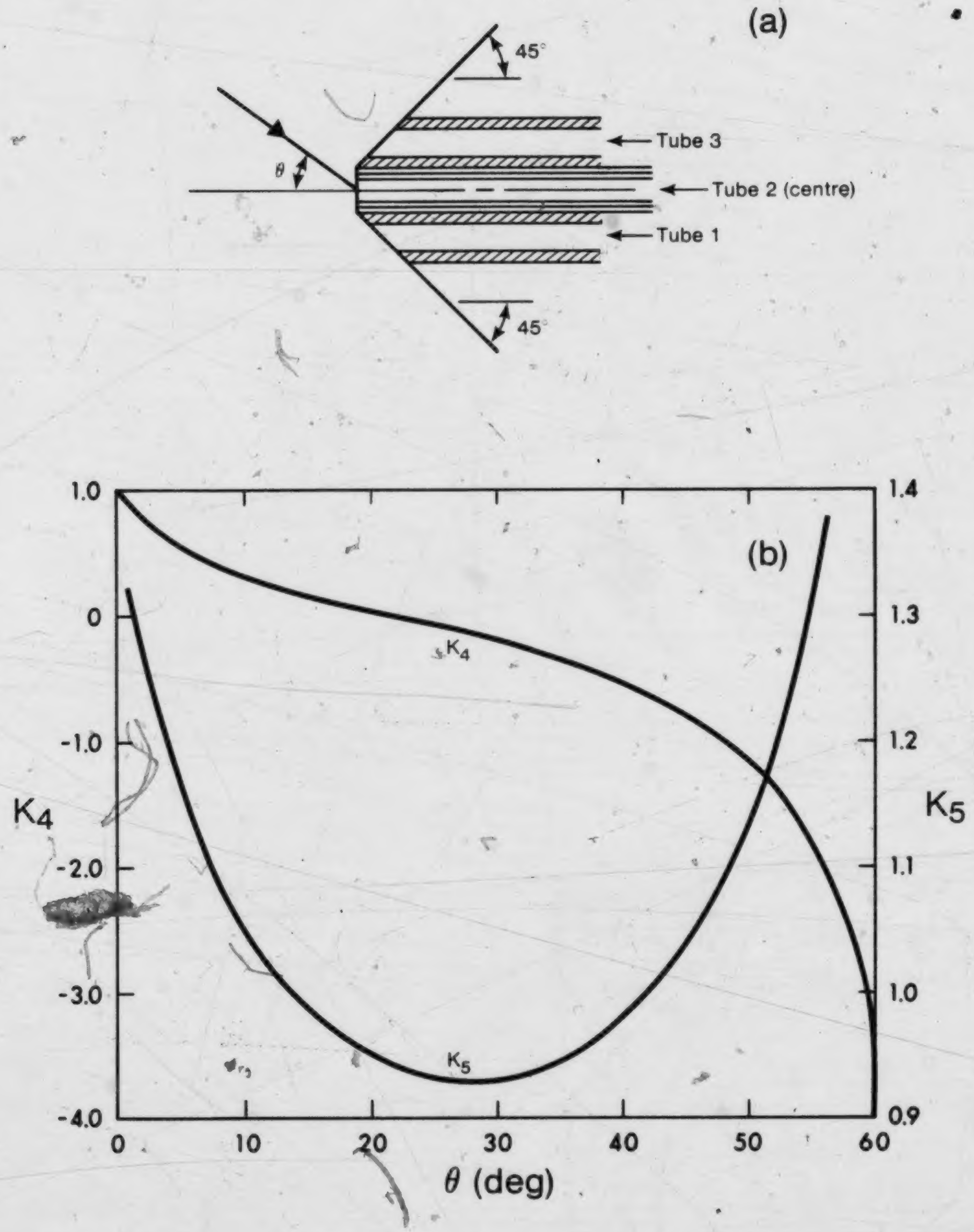

Figure 2.3 (a & b) Yaw Probe and its Calibration Curves

$$h_1 = h_0 + K_1 \frac{v^2}{2g}$$

$$h_2 = h_0 + K_2 \frac{v^2}{2g} \qquad (2.1)$$

$$h_3 = h_0 + K_3 \frac{v^2}{2g}$$

where K_1, K_2, K_3 are the calibration co-efficients and functions of only θ, neglecting viscous effects and other minor correction factors; suffix 2 corresponds to the centre tube, 3 represents the tube on the side of the velocity vector, and 1 is for the other outer tube; and h_0 is the piezometric head.

By rotating the yaw probe through known angles in a potential velocity field, it was possible to determine the calibration curves for K_1, K_2, and K_3. Using the three calibration factors, a fourth factor K_4 can be defined as:

$$K_4 = \frac{K_3 - K_2}{K_1 - K_2} \qquad (2.2)$$

or from equation 2.1:

$$K_4 = \frac{h_3 - h_2}{h_1 - h_3} \qquad (2.3)$$

The variation of K_4 with θ as determined by Rajaratnam and Muralidhar (1967) is shown in Figure 2.3(b). Thus equation 2.3 in combination with Figure 2.3(b) gives the angle of the velocity vector. Further, from equation 2.1, it can be shown that:

$$V = \frac{\sqrt{2g(h_1 - h_2}}{\sqrt{K_1 - K_2}} \tag{2.4}$$

or

$$V = K_5\sqrt{2g\Delta h} \tag{2.5}$$

where

$$K_5 = \frac{1}{\sqrt{K_1 - K_2}} ; \; \Delta h = h_1 - h_2$$

Again, K_5 is only a function of θ and its variation is shown in Figure 2.3(b). Figure 2.3(b) was digitized for computer application. Longitudinal and transverse components of velocity could be found by resolving the velocity vector.

Differential pressures between the two outer tubes and the central tube were measured with two Pace Model P90D differential pressure transducers equipped with a 0.03 psid. full scale diaphragm. The transducers were calibrated by applying static differential heads of zero to one inch of distilled water to the yaw probe and adjusting the indicator until a linear output of zero to 10 volts was achieved. The calibration was checked daily. The differential pressures were used to obtain velocities according to equation 2.5.

2.4 Shear Stress Measurement

In turbulent flows in open channels, the boundary shear stress distribution can be obtained by one of the following techniques:

1. Velocity profiling.
2. Direct shear measurement with a floating plate element.
3. The Preston tube.

Hollingshead (1972) presented a comprehensive review of these methods. The floating plate elements are usually fixed in one boundary location. Therefore, they are not appropriate for mapping the shear stress field. In this study most shear stress measurements were made by the Preston tube technique. In the approach flow, shear stress was determined by both the Preston method and the velocity profile method.

Velocity Profile Method

In the wall law region of a two dimensional turbulent flow over a rough boundary, the velocity profile is given as:

$$\frac{u}{u_*} = \frac{1}{\kappa} \ln \frac{y}{k} + B \qquad (2.6)$$

where B is a function of the roughness Reynolds number $(u_* k/\nu)$; u_* is the friction velocity; κ is the Von Karman constant (approximately equal to 0.4) and k is the roughness height. The relationship between B and $u_* k/\nu$ was evaluated by Nikuradse in his experiments with pipes which were coated with uniform sand grains. It is now customary to replace B and k by their equivalent sand grain roughness values of B_s and k_s respectively. According to Nikuradse, if $(u_* k_s/\nu \overset{\sim}{<} 3.5)$, the flow behaves as though the rough boundary is hydrodynamically smooth and:

$$B_s = 5.75 \log \frac{u_* k_s}{\nu} + 5.5 \qquad (2.7)$$

or

$$\frac{u}{u_*} = 5.75 \log \frac{yu_*}{\nu} + 5.5 \qquad (2.8)$$

and for rough boundary, $u_* k_s/\nu \overset{\sim}{>} 70$, the flow behaves as though the rough boundary is hydrodynamically rough, and

$$B_s = 8.5$$

or

$$\frac{u}{u_*} = 5.75 \log \frac{y}{k_s} + 8.5 \qquad (2.9)$$

From either of the equation 2.8, 2.9, the friction velocity and hence the shear stress is obtained as:

$$\sqrt{\frac{\tau_0}{\rho}} = u_* = \frac{1}{5.75} \left[\frac{u_2 - u_1}{\log(\frac{y_2}{y_1})} \right] \qquad (2.10)$$

where u_1 and u_2 are mean velocities at ordinates y_1 and y_2 respectively. The final equation is independent of B_s and k_s and applies for smooth and rough beds alike. However for large roughness elements, it is important to determine a correct reference datum for y. Usually, various datum planes are tried until a linear plot is obtained when the velocity u is plotted against log y. Einstein and El-Samni (1949) and Hollingshead (1972) found that for a surface consisting of closely packed hemispheres, this datum plane is located 0.2 diameter below the tops of the hemispheres.

Preston Tube Technique

Preston (1954) used similarity considerations and the existence of the law of the wall to develop a simple method for determining the local shear stress on a smooth boundary. The method uses a total head tube resting on the boundary.

In the 'law of the wall region' near the boundary, it is known that

$$\frac{u}{u_*} = f\left(\frac{u_* y}{\nu}\right) \tag{2.11}$$

Consider a total head tube of diameter d placed in this flow region. If p is the total pressure reading of the tube and p_0 is the static pressure at the boundary, then $\Delta p = (p - p_0)$ can be considered as the dependent variable relating to the independent variables ρ, ν, τ_0 and d. Consequently:

$$\frac{\Delta p d^2}{4\rho\nu^2} = f\left(\frac{\tau_0 d^2}{4\rho\nu^2}\right) \tag{2.12}$$

where ρ and ν are the mass density and kinematic viscosity of the fluid respectively. For hydrodynamically rough boundaries, the effect of viscosity could be neglected and the corresponding equation takes the form:

$$\frac{\Delta p}{\tau_0} = f\left(\frac{d}{k}\right) \tag{2.13}$$

where k is the roughness height.

A number of studies have been carried out to evaluate the functions of equations 2.12 and 2.13 and to test their applicability in pressure gradient flows. (Head and Rechenberg, 1962; Patel, 1965; Hollingshead, 1972). In this study, the calibration curves developed by Patel (1965) for the smooth boundary and by Hollingshead (1972) for rough boundaries are used. Patel's calibration equations are as follows:

for $\log \tau_{0*} < 1.5$

$$\log \tau_{0*} = \frac{1}{2} \log \Delta p_* + 0.037$$

for $1.5 \leq \log \tau_{0*} < 3.5$

$$\log \tau_{0*} = 0.829 - 0.138 \log \Delta p_* + 0.144 (\log \Delta p_*)^2 - 0.006 (\log \Delta p_*)^3 \tag{2.14}$$

for $3.5 \leq \log \tau_{0*} < 5.3$

$$\log \Delta p_* = \log \tau_{0*} + 2 \log (1.95 \log \tau_{0*} + 4.1)$$

where $\Delta p_* = \frac{\Delta p d^2}{4\rho\nu^2}$ and $\tau_{0*} = \frac{\tau_0 d^2}{4\rho\nu^2}$

The calibration for rough boundary as given by Hollingshead assumes Δp at the geometric centre of the boundary tube to be

$$\Delta p = \frac{1}{2} \rho u^2 \tag{2.15}$$

where u is the velocity at this level. Further, the normal distance y from the datum to the geometric centre of the tube is equal to (y' + d/2), where y' is the distance of the top of the roughness elements from the datum.

Since $\tau_0 = \rho u_*^2$, we have

$$\frac{\Delta p}{\tau_0} = \frac{1}{2} \left(\frac{u}{u_*} \right)^2 \tag{2.16}$$

Substituting in equation 2.9

$$\frac{\Delta p}{\tau_0} = \frac{1}{2} \left[5.75 \log \frac{1}{k_s} \left(\frac{d}{2} + y'\right) + 8.5\right]^2 \tag{2.17}$$

This equation gives the pressure to shear ratio in a fully rough flow. For the transition region, equation 2.17 can be written in its general form as

$$\frac{\Delta p}{\tau_0} = \frac{1}{2} \left[5.75 \log \frac{1}{k_s} \left(\frac{d}{2} + y'\right) + B_s\right]^2 \tag{2.18}$$

and according to Nikuradse,

$$\begin{aligned} &\text{for} \quad 3.5 < \frac{u_* k_s}{\nu} \leq 7.1; \; B_s = 3.5 \log \frac{u_* k_s}{\nu} + 6.59 \\ &\text{for} \quad 7.1 < \frac{u_* k_s}{\nu} \leq 14.1; B_s = 9.58 \\ &\text{for} \quad 14.1 < \frac{u_* k_s}{\nu} < 70; \; B_s = 11.5 - 1.62 \log \frac{u_* k_s}{\nu} \end{aligned} \tag{2.19}$$

Hollingshead determined the limiting values in the transition region by the relation

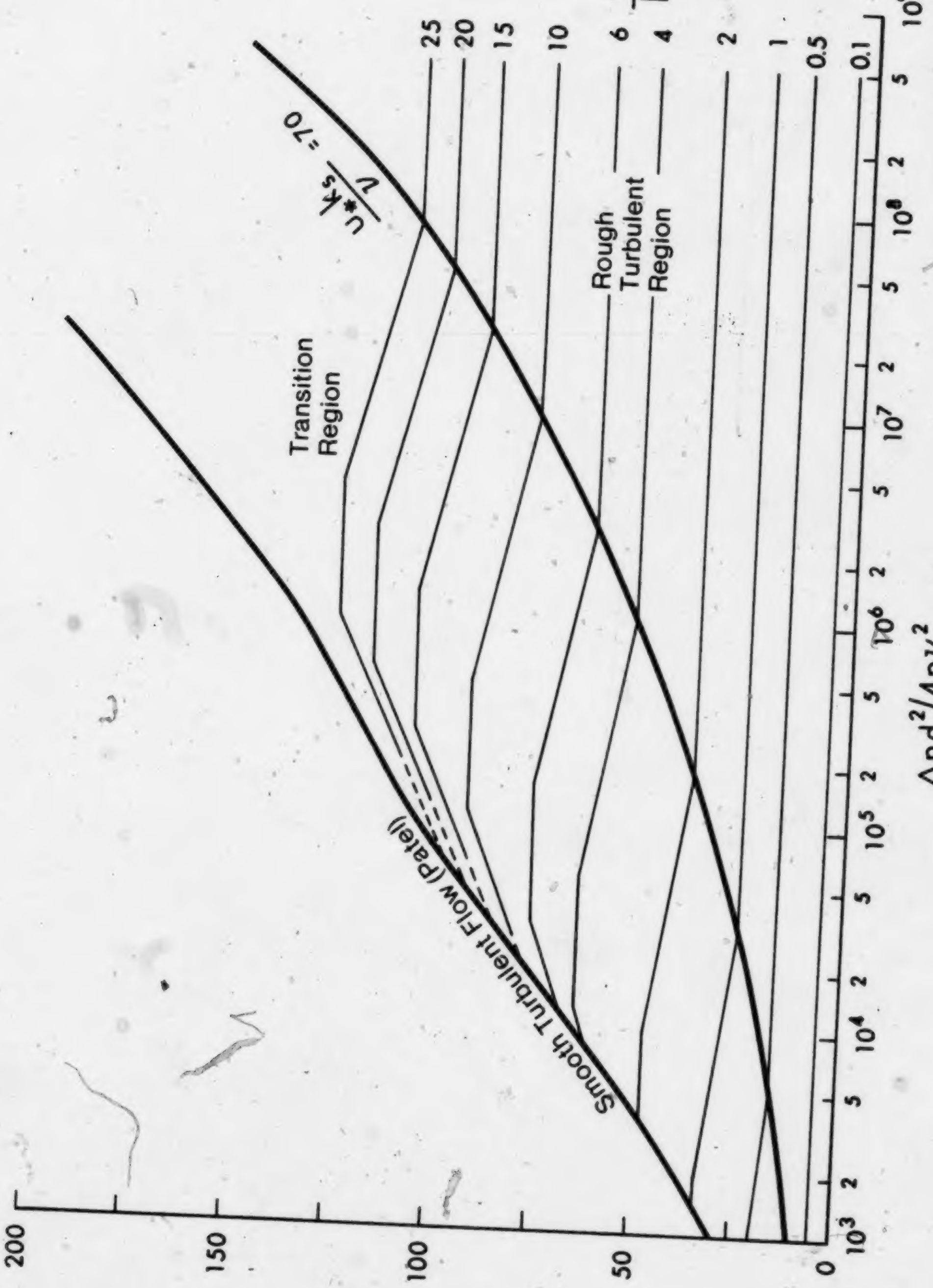

Figure 2.4 Calibration Curves for Preston Tube

$$\Delta p_* = \frac{\Delta p d^2}{4\rho\nu^2} = \frac{1}{4} N^2 \frac{\Delta p}{\tau_0} (\frac{d}{k_s})^2 \qquad (2.20)$$

where

$$N = \frac{u_* k_s}{\nu}$$

Equations 2.17 to 2.20 were used to develop the calibration curves of Figure 2.4.

2.5 Equivalent Grain Roughness, k_s

Equation 2.6 describing the law of the wall was given as

$$\frac{u}{u_*} = \frac{1}{\kappa} \ln \frac{y}{k} + B \qquad (2.21)$$

or

$$u = \frac{1}{\kappa} u_* \ln y + (Bu_* - \frac{1}{\kappa} u_* \ln k)$$

In general, k is a known quantity. Therefore, from a measured velocity profile it is possible to evaluate B. Rewriting equation 2.6 in terms of equivalent sand grain roughness, we have

$$\frac{u}{u_*} = \frac{1}{\kappa} \ln \frac{y}{k_s} + B_s \qquad (2.22)$$

By combining equations 2.21 and 2.22

$$\frac{k_s}{k} = e^{-\kappa(B-B_s)} \qquad (2.23)$$

where $B_s = 8.5$ and $\kappa = 0.4$

Thus k_s can be evaluated from velocity profile and equation 2.23.

2.6 Preston Tube in Pressure Gradient Flows

The principle of the Preston tube depends on the existence of the law of the wall. If the pressure gradients become large, it is generally recognized that the velocity distribution undergoes changes (Stratford, 1959; Patel, 1965; Perry and Joubert, 1965). Consequently, the Preston tube calibration would be expected to change. The severity of the pressure gradient as it affects the flow in the wall region is assessed by means of the parameter, $\Delta = \frac{\nu}{\rho u_*^3}\frac{dp_0}{dx}$ where $\frac{dp_0}{dx}$ is the pressure gradient. Patel (1965) empirically determined the limiting values of Δ for a Preston tube to record τ_0 within prescribed error ranges. These limits are as follows:

i. Adverse pressure gradients -

maximum error 3%: $0 < \Delta < 0.01, \frac{u_* d}{\nu} \leq 200$

maximum error 6%: $0 < \Delta < 0.015 \frac{u_* d}{\nu} \leq 250$

ii. Favourable pressure gradients -

maximum error 3%: $0 > \Delta > -0.005; \frac{u_* d}{\nu} \leq 200; \frac{d\Delta}{dx} < 0$

maximum error 6%: $0 > \Delta > -0.007; \frac{u_* d}{\nu} \leq 200; \frac{d\Delta}{dx} < 0$

In this study, it was approximately verified that the effect of pressure gradient could not introduce any errors above the limits due to general experimental errors.

2.7 Instrument Corrections

The Preston tube or Pitot tube placed near a boundary causes a displacement in the streamline impinging on it. For round Pitot tubes, it has been shown (McMillan, 1957) that the impinging streamline comes from a higher level thereby recording a higher impact pressure than the true value. For a three tube yaw probe, no correction estimate for flow displacement is available at this time.

Another correction to be considered is that due to turbulence. The corrections due to flow discplacement and turbulence are discussed by Montes and Ippen (1973). These corrections, however, were not applied in this study.

2.8 Yaw Probe Used as Preston Tube

The Preston tube technique is convenient for measuring the shear stress vector when its direction is known. By rotating the tube until the maximum dynamic pressure is recorded, it will still be possible to determine the magnitude and direction of the shear stress. But such processes will be tedious and time consuming. To overcome this difficulty in flows with large angles of yaw, Rajaratnam and Muralidhar (1968) suggested that the magnitude and direction of the boundary shear stress could be obtained by placing the conventional three tube yaw probe on the boundary and using it as a Preston tube. For this purpose, equation 2.1 is rewritten in terms of the total pressure recorded by each tube as

$$
\begin{aligned}
p_1 &= p_0 + K_{10}\Delta p \\
p_2 &= p_0 + K_{20}\Delta p \\
p_3 &= p_0 + K_{30}\Delta p
\end{aligned}
\qquad (2.24)
$$

where $\Delta p = (p-p_0)$; p is the total pressure indicated by Preston tube of equivalent diameter, K_{10}, K_{20}, and K_{30} are as previously defined but show some variation because of its placement on the boundary (see Figure 2.5). Substituting for Δp given in equation 2.12,

$$
\begin{aligned}
p_1 &= p_0 + K_{10}\,\frac{4\rho\nu^2}{d^2}\; f(\tau_*) \\
p_2 &= p_0 + K_{20}\,\frac{4\rho\nu^2}{d^2}\; f(\tau_*) \\
p_3 &= p_0 + K_{30}\,\frac{4\rho\nu^2}{d^2}\; f(\tau_*)
\end{aligned}
\qquad (2.25)
$$

where $\tau_* = \dfrac{\tau_0 d^2}{4\rho\nu^2}$

By manipulating equation 2.25, it could be shown that

$$\frac{p_3 - p_2}{p_1 - p_2} = \frac{K_{30} - K_{20}}{K_{10} - K_{20}} = K_{40} \qquad (2.26)$$

Figure 2.5 plots K_{40} versus the shear stress angle. From the first two expressions of equation 2.25, it could be shown that

$$\frac{(p_2 - p_1)\, d^2}{4\rho\nu^2} \cdot \frac{1}{K_{20} - K_{10}} = f(\tau_*) \qquad (2.27)$$

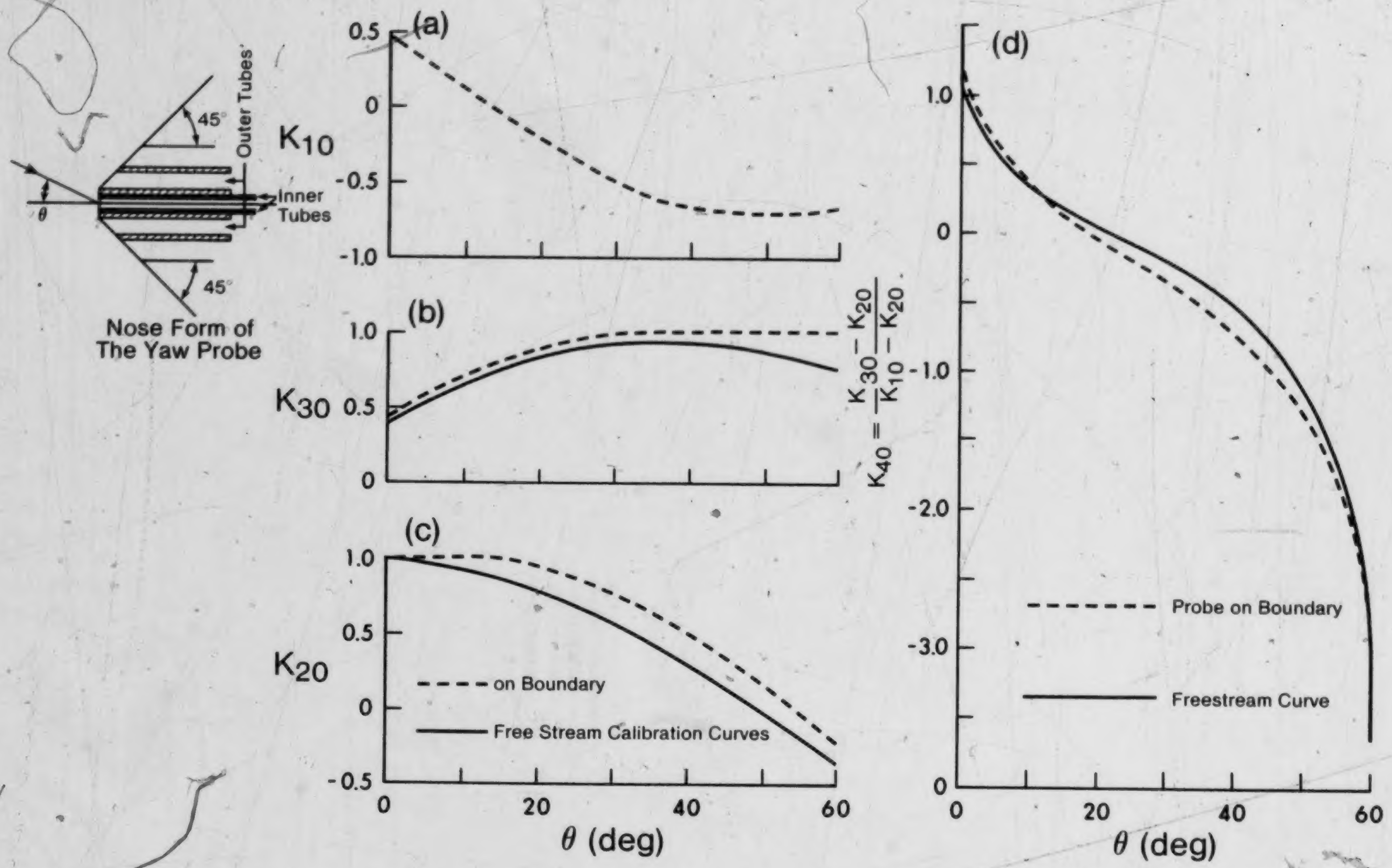

Figure 2.5 Calibration Curves for Yaw-Type Preston Tube

The calibration curves for K_{10}, K_{20} and K_{30} are given in Figure 2.5. Equation 2.27 provides an adjusted pressure term when a yaw probe is used as a Preston tube. Once this adjustment is applied, the Preston tube calibration previously discussed could be used to determine τ_0.

In an exploratory experiment, shear stress measurements were made using a yaw probe and a Preston tube, each having an external diameter of 3 mm. The results compared favourably. Detailed study of the shear stress field subsequently was made with the yaw probe.

2.9 Other Measuring Devices

Water surface profiles were measured using the water level detector. This instrument was developed at the University of Alberta, in the Department of Civil Engineering with co-operation of the Department of Electrical Engineering. The probe which has a tapered tip is raised or lowered at a fixed distance below the water level under the control of a servo-system. It was connected to an autograph recorder which could be calibrated to provide a convenient scale for the water level changes.

To establish an experimental run, a point gauge was used to measure the depth of flow at the approach length. The point gauge was equipped with a vernier scale which measured to the nearest 0.001 ft.

2.10 Data Acquisition System

Manual measurement of velocity and shear stress in such a sharply deflected flow as that considered in this work is tedious and time consuming because (1) these variables change significantly over short distances in space and entail measurement at a large number of points in order to track their apparent variation; (2) the use of a yaw probe requires simultaneous reading of two or three pressure gauges. To overcome these experimental difficulties, an automatic and programmable data acquisition system was developed for this study. Once activated, the system could run unattended for several days with occassional visits to change cassette tapes on which the data had been recorded and to check the transducer calibration.

The data acquisition system consisted of a control unit, traverse unit, logging and recording units. Data retrieval, analysis and plotting were performed using the larger computer systems. Details of the data acquisition system have been published earlier (See Nwachukwu et al, 1978).

The main component of the control unit is the SC/MP (Simple Cost-Efficient Microprocessor) which accepts a BASIC language programme,NIBL (National Industrial BASIC Language). The programme developed for this operation was referred to as TCOS (Traverse Control Operating System). Under the influence of TCOS, the control unit moves the probe to a specified location, activates the data logging unit and maintains a prescribed sequence of operation. The control unit was accessed through a TTY (teletype).

The traverse unit carried the yaw and other measuring probes to a designated station under the command of the programme on the control unit. To achieve accuracy and repeatability in locating a station, the traverse unit was made of precision components and fabricated to fine tolerances to minimize friction and backlash of moving parts. The traverse unit is shown in Figure 2.6.

The data logging unit used in the study is the Fluke 2240A.

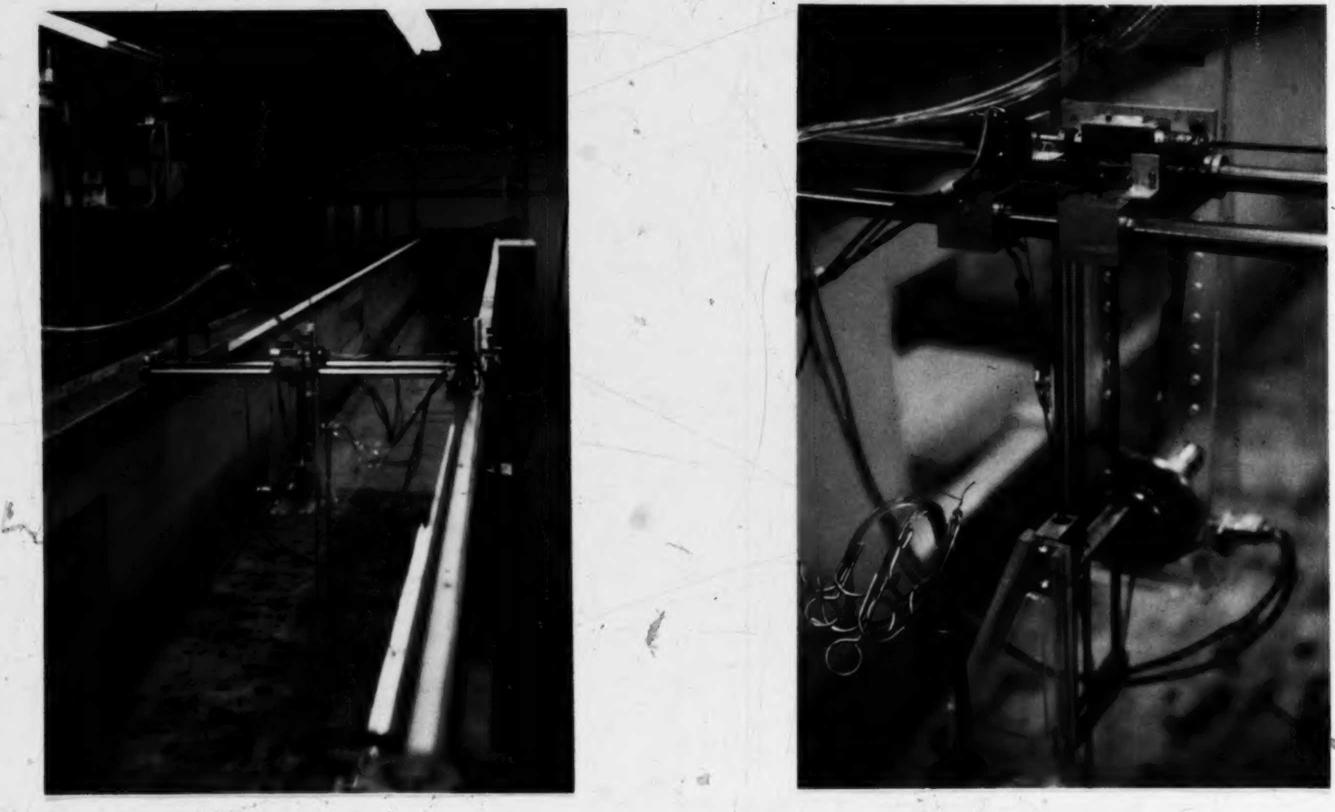

(a) Over View (b) Close-up View

Figure 2.6 The Traverse System

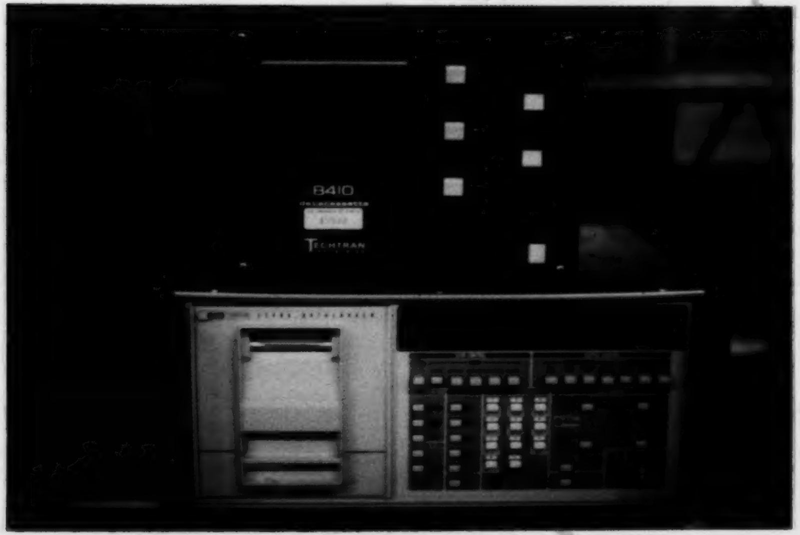

Figure 2.7 Data Logger (Below) and Cassette Recorder (Top)

Under the control of NIBL, the data logger scanned the analog signals from the transducers and traverse units. These signals were simultaneously digitized and transferred to a recording device. The recorder unit used was a digital cassette tape. Logging and recording units are shown in Figure 2.7. The serial data from the data logger was recorded at 300 baud and read back at 2400 baud to a mini-computer for processing. The processed data was transferred on-line to the University computer (Amdal 470) for plotting. Plotting was done on a calcomp plotter.

A block diagram for the experimental operation is shown in Figure 2.8. The programme TCOS, developed in this study is shown in Figure 2.9. The programme has eight legal modes which are explained in Figure 2.10. The application is "conversational" and all entries were made on the TTY attached to the control unit.

2.11 Test Procedure

For a selected test discharge, the flume slope and depth were adjusted to establish uniform flow conditions. The flow depth was adjusted using the tailgate located at the downstream end of the flume and the depth of flow was measured along the flume centreline near the test section, using a point gauge. Uniform flow was assumed when the measured depths of flow varied within ± 0.002 ft. of the mean value. The flow was then stopped and the groyne installed. The boundaries of the flume with the groyne were sealed to prevent leakage.

Test stations were established as shown in Figure 2.11. The (X,Z) co-ordinates and the bed elevations (referenced to an arbitrary datum) for each station was determined and fed into the data acquisition

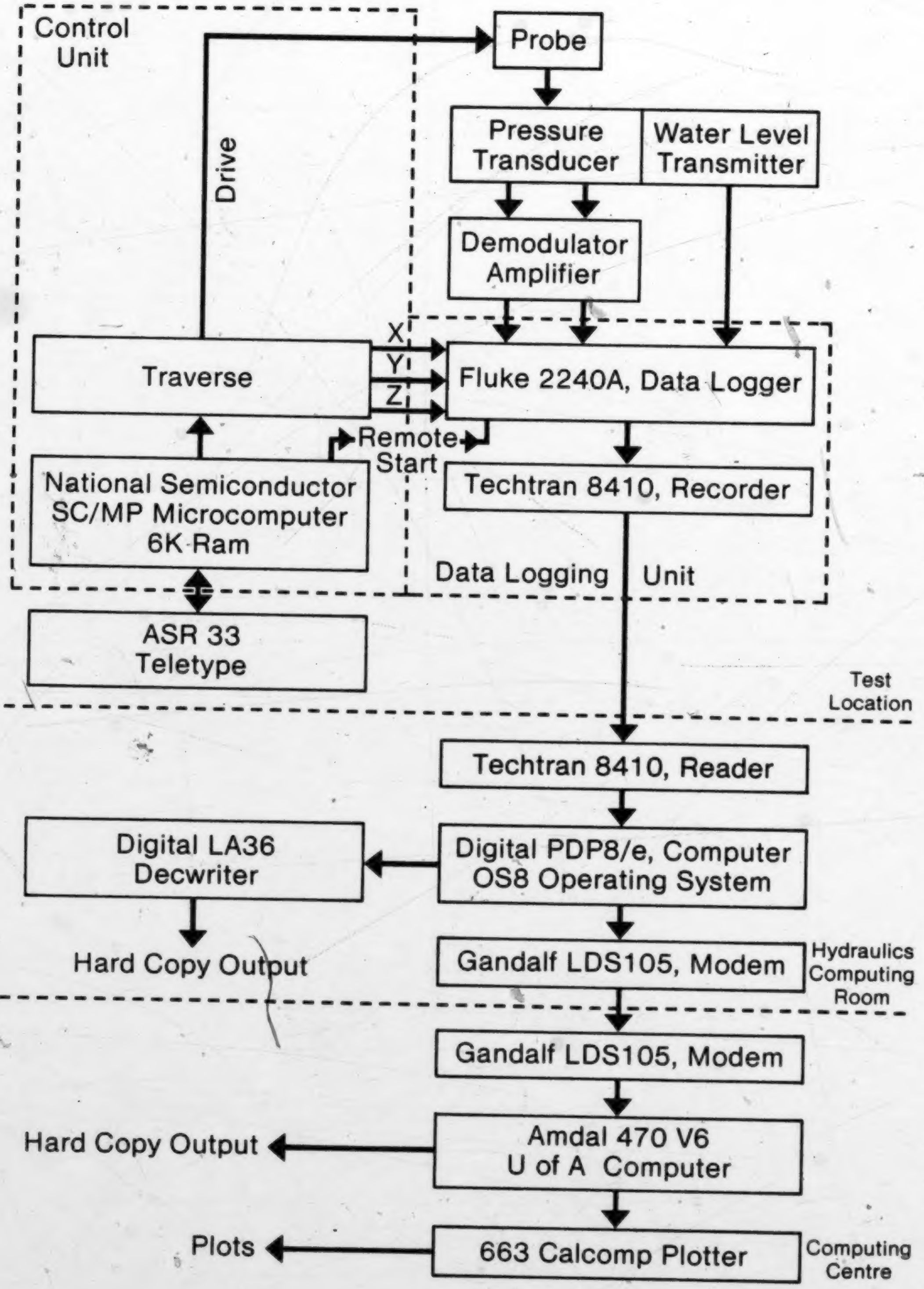
Control Unit
Drive
Probe
Pressure Transducer
Water Level Transmitter
Demodulator Amplifier
X
Y
Z
Traverse
Fluke 2240A, Data Logger
Remote Start
National Semiconductor SC/MP Microcomputer 6K Ram
Techtran 8410, Recorder
Data Logging Unit
ASR 33 Teletype
Test Location
Techtran 8410, Reader
Digital LA36 Decwriter
Digital PDP8/e, Computer OS8 Operating System
Hard Copy Output
Gandalf LDS105, Modem
Hydraulics Computing Room
Gandalf LDS105, Modem
Hard Copy Output
Amdal 470 V6 U of A Computer
Plots
663 Calcomp Plotter
Computing Centre

Figure 2.8 Data Acquisition System Block Diagram

Figure 2.9 Data Acquisition — Applications Program (TCOS)

```
05 X=#7FF:Y=#4FF:Z=#7FF:GOSUB 8000:GOSUB 8020:GOSUB 8040
10 PP "MOVE X,Y,Z AWAY FROM LIMITS"
15 PR "THEN ENTER 0";:INPUT O
45 PR "MODE";:INPUT P
50 IF (P<9)AND(P>0) GOTO 60
55 PR "ILLEGAL ENTRY":GOTO 5
60 GOSUB P*200:GOTO 45
200 PR "ENTER X,Y,Z (-1,-1,-1 TO STOP ) "
210 M=0:N=0:DO:PR N;:INPUT X,Y,Z
220 IF (X>-1) GOTO 240
230 M=M-1:RETURN
240 GOSUB 9000:M=M+1:N=M:UNTIL M=256
250 PR " YOU HAVE ENTERED TOO MANY POINTS"
260 RETURN
400 PR "ENTER POINT #,X,Y,Z ";:INPUT N,X,Y,Z
410 IF (N>=0)OR (N<=M) GOTO 430
420 PR "OUT OF RANGE (0 - ",M,")":GOTO 400
430 GOSUB 9000:RETURN
600 PR "ST AT";:INPUT G
610 FOR N=G TO M:GOSUB 9100:IF X=0 GOTO 620
620 GOSUB 8700:PR N," .-  ",X,Z:GOSUB 9500
625 GOSUB 9000
630 NEXT N:RETURN
800 PR "ENTER POINT # ";:INPUT N
810 IF (N>=0)OR(N<=M) GOTO 830
820 PR "OUT OF RANGE (0 - ",M,")":GOTO 800
830 PR "X,Z";:INPUT X,Z:GOSUB 8700:GOSUB 9500
840 GOSUB 9000:RETURN
1000 PR "ST,FIN";:INPUT G,H
1010 FOR N=G TO H:GOSUB 9100:PR N,"     ",X,Y,Z:NEXT N
1020 RETURN
1200 PR "ENTER NUMBER OF POINTS ";:INPUT M
1210 IF (M>=0)OR(M<=256) RETURN
1220 PR "NUMBER OF POINTS MUST BE <256 AND >=0":GOTO 1200
1400 PR "RUNS TO FILL CASSETTE ";:INPUT R:Q=0
1410 PR "POINT # TO TURN TO 45 DEGS";:INPUT G
1420 PR "POINT # TO TURN TO 135 DEGS";:INPUT H
1430 PR "FIRST,LAST POINT #";:INPUT I,J
1440 IF (I<16)OR(J>M) GOTO 1450:PR "ILL VALS":GOTO 1430
1450 PR "TURN PROBE TO 0 DEGS; ENTER 0 TO GO";:INPUT O
1460 FOR P=I TO J
1470 IF P=G GOSUB 7000
1480 IF P=H GOSUB 7100
1490 N=P:GOSUB 9100:IF X=0 GOTO 1570
1500 W=Y:GOSUB 8700:PR P,X,Y,Z;
1501 U=60
1510 GOSUB 7200:FOR E=0 TO 15:PR ".";
1520 N=E:GOSUB 9100:Y=Y+W:GOSUB 8020
1521 U=30
1530 GOSUB 7200:Q=Q+2:IF Q>(R-Q) GOSUB 9700
1540 FOR O=1 TO 2:PR "#";:@#2A00=0
1541 U=60
1550 GOSUB 7200:NEXT O
1560 NEXT E
1570 PR " ":NEXT P:RETURN
1600 FOR N=0 TO M:GOSUB 9100:PR X,",",Y,",",Z:NEXT N
1610 PR -1,",",-1,",",-1:RETURN
7000 PR "TURN PROBE TO 30 DEGS; ENTER 0 TO GO";:INPUT O:RETURN
7100 PR "TURN PROBE TO 180 DEGS; ENTER 0 TO GO";:INPUT O:RETURN
```

CONTD

```
7200 IF (STAT AND #10)=0 GOSUB 7300
7205 U=U*25:T=0:DO
7210 T=T+1:UNTIL T>=U: RETURN
7300 PR " ":PR "WAITING - ENTER 0 TO GO";:INPUT A:RETURN
8000 J=1:V=X:IF (X<100)OR(X>#FC0) RETURN
8010 GOTO 8050
8020 J=4:V=Y:IF (Y<0)OR(Y>#BC0) RETURN
8030 GOTO 8050
8040 J=16:V=Z:IF (Z<10)OR(Z>4080) RETURN
8050 @(#2C00+J)=V/256
8060 @(#2C00+(J*2))=V
8070 RETURN
8700 Y=512:GOSUB 8020
8710 GOSUB 8000
8720 GOSUB 8040
8730 RETURN
9000 A=#2000:V=X:GOSUB 9200
9010 A=#2200;V=Y:GOSUB 9200
9020 A=#2400:V=Z:GOSUB 9200
9030 RETURN
9100 X=@((N*2)+#2000)*256+@((N*2)+#2001)
9110 Y=@((N*2)+#2200)*256+@((N*2)+#2201)
9120 Z=@((N*2)+#2400)*256+@((N*2)+#2401)
9130 RETURN
9200 @((N*2)+A)=V/256:@((N*2)+A+1)=V:RETURN
9500 PR "DIR,AMT";:INPUT A,B:IF A=0 RETURN
9510 IF NOT((A<-1)OR(A>1)) GOTO 9520:PR "ILLEGAL DIR":GOTO 9500
9520 T=0
9530 T=T+1
9540 IF T>=20 GOTO 9500
9550 IF (NOT(STAT) AND #10)=0 GOTO 9530
9560 IF ((Y-A*B)>3000) OR ((Y-A*B)<0) GOTO 9520
9570 Y=Y-A*B:GOSUB 8020:GOTO 9520
9700 PR "CASSETTE FULL"
9710 PR "ENTER 0 TO GO";:INPUT O
9720 Q=0
9730 RETURN
9999 END
```

Figure 2.10 Documentation of the Applications Program

MODE 1 - NUMERICAL POINT ENTRY

THIS MODE ALLOWS ENTRY OF A SERIES OF POINTS AS NUMBERS WHICH IS REPRESENTED AS FOLLOWS:

X - LENGTH OF X AXIS/4095 AS UNIT; RANGE:100<X<4000
Y - LENGTH OF Y AXIS/4095 AS UNIT; RANGE:100<Y<4000
Z - LENGTH OF Z AXIS/4095 AS UNIT; RANGE:100<Z<4000

THE COMPUTER WILL ASK THE FOLLOWING QUESTION; FOLLOWED BY THE POINT NUMBER AND A REQUEST FOR A LIST OF VALUES FOR THE POINT:

```
ENTER X,Y,Z (-1,-1,-1 TC STOP )
0 ?
```

HERE YOU ENTER THE VALUES FOR X,Y AND Z SEPARATED BY COMMAS. YOU CAN ONLY SPECIFY 256 POINTS AND IF YOU ENTER TOO MANY, THE COMPUTER WILL PRINT OUT:

```
YOU HAVE ENTERED TOO MANY POINTS
```

AND THEN RETURN TO MODE SELECTION. TO STOP ENTERING POINTS, ENTER -1,0,0.

MODE 2 - NUMERICAL EDITING

THIS MODE ALLOWS YOU TO CHANGE THE VALUE FOR A SINGLE POINT. UPON ENTERING 2 TO MODE, THE FOLLOWING IN WRITTEN:

```
ENTER POINT #,X,Y,Z?
```

TO THIS, A POINT NUMBER, AN X VALUE, A Y VALUE, AND A Z VALUE ARE ENTERED SEPARATED BY COMMAS. THE POINT NUMBER MUST BE ONE OF THE POINTS CURRENTLY ENTERED AND IF A POINT NUMBER GREATER THAN THE LAST ENTERED POINT IS GIVEN, THE FOLLOWING IS WRITTEN:

```
OUT OF RANGE (0 - XXX)
```

WHERE XXX IS THE LARGEST POINT NUMBER. YOU WILL THEN BE REASKED THE FIRST QUESTION. IF YOU NEED TO ADD POINTS, SEE MODE 6.

MODE 3 - Y ENTRY BY DAC

MODE 3 IS BASICALLY AN EXTENSION OF MODE 1 USED TO ALLOW THE SELECTION OF Y VALUES WITH THE PUSH BUTTON TO ALLOW ALIGNMENT OF Y BY SIGHT.

THE COMPUTER WILL PROMPT FOR THE START POINT NUMBER FOR POINT EDITING:

```
ST AT?
```

AT THIS POINT ENTER THE POINT NUMBER AT WHICH YOU WISH TO CHANGE Y VALUES.

THE COMPUTER WILL TELL YOU THE CURRENT POINT NUMBER AND X AND Z:

```
NNNN  -  XXXX ZZZZZ
```

CONTD

WHERE NNNN IS THE CURRENT POINT NUMBER
XXXX IS THE X VALUE AT THIS POINT
ZZZZ IS THE Z VALUE AT THIS POINT

NOW, A VALUE FOR Y MUST BE SELECTED. THIS IS DONE BY THE USE OF A PUSH BUTTON WHICH CAN BE FOUND NEAR THE TELETYPE. THE WILL ASK YOU:

```
DIR,AMT?
```

BY WHICH IS MEANS, DIRECTION OF Y TRAVEL(1 IS DOWN AND -1 IS UP, WHERE DOWN IS TOWARD THE BED OF THE FLUME) AND THE AMOUNT OF CHANGE IN Y, IN Y UNITS AS EXPLAINED IN MODE 1. THE COMPUTER WILL THEN PULSE THE Y AXIS BY THE AMOUNT SPECIFIED EVERY TIME THE BUTTON IS PRESSED OR CONTINUOUSLY IF THE BUTTON IS HELD DOWN. IF THE BUTTON IS RELEASED FOR ABOUT 5 SECONDS, YOU WILL RETURN TO THE "DIR,AMT?" QUESTION FOR NEW VALUES.

TO STOP ADJUSTING Y, ENTER 0,0 AND THE NEXT POINT WILL BE SELECTED. AFTER ALL POINTS ARE DONE, THE PROGRAM WILL RETURN TO MODE.

<u>MODE 4</u> - DAC EDIT MODE

THIS MODE IS USED TO EDIT POINTS BUT TO MAKE USE OF THE PUSH BUTTON FACILITY TO SELECT A Y VALUE BY SIGHT ALIGNMENT. THIS MODE IS BASICALLY IDENTICAL TO MODE 2 EXCEPTING THAT A VALUE FOR Y MUST SELECTED BY NON-NUMERICAL METHODS.

UPON ENTERING MODE 4, THE FOLLOWING PRINTED:

```
ENTER POINT #?
```

WHICH REQUESTS THE POINT NUMBER TO BE CHANGED, WHICH MUST BE ONE OF THE POINTS CURRENTLY ENTERED AND IF A POINT NUMBER GREATER THAN THE LAST ENTERED POINT IS GIVEN, THE FOLLOWING IS WRITTEN:

```
OUT OF RANGE (0 - XXX)
```

WHERE XXX IS THE LARGEST POINT NUMBER. YOU WILL THEN BE REASKED THE FIRST QUESTION. IF YOU NEED TO ADD POINTS, SEE MODE 6.

THEN YOU MUST ENTER A VALUE FOR X AND Z WHICH IS REQUESTED BY:

```
X,Z?
```

NOW, A VALUE FOR Y MUST BE SELECTED. THIS IS DONE BY THE USE OF A PUSH BUTTON WHICH CAN BE FOUND NEAR THE TELETYPE. THE WILL ASK YOU:

```
DIR,AMT?
```

BY WHICH IS MEANS, DIRECTION OF Y TRAVEL(1 IS UP AND -1 IS DOWN, WHERE DOWN IS TOWARD THE BED OF THE FLUME) AND THE AMOUNT OF CHANGE IN Y, IN Y UNITS AS EXPLAINED IN MODE 1. THE COMPUTER WILL THEN PULSE THE Y AXIS BY THE AMOUNT SPECIFIED EVERY TIME THE BUTTON IS PRESSED OR CONTINUOUSLY IF THE BUTTON IS HELD DOWN. IF THE BUTTON IS RELEASED FOR ABOUT 5 SECONDS, YOU WILL RETURN TO THE "DIR,AMT?" QUESTION FOR NEW VALUES.

TO STOP ADJUSTING Y, ENTER 0,0 AND YOU WILL BE RETURNED TO MODE.

CONTD

MODE 5 - PRINT LISTING OF POINTS

THIS MODE WILL PRINT OUT A LIST OF ALL THE CURRENTLY SET POINT NUMBERS AND THEIR VALUES FOR X, Y, AND Z IN THAT ORDER.

THE PROGRAM WILL THEN ASK FOR THE POINT NUMBERS FOR THE START AND FINISH OF THE LISTING:

```
     ST,FIN?
```

TO WHICH YOU REPLY WITH THE START AND FINISH POINT NUMBERS.

MODE 6 - RESELECT MAXIMUM NUMBER OF POINT

THIS COMMAND ALLOWS FOR THE EXPANSION OF THE CURRENT SET OF POINTS BUT REQUIRES SPECIFYING THE POINT VALUES WITH THE NUMERICAL EDIT OR DAC EDIT MODES.

UPON ENTRY TO THIS MODE, THE FOLLOWING IS PRINTED:

```
   ENTER NUMBER OF POINTS?
```

TO WHICH YOU REPLY WITH THE NUMBER OF POINTS IN THE POINTS BUFFER, THAT IS, THE NUMBER OF POINTS. THE MAXIMUM NUMBER POINTS IS 255, AND THE MINIMUM IS 0. ENTRY OF ANY OTHER VALUE WILL RESULT IN THE FOLLOWING MESSAGE:

```
   NUMBER OF POINTS MUST BE <256 AND >=0
```

AND WILL ASK YOU FOR THE NUMBER OF POINTS AGAIN.

MODE 7 - DO SAMPLING RUN MODE

THIS MODE IS THE MODE WHICH ALLOWS THE COMPUTER TO EXECUTE A RUN AND SAMPLE DATA. THERE ARE SEVERAL PIECES OF DATA NEEDED TO ALLOW THIS SECTION TO RUN CORRECTLY AND THESE ARE ASKED FIRST.

THE NUMBER OF ACTIVATIONS OF THE FLUKE TO FILL CASSETTE:

```
   RUNS TO FILL CASSETTE?
```

THE NUMBER OF THE POINT AT WHICH THE PROBE IS TO BE TURNED TO 45 DEGREES:

```
   POINT # TO TURN TO 30 DEGS?
```

THE NUMBER OF THE POINT AT WHICH THE PROBE IS TO BE TURNED TO 135 DEGREES:

```
   POINT # TO TURN TO 180 DEGS?
```

THEN A REQUEST FOR INITIAL POINT NUMBER IS GIVEN:

```
  FIRST, LAST POINT #?
```

ENTER THE STARTING AND FINISHING POINT FOR THIS RUN. IF YOU ENTER A START LESS THAN 16 OR A FINISH GREATER THAN THE NUMBER OF POINTS ENTERD, THE FOLLOWING ERROR MESSAGE WILL BE PRINTED

```
   ILL VAL
```

AND YOU WILL BE ASKED FOR NEW VALUES.

THEN A REQUEST IS PRINTED TO TURN PROBE TO 0 DEGREES TO START:

```
   TURN PROBE TO 0 DEGS; ENTER 0 TO GO?
```

CONTD

AT THE APPROPRIATE TIME, THE FOLLOWING MESSAGES WILL BE PRINTED WITH THE SAME MEANING AS THE ABOVE:

```
   TURN PROBE TO 30 DEGS; ENTER 0 TO GO?

   TURN PROBE TO 180 DEGS; ENTER 0 TO GO?
```

WHEN THE CASSETTE IS FILLED THE FOLLOWING IS PRINTED:

```
   CASSETTE FULL
   ENTER 0 TO GO?
```

AT ANY POINT IN THE RUN, HOLDING THE PUSH BUTTON DOWN WILL STOP THE PROGRAM JUST PRIOR TO A TIMING POINT. THIS MEANS THAT THE WAIT WILL DEPEND ON THE AMOUNT OF DELAY YOU HAVE IN YOUR PROGRAM. THE FOLLOWING MESSAGE WILL BE PRINTED:

```
   WAITING - ENTER 0 TO GO?
```

AND UPON ENTERING 0, THE PROGRAM WILL CONTINUE.

NOTE ALSO THAT A POINT WHICH HAS A ZERO X VALUE WILL BE SKIPPED.

MODE 8 PUNCH OUT POINTS LIST

THIS MODE IS USED TO PREPARE A LIST OF POINTS IN A FORMAT THAT WILL ALLOW REENTRY OF POINTS USING MODE 1. THE BASIC DIFFERENCE BETWEEN THIS MODE AND MODE 5 (LIST POINTS) IS THAT MODE 5 ALSO PRINTS THE POINT NUMBER AND DOES NOT INCLUDE THE ESSENTIAL COMMAS USED TO SEPARATE THE X, Y, AND Z OF THE POINT.

TO USE THIS MODE

1) AT MODE REQUEST, TURN THE PUNCH ON,
2) HOLD "HERE IS" FOR ANY LENGTH OF LEADER DESIRED
3) TURN PUNCH OFF
4) ENTER CONTROL U
5) ENTER MODE 8 BUT DO NOT STRIKE "CR"
6) TURN PUNCH ON
7) ENTER "CR"
8) AFTER ALL POINTS HAVE BEEN PUNCHED AND "MODE?" IS AGAIN ASKED, DEPRESS "HERE IS" FOR DESIRED LENGTH OF LEADER
9) TURN PUNCH OFF
10) ENTER CONTROL U AND CONTINUE

TO USE THE PUNCHED CONTROL TAPE

1) AT MODE REQUEST, ENTER MODE 1
2) AT FIRST REQUEST, PLACE TAPE IN READER
3) ALIGN TAPE TO THIRD CHARACTER AFTER THE LAST LEADER CHARACTER
4) MOVE READER CONTROL TO "MANUAL START"
5) AFTER ALL POINTS HAVE BEEN READ IN MOVE READER CONTROL TO "FREE" AND REMOVE TAPE
6) ENTER CONTROL U AND CONTINUE

system as explained in Mode 1 of Figure 2.10. A run was initiated with Mode 7. Other modes were used for editing, expanding and listing of the test stations. The predetermined test flow condition was re-established and the pressure transducers were calibrated for an output of 1 inch of water head equal to 10 volts. The yaw probe was moved to an upstream station outside the range affected by the groyne and aligned to the flow direction by rotating the probe until the differential pressure between the centre tube and the two outer tubes were equal. The command code "run" was entered into the data acquisition system through the TTY. Other information required to start the run is given in Mode 7 of Figure 2.10.

In operation, TCOS sent a digital signal to the D/A (Digital to Analog) converters which then sent an analog signal to the power operational amplifiers of the control unit. This signal was compared to the feedback signal from the transverse device. The compared signal determines the output of the operational amplifiers which drive the probe in one direction or the other until a balanced condition for a sampling location was reached. Movement in the vertical, lateral, and longitudinal directions were controlled by their respective Servo Control units. When the sampling location was determined, TCOS provided a short delay to allow the transducers attached to the probe to stabilize. After this delay, the programme sent a remote start to the data logging unit, timed the readings and then moved the probe to the next location. This was repeated until the test was completed or until the data recording cassette was full, at which time a message was printed on a TTY instructing the user to change the cassette. When the cassette was changed, the test was continued by entering a control character on the TTY. While a test was in progress, the programme allowed specific

(a) Plan View (schematic)

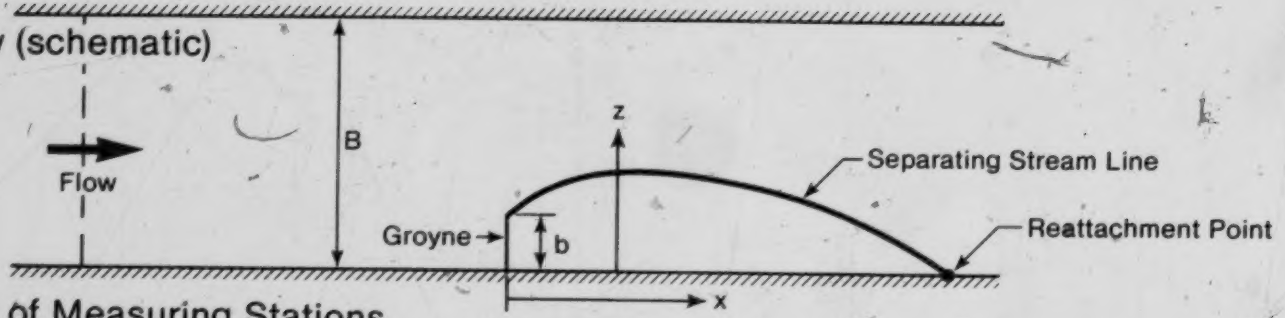
Flow
B
z
x
b
Groyne
Separating Stream Line
Reattachment Point

(b) Location of Measuring Stations

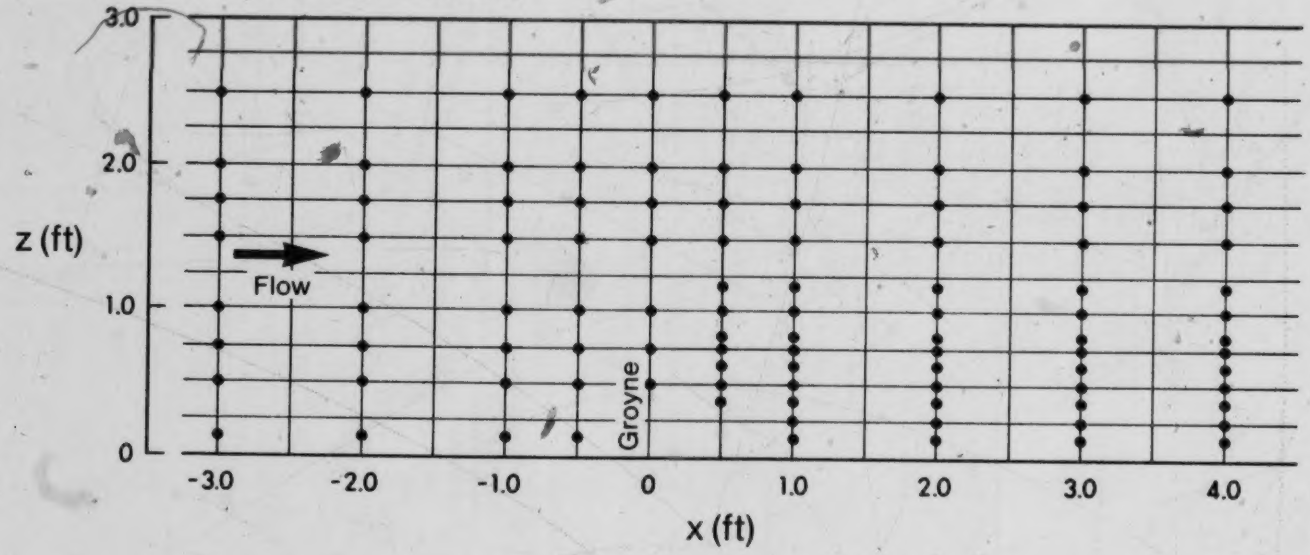
3.0
2.0
1.0
0
z (ft)
Flow
Groyne
-3.0
-2.0
-1.0
0
1.0
2.0
3.0
4.0
x (ft)

Figure 2.11 Definition Sketch and Test Stations

TABLE 2.1

EXPERIMENTS ON RIGID BED

Expt.	Groyne Shape	Depth of flow y_o (ft)	Width of flume B(ft)	Discharge Q(cfs)	Mean Velocity V(ft/sec) $=Q/y_oB$	Length of Groyne b(ft)	Approach Bed Shear Stress τ_{oo} lbs/ft^2	Froude Number $F=\frac{V}{\sqrt{gy_o}}$	Nature of Bed	Shear Stress Amplification $\frac{\tau_{om}}{\tau_{oo}}$
A1	Thin Plate	0.62	3.0	1.6	0.83	0.50	0.0027	0.19	Smooth	4.9
A2	" "	0.73	"	1.6	0.71	"	0.0022	0.15	"	4.5
A3	" "	0.84	"	1.6	0.63	"	0.0017	0.12	"	4.9
A4	" "	0.50	"	1.6	1.05	"	0.0050	0.26	"	4.5
A5	" "	0.50	"	1.2	0.80	"	0.0028	0.20	"	4.6
B1	" "	0.50	"	1.6	1.15	0.25	0.0050	0.29	"	3.0
B2	" "	0.72	"	1.6	0.75	"	0.0024	0.16	"	2.8
B3	" "	0.62	"	1.6	0.78	"	0.0024	0.17	"	3.4
C1	" "	0.50	"	1.58	1.07	"	0.0060	0.27	Sand Paper	5.2
C2	" "	0.73	"	1.6	0.73	0.50	0.0023	0.15	"	5.3
D1	" "	0.72	"	1.6	0.75	"	0.0060	0.16	Hemi-spherical roughness	-
E1	Cylindrical	0.50	"	1.6	1.05	"	0.0047	0.26	Smooth	4.2
E2	"	0.73	"	1.6	0.71	"	0.0022	0.146	"	4.3

characters to be printed on the TTY indicating the sequency of the test operation. Measurements made with the probe on the boundary were used to determine the shear stresses.

2.12 Outline of Experimental Conditions

The experimental programme was organized primarily to determine the structure of flow near a groyne. Secondary concerns include the effect of roughness, the effect of projection length and groyne shape. Table 2.1 gives a summary of experimental conditions. It can be seen that the aspect ratios (width to depth ratio) were less than expected in natural channels. However the constriction ratios, $\frac{B-b}{B}$ were kept in the range of practical interest. The data of this study has been recorded on a tape which is available from the Hydraulics Laboratory, University of Alberta.

2.13 Dimensional Analysis

Considering a thin groyne at right angles to the bank of a straight channel, the following function for the bed shear stress distribution can be formulated:

$$\tau_o = f(\tau_{oo}, z', b, B, x) \tag{2.28}$$

where τ_o is the bed shear stress at any location, τ_{oo} is the approach bed shear stress, b is the groyne projection length, $z' = z-b$, where z, and x are the transverse and longitudinal coordinates respectively.

Assuming τ_{oo} and b as repeating variables, the Pi-theorem yields the following dimensionless arrangement:

$$\frac{\tau_o}{\tau_{oo}} = f(B/b,\ z'/b,\ x/b) \tag{2.29}$$

Writing $\tau_o = \tau_{oo} + \Delta\tau_o$ where $\Delta\tau_o$ is the change in bed shear stress from the approach value, equation 3.29 could be transformed to:

$$\frac{\Delta\tau_o}{\tau_{oo}} = f(B/b,\ z'/b,\ x/b) \tag{2.30}$$

A plot of the shear stress distribution as suggested in equation 3.29 using z'/b as a third parameter, for a specified B/b, shows that τ_o/τ_{oo} increases from an upstream value of 1.0 to a maximum value and decreases thereafter. For the maximum shear stress at any longitudinal section, one could write:

$$\tau_{om} = f(\tau_{oo},\ b,\ B,\ z') \tag{2.31}$$

or

$$\frac{\tau_{om}}{\tau_{oo}} = f(B/b,\ z'/b) \tag{2.32}$$

If $\tau_{om} = \tau_{oo} + \Delta\tau_{om}$, equation 3.32 transforms to:

$$\frac{\Delta\tau_{om}}{\tau_{oo}} = f(B/b,\ z'/b) \tag{2.33}$$

Similary, the location x_m of the maximum bed shear stress along any longitudinal section could be formulated as:

$$x_m = f(z', b, B) \tag{2.34}$$

or

$$\frac{x_m}{b} = f(B/b, z'/b) \tag{2.35}$$

These dimensionless considerations guided the analyses of the measured bed shear stresses.

The velocity distribution and the angles of the velocity vectors could also be subjected to dimensional analysis. Consider for example, the upper potential flow layer. If U is the velocity at any location and U_o is the approach velocity, we could write:

$$U = f(U_o, x, z, b, B) \tag{2.36}$$

Assuming U_o and b as the repeating variables, then

$$\frac{U}{U_o} = f(x/b, z/b, B/b) \tag{2.37}$$

Next, if α is the angle of the velocity vector at any location,

$$\alpha = f(x, b, B, z) \tag{2.38}$$

or

$$\alpha = f(B/b, z/b, z/b) \tag{2.39}$$

Empirical relations for equation 3.37 and 3.39 were determined in this study (see Figures 3.20, 3.22).

CHAPTER 3

EXPERIMENTAL RESULTS AND ANALYSIS

In this chapter, the experimental results obtained in the fixed bed flume are presented. The data are analysed using the model of a skewed turbulent boundary layer and similarity technique. The experimental programme is summarized in Table 2.1. Five series of experiments were performed using two lengths of thin groyne, a cylindrically shaped groyne, in smooth and rough beds.

3.1 Experimental Results

3.1.1 Velocity Data

Velocity profiles [u(y)] measured in the centreplane at a distance of 3 ft. upstream of the groyne are shown in Figure 3.1 (a to c), wherein u is the velocity component in the x-direction. At this upstream reference section, it was determined that the presence of the groyne did not disturb the flow. For the larger hemispherical roughness, experiment D1 in Figure 3.1c, y was plotted from a hypothetical plane located 0.2 diameter below the tops of the hemispheres. All the profiles indicate that the velocity increases linearly with log y. The two series E experiments were very similar to A4 and A2 experiments respectively and have not been shown in Figure 3.1. Typical velocity profiles in the region affected by the presence of the groyne are presented in Figure 3.2(a and b). Some profiles were not shown in these plots for clarity of presentation. The entire profiles indicate that

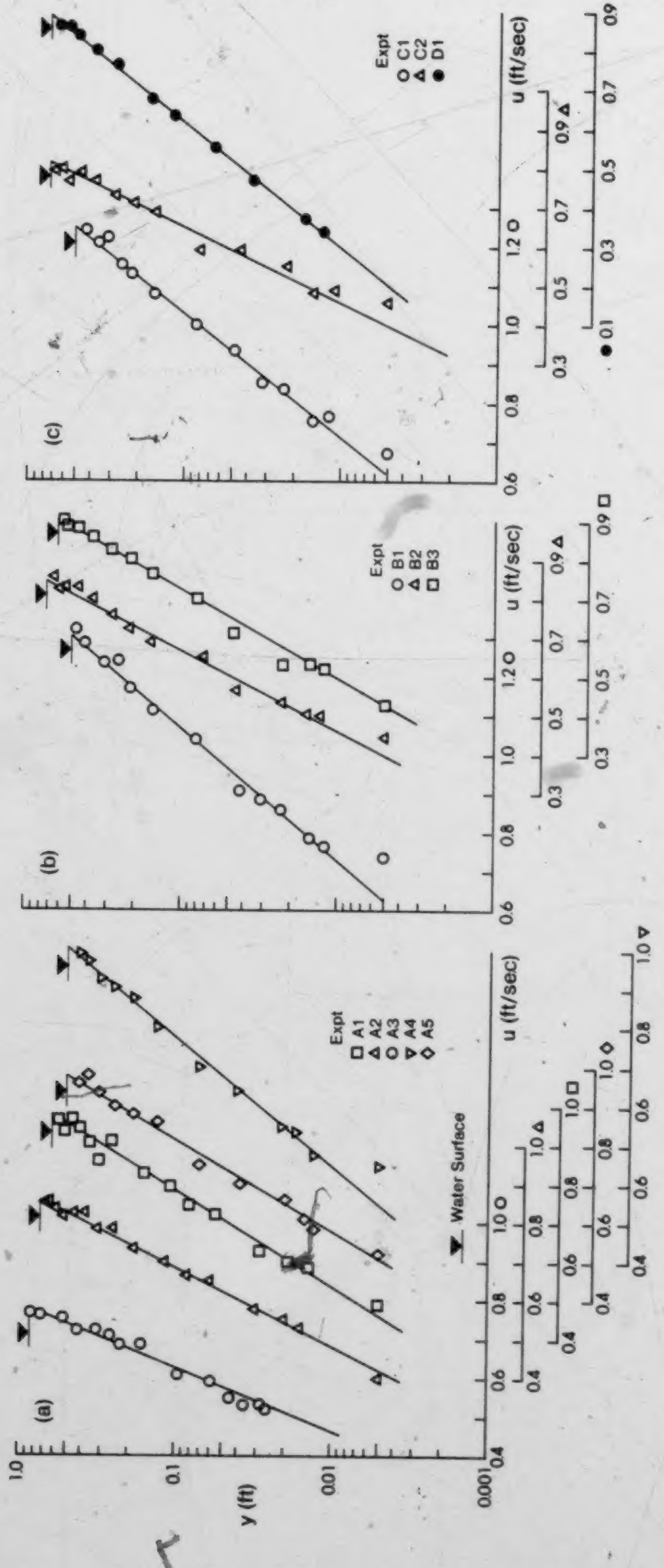

Figure 3.1 Velocity in the Approach Flow

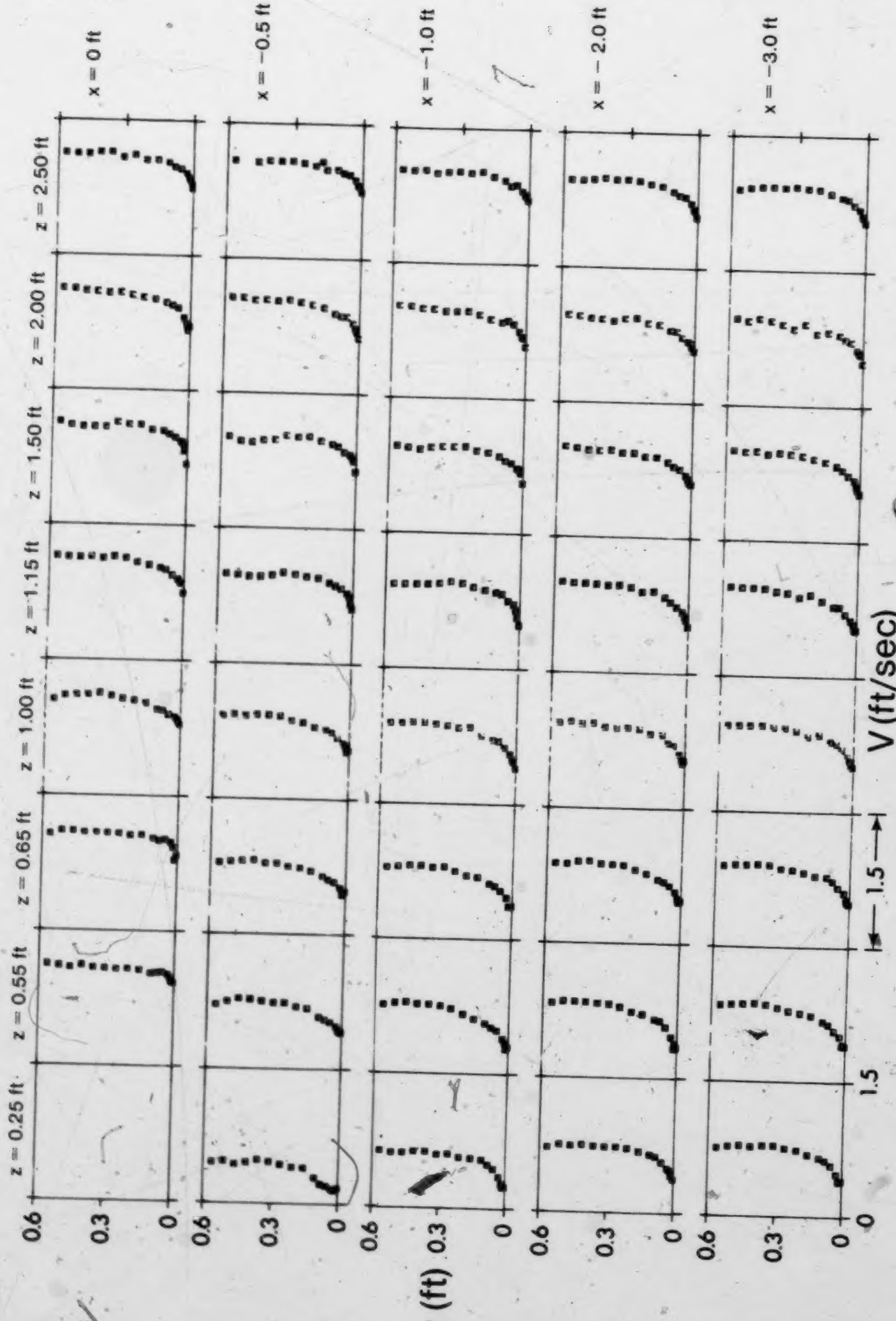

Figure 3.2 (a) Velocity Profiles Near a Groyne (Expt. A1, Upstream)

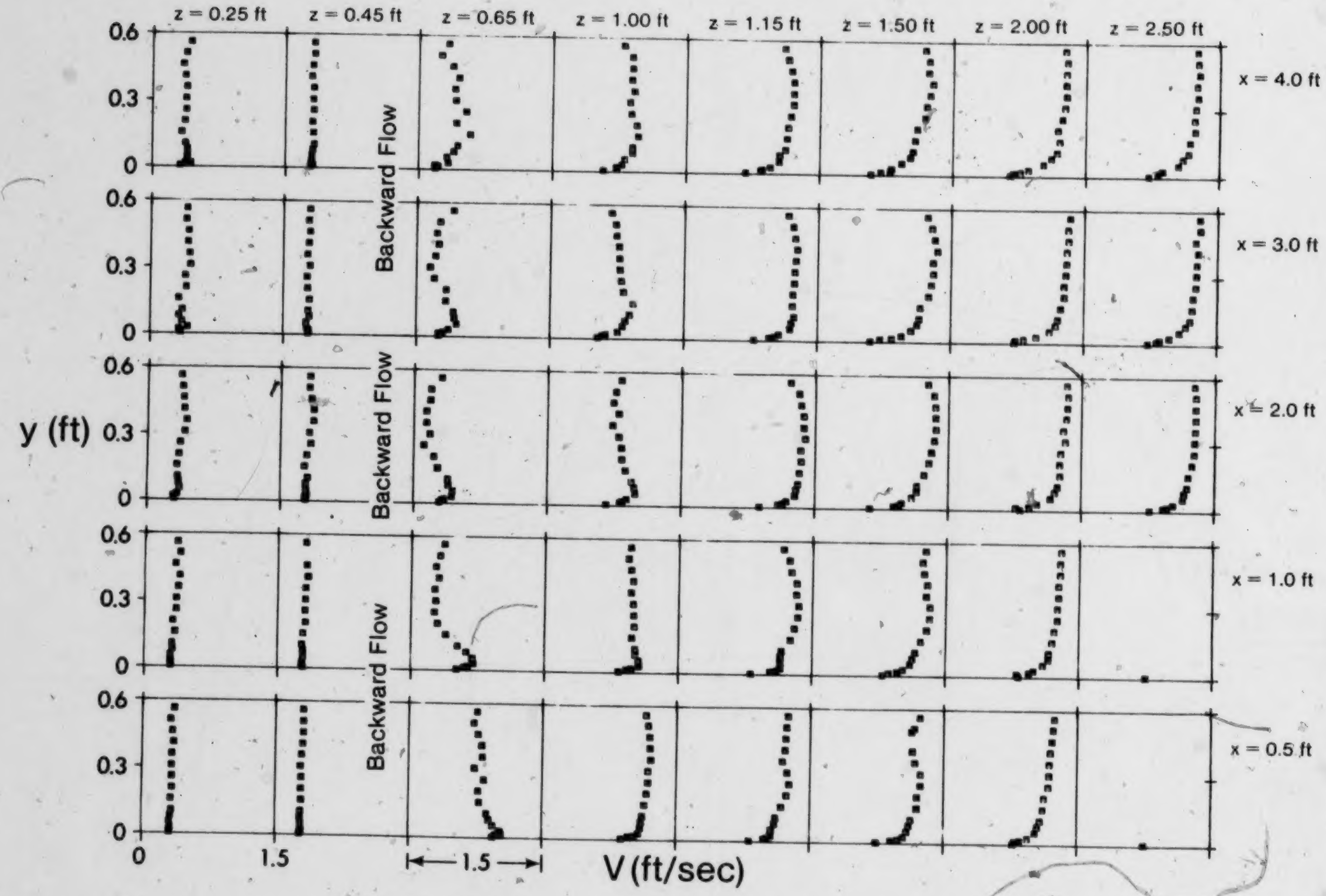

Figure 3.2 (b) Velocity Profiles Near a Groyne (Expt. A1, Downstream)

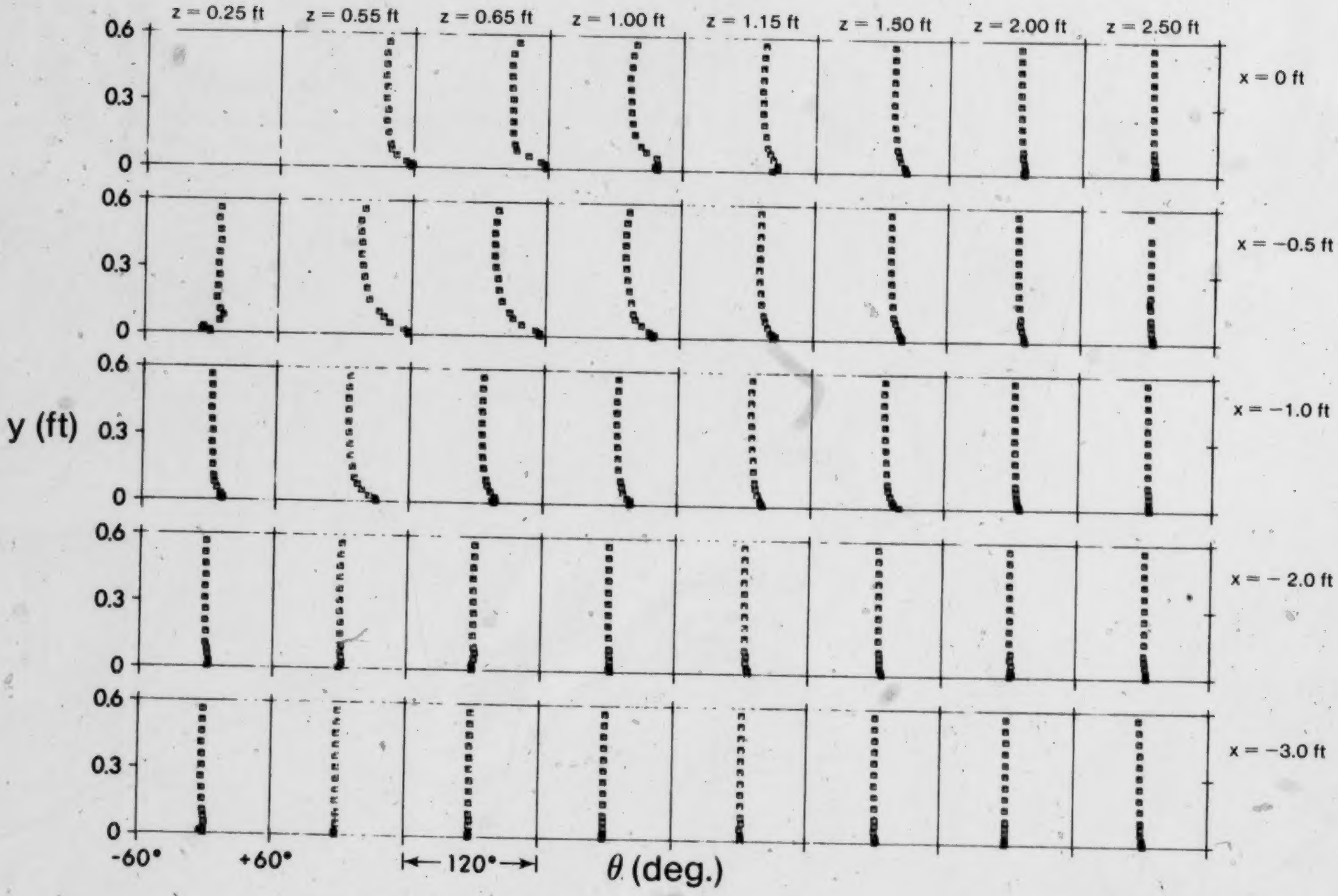

Figure 3.3 (a), Vertical Distribution of the Angles of Velocity Vector (Expt. A1, Upstream)

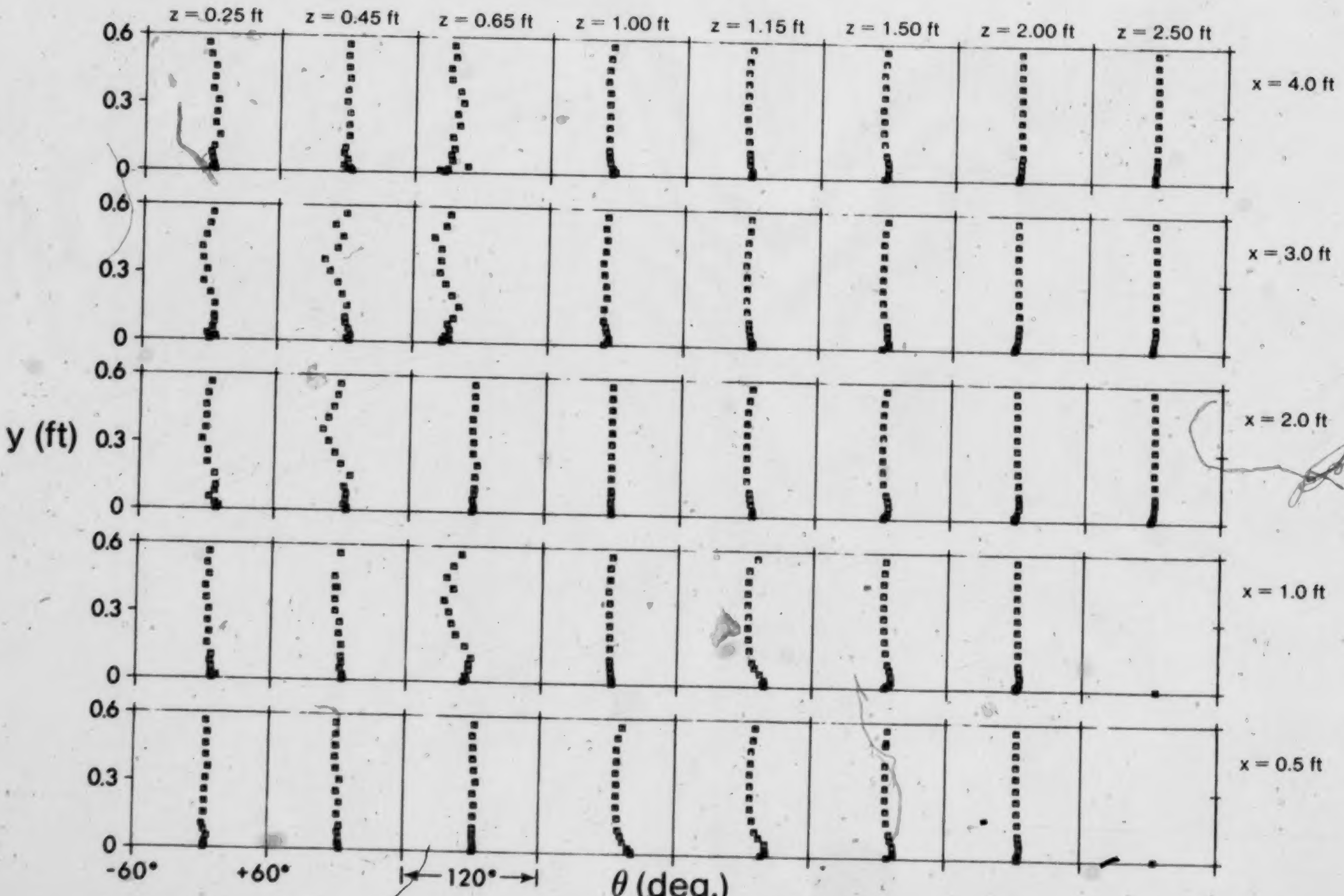

Figure 3.3 (b) Vertical Distribution of the Angles of Velocity Vector (Expt. A1, Downstream)

as the water flows around the groyne, the velocity distribution becomes almost uniform near the nose of the groyne and in the backward flow region. Further downstream, near the nose, the profiles show the formation of a high velocity jet close to the bed. The vertical distribution of the angles of the velocity vectors relative to the longitudinal direction are plotted in Figure 3.3 (a and b). Figures 3.2 and 3.3 suggest that the velocity field in the region deflected by the groyne could be analysed by treating it as a skewed turbulent boundary layer (see Nash and Patel, 1972). The velocity measurements for experiment A1 for $\frac{x}{b}$ = -2, -1, 0, 1, 2, 3, and 8 for different values of the transverse distance z are shown in Figure 3.4 in the form of Johnston's polar plots, where b is the groyne projection length. In these plots, for any location, the x-component of velocity u is plotted against the z-component w which is normal to the u component. These plots and similar ones for the other experiments generally showed that in the deflected flow upstream of the groyne as well as in the downstream region for the $\frac{x}{b}$ up to about 1.0, there exists an inner region in which the velocity profiles are collinear and the velocity vectors are in the direction of the wall shear. In the outer layer above the inner layer which terminates at the apex of the triangle, the velocity vector increases in magnitude and simultaneously turns continuously away from the wall shear stress until it attains the magnitude and direction of the upper potential layer. For $\frac{x}{b}$ greater than about 2.0 and particularly for the verticals with larger values of $\frac{z}{b}$, the Johnston triangle begins to deform until the velocity vectors, further downstream, eventually become collinear for the whole depth of flow.

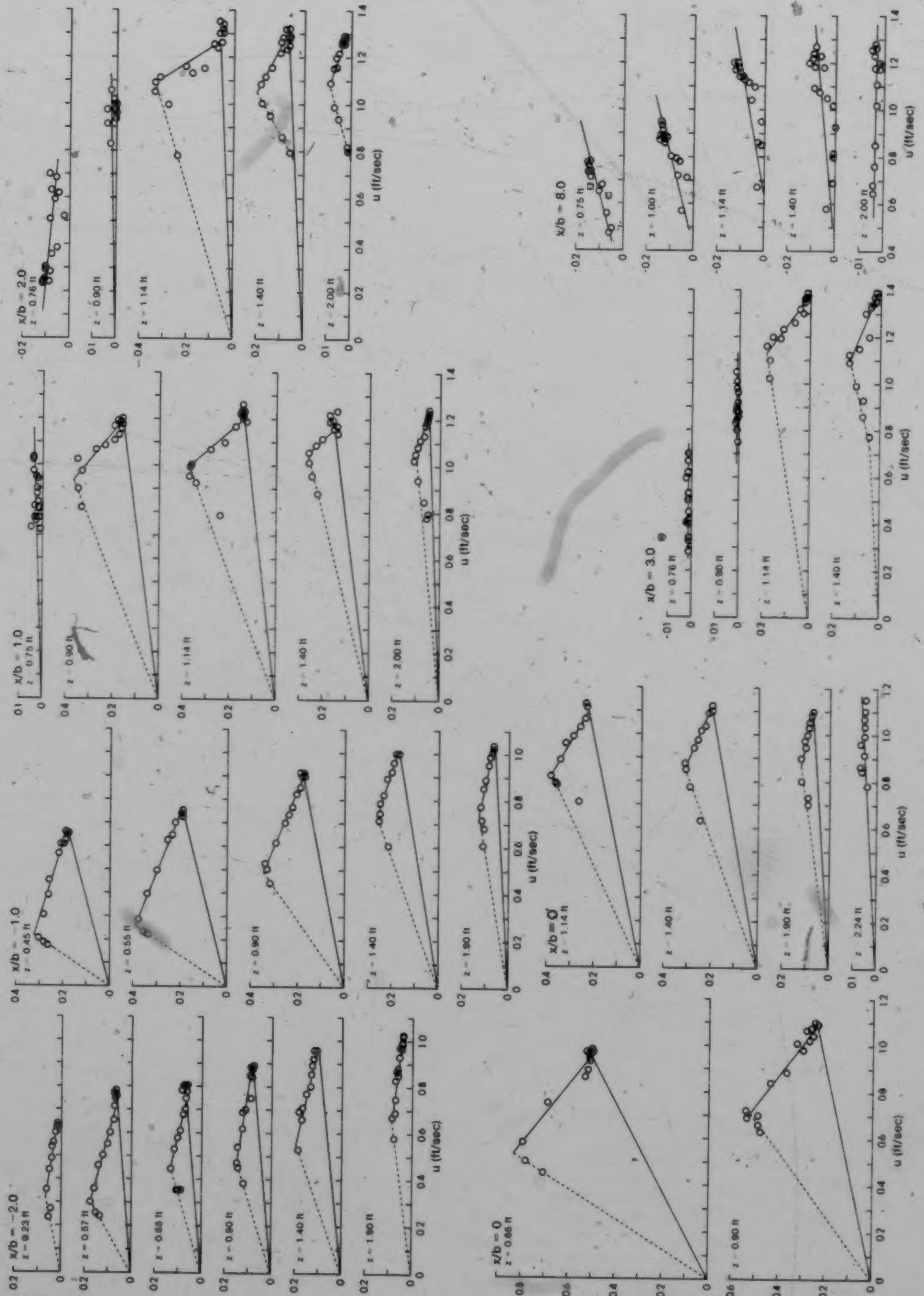

Figure 3.4 Polar Plots in Skewed Boundary Layer (Expt. A1)

3.1.2 Shear Stress Data

Experimental results for the bed shear stress are shown in Figure 3.5. Series A experiments are plotted in Figure 3.5a; Series B, C, D experiments are shown in Figure 3.5b and Series E experiments are shown in Figure 3.5c. The plots indicate in general, considerable increase in bed shear stress τ_o near the nose and the immediate neighbourhood of the groyne. In Figure 3.5a, considering experiment A1 with smooth bed, and z = 0.5 ft. (i.e. $\frac{z}{b} = 1.0$), as the nose of the groyne is approached, τ_o increases rather rapidly from the upstream value of $\tau_{oo} \simeq 0.0025$ lbs/sq.ft. to a maximum of τ_{om} of about 0.013 lbs/sq.ft. and then decreases rapidly as x increases, entering into the wake. For $\frac{z}{b}$ greater than one, τ_{om} assumes decreasing values occurring downstream of the nose. If τ_{ox} and τ_{oz} are respectively the longitudinal and transverse components of the bed shear stress, the variations of τ_{ox} shown in Figure 3.6(a) indicates a variation very much like that of τ_o itself. Figure 3.6(b) shows that τ_{oz} increases with x from zero to reach the peak value at or near the nose and then decreases continuously. Figure 3.7(a) shows a typical contour-type plot of τ_o for the neighbourhood of the groyne and the maximum value of $\frac{\tau_o}{\tau_{oo}}$ is about 5.0. The shorter groyne shows smaller bed shear stress amplification (see Table 2.1 and Figure 3.5b). Figure 3.7(b) and Figure 3.5(b) (series C and D plots) also show that the shear stress profiles on the bed [i.e. $\tau_o(z,x)$] behave in the same general way for the sand-paper and larger hemi-spherical roughness. However, for the cylindrically shaped groyne [series E, Figures 3.5(c) and 3.7(c)], the increase in bed shear stress for $z/b \geq 1.5$ is minimal.

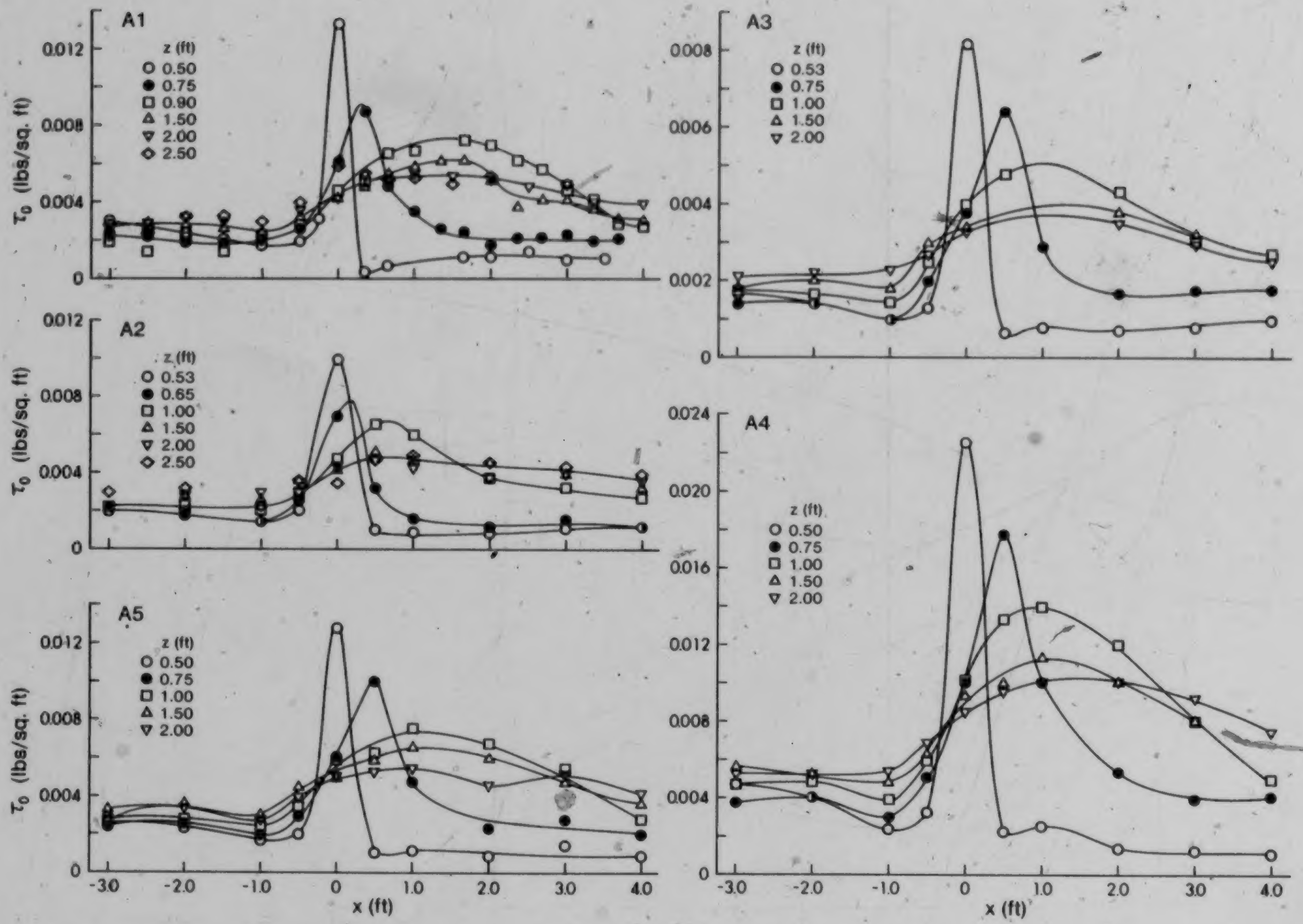

Figure 3.5 (a) Bed Shear Stress Plots (Series A Expts.)

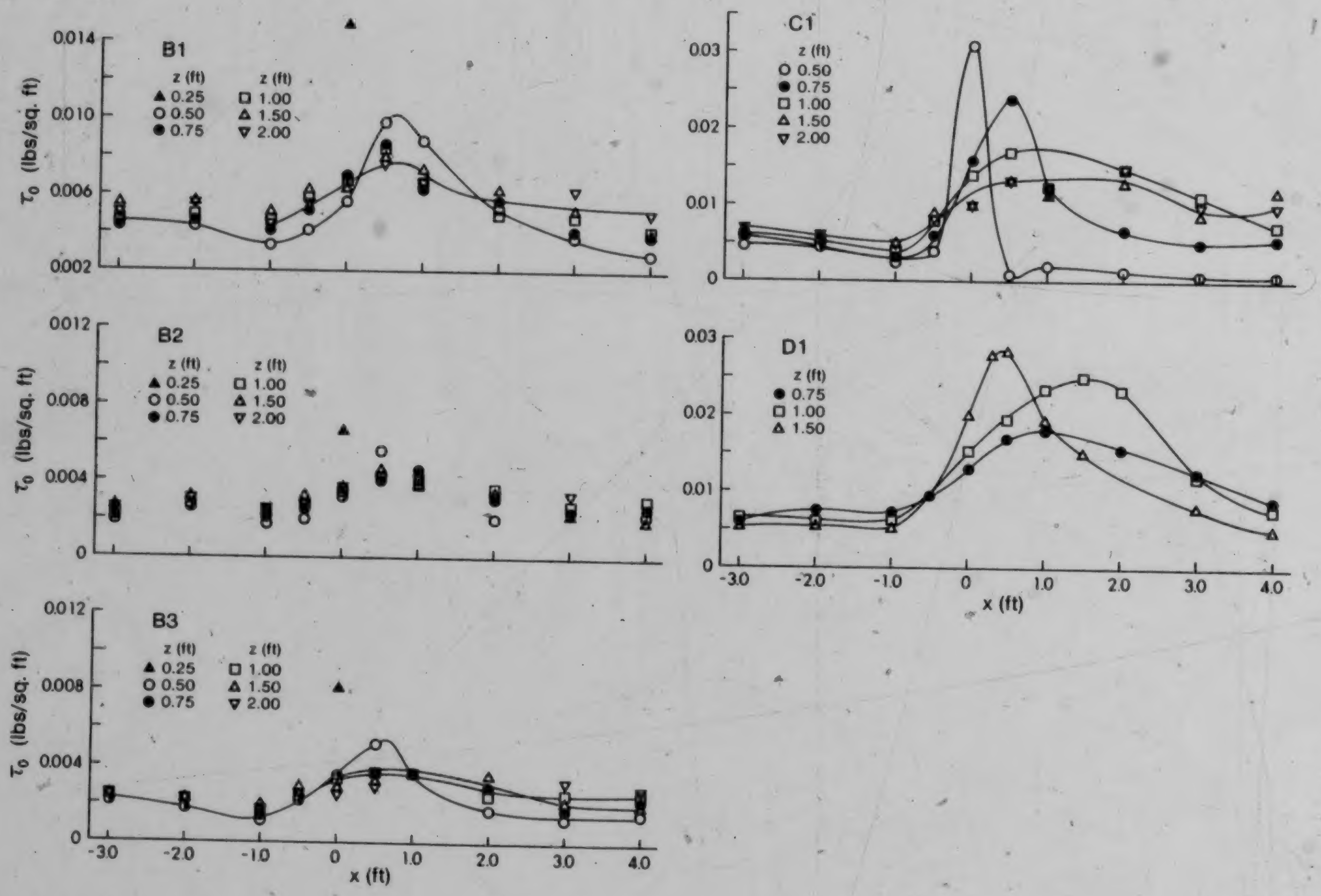

Figure 3.5 (b) Bed Shear Stress Plots (Series B, C, D Expts.)

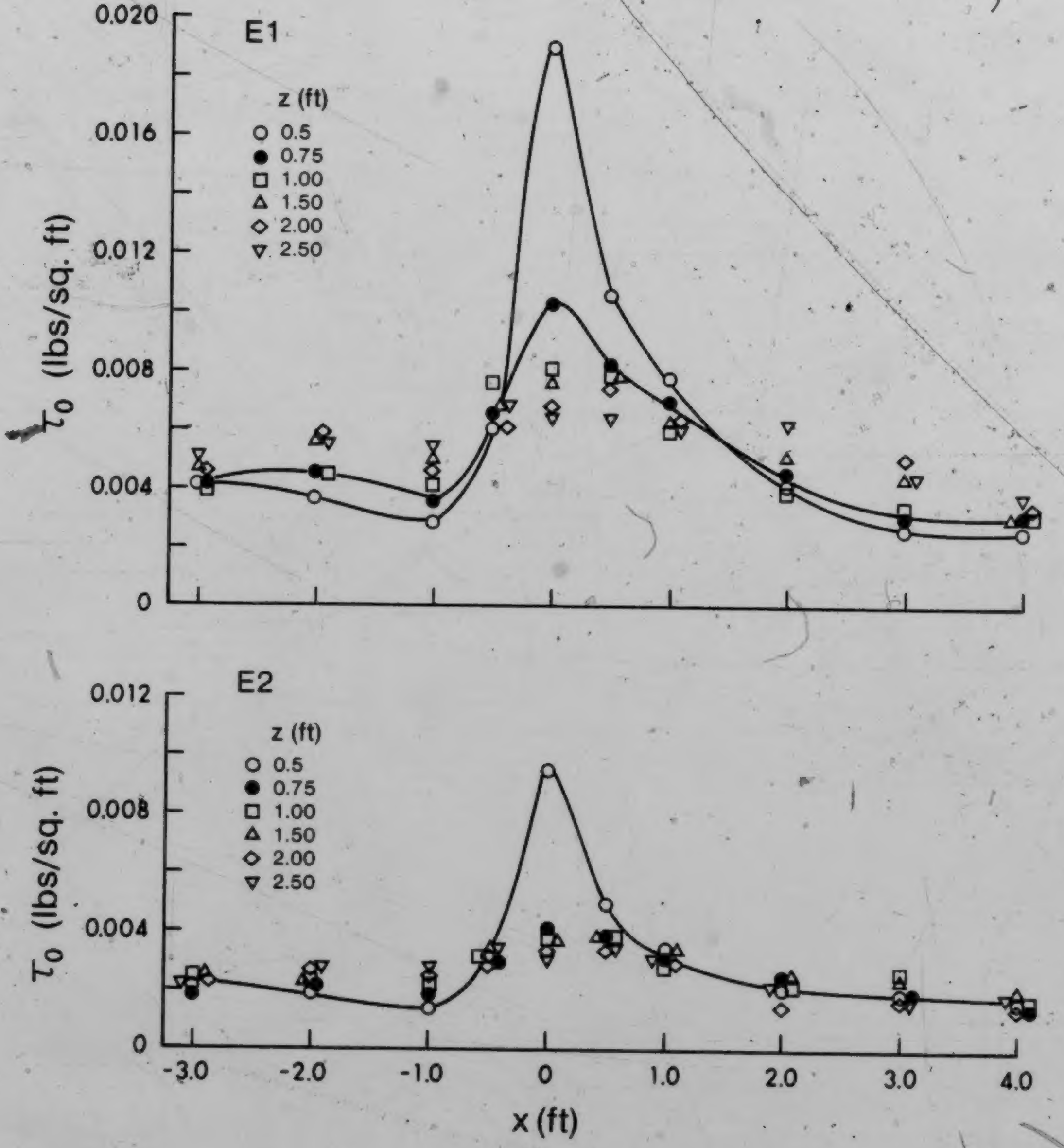

Figure 3.5 (c) Bed Shear Stress Plots (Series E Expts.)

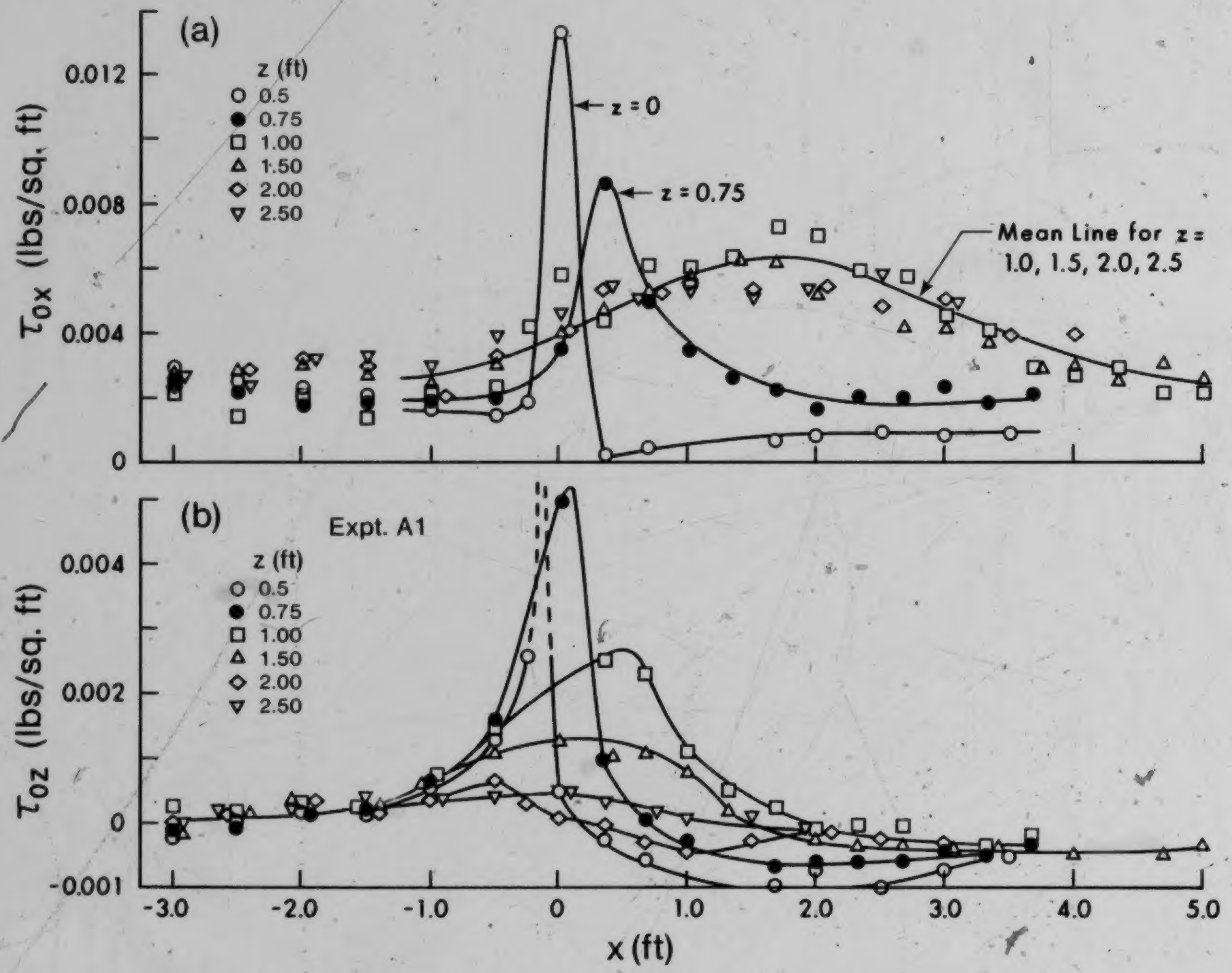

Figure 3.6 (a & b) Variation of τ_{ox} and τ_{oz} (Expt. A1)

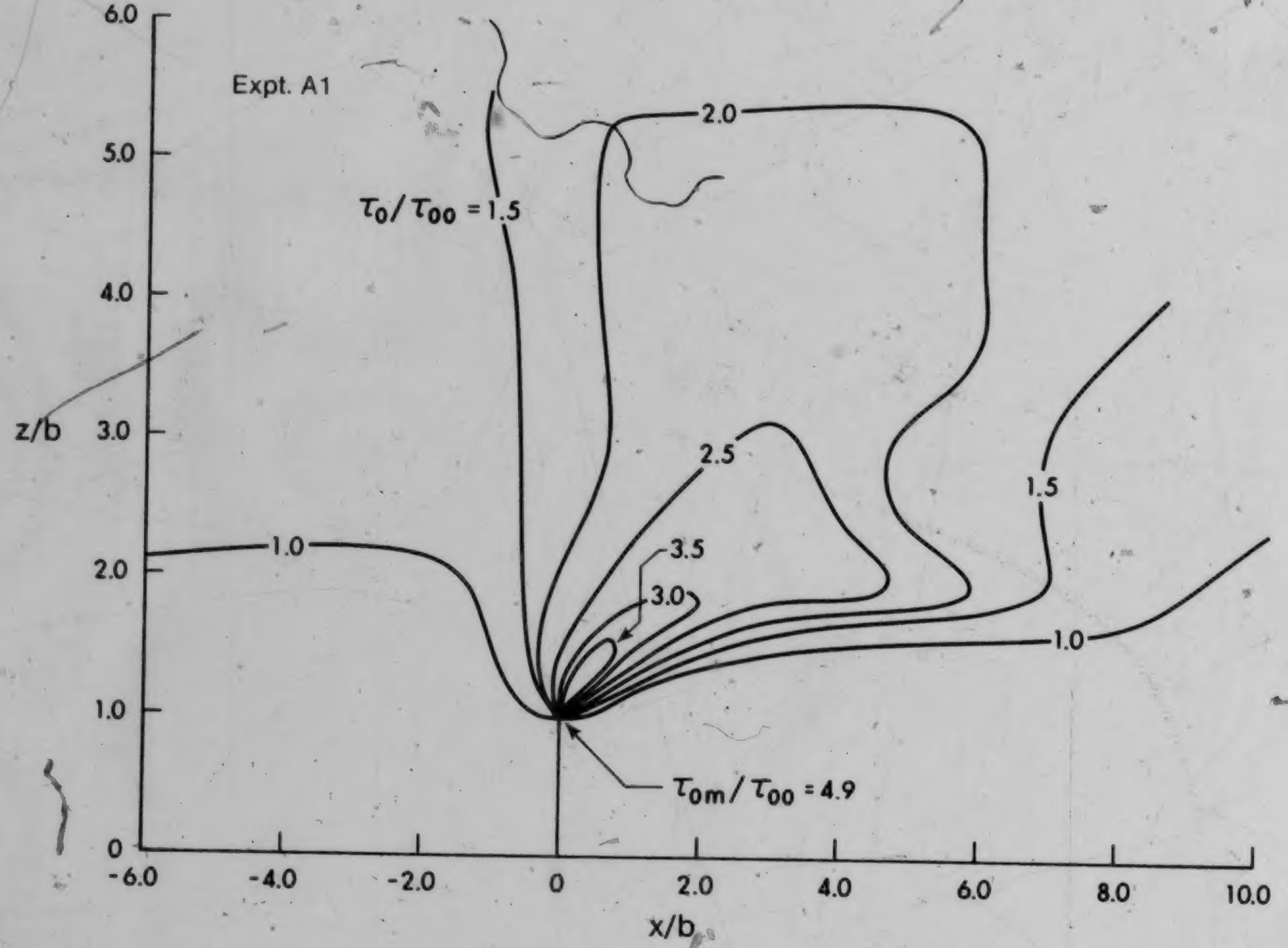

Figure 3.7 (a) Contour Plot for τ_o (Expt. A1)

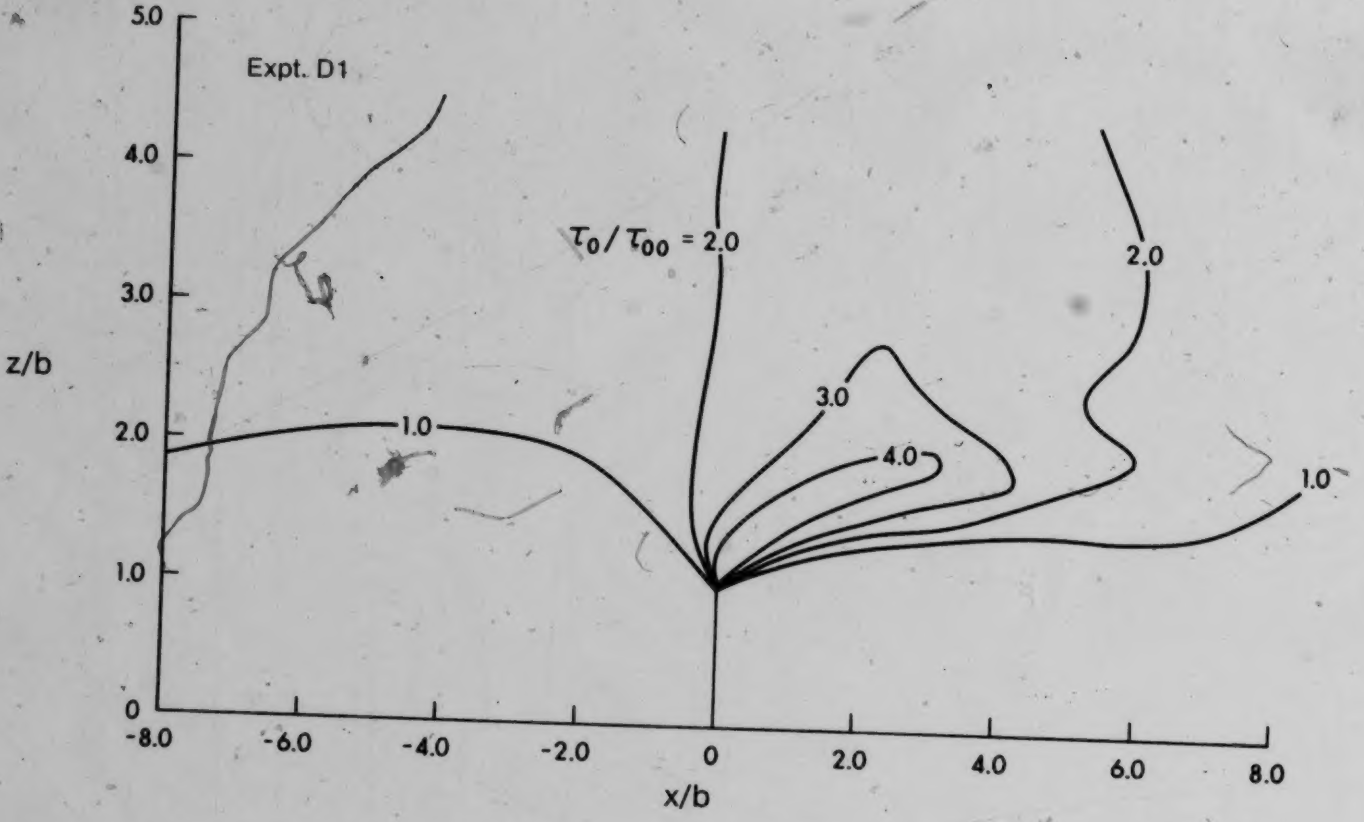

Figure 3.7 (b) Contour Plot for τ_o (Expt. D1)

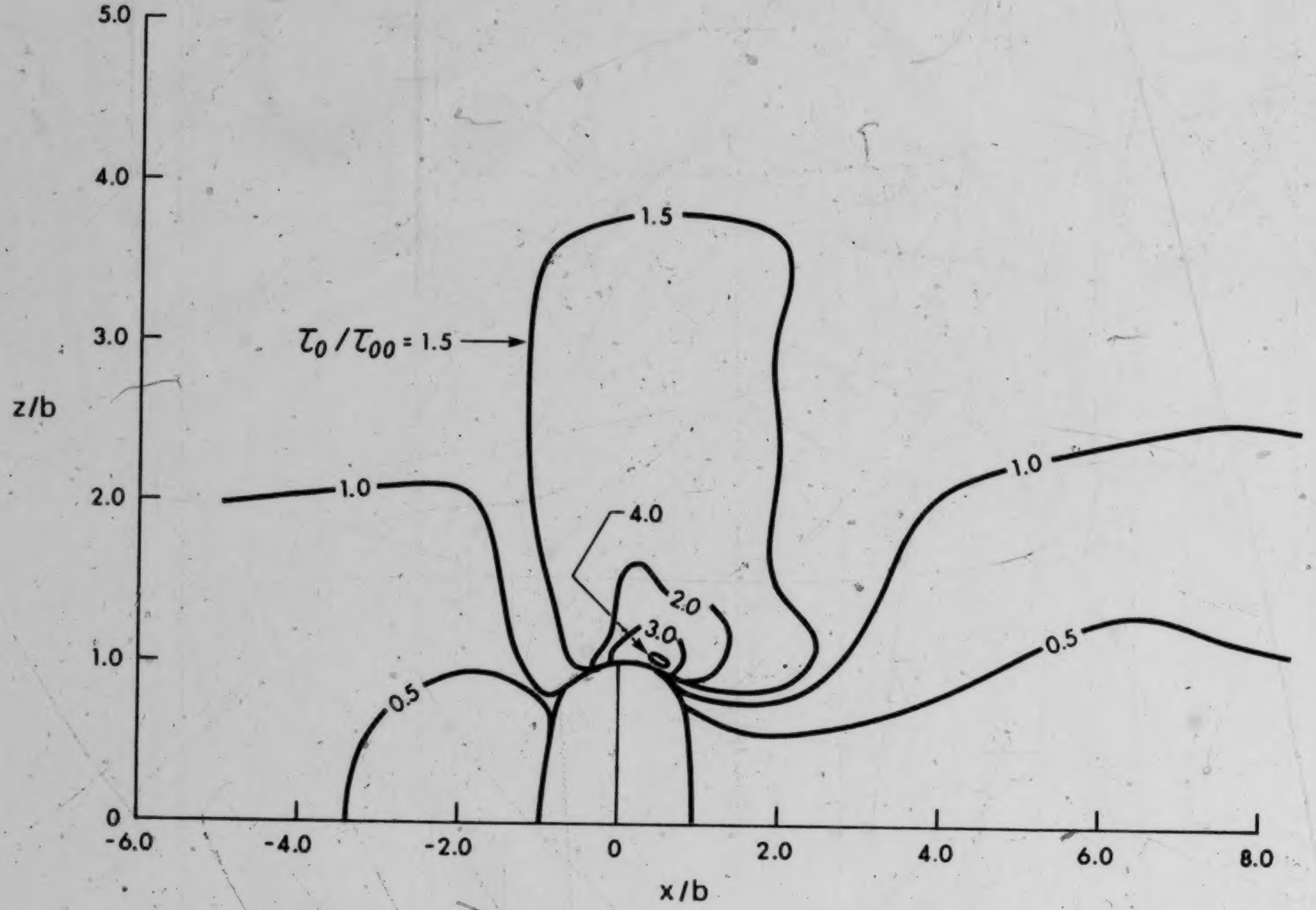

Figure 3.7 (c) Contour Plot for τ_0 (Expt. E1)

3.1.3 Shear Layer Data

The features of the velocity distribution downstream of the groyne are shown for experiment A1 in Figure 3.8 for two arbitrarily chosen levels, one for $\frac{y}{y_o} = 0.03$ and another for $\frac{y}{y_o} = 0.85$, where y_o is the approach depth of flow. Both plots show clearly the backward-flow region behind the groyne. At the upper level, the velocity, at any x distance increases continuously with z, starting from the backward-flow region, until it merges with the flow speeded up by the constriction caused by the groyne. At the lower level, especially for $\frac{x}{b} = 2$ to 6, the maximum velocity reached at any x appears to be the same but because the velocity magnitude at larger z is smaller because of the proximity of the bed, a characteristic peak occurs in the velocity profiles at the location of velocity concentration. A more detailed set of velocity profiles are shown in Figure 3.9 for experiment A4. Similar structural features can also be noticed in the velocity profiles for experiment C1 with the sand roughness (Figure 3.10 a,b). For the larger hemi-spherical roughness, the profile at $\frac{y}{y_o} = 0.6$ (Figure 3.10c) has the same general features. The regions of backward-flow for experiments B series (shorter groyne) and E series (cylindrical shape) were small and could not be investigated with the traverse system used for the study.

3.1.4 Water Surface Data

As the water flows past the groyne, there is a lowering of the water surface at the nose of and behind the groyne. A typical set of water surface profiles (for experiment A3) is given in Figure 3.11. These profiles show that for $\frac{z}{b} = 1.0$ (or z = 0.5 ft.) there is an almost

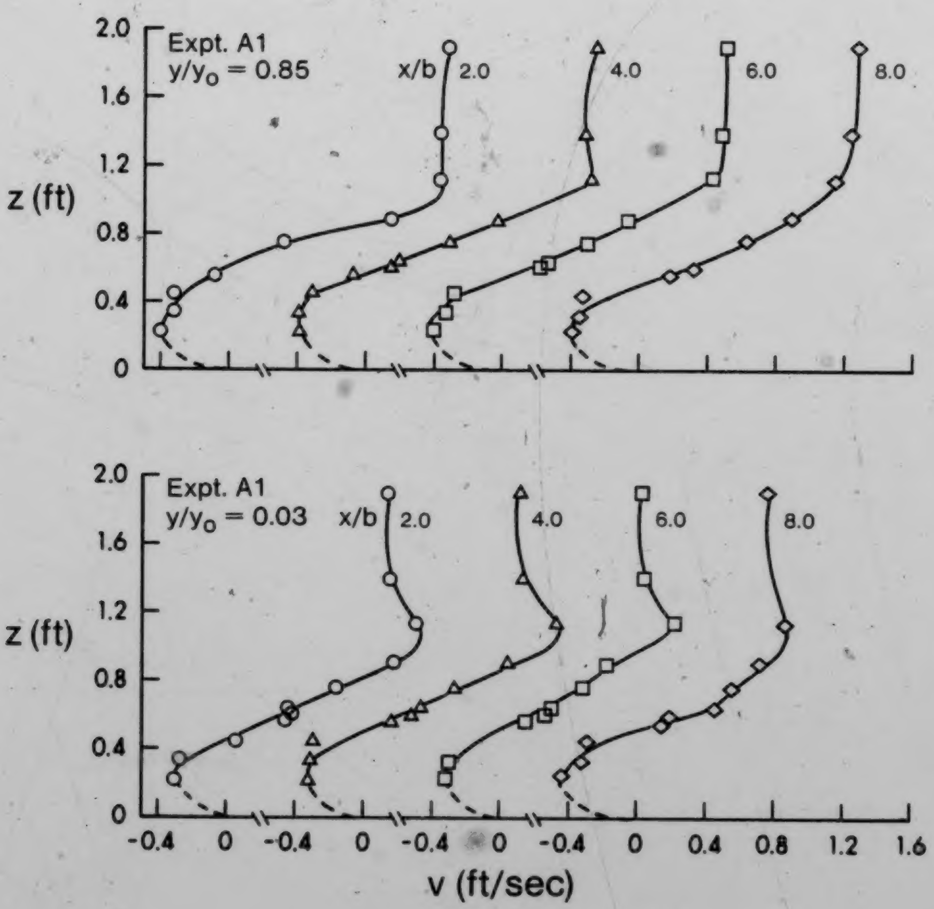

Figure 3.8 Velocity Profiles in Shear Layer (Expt. A1)

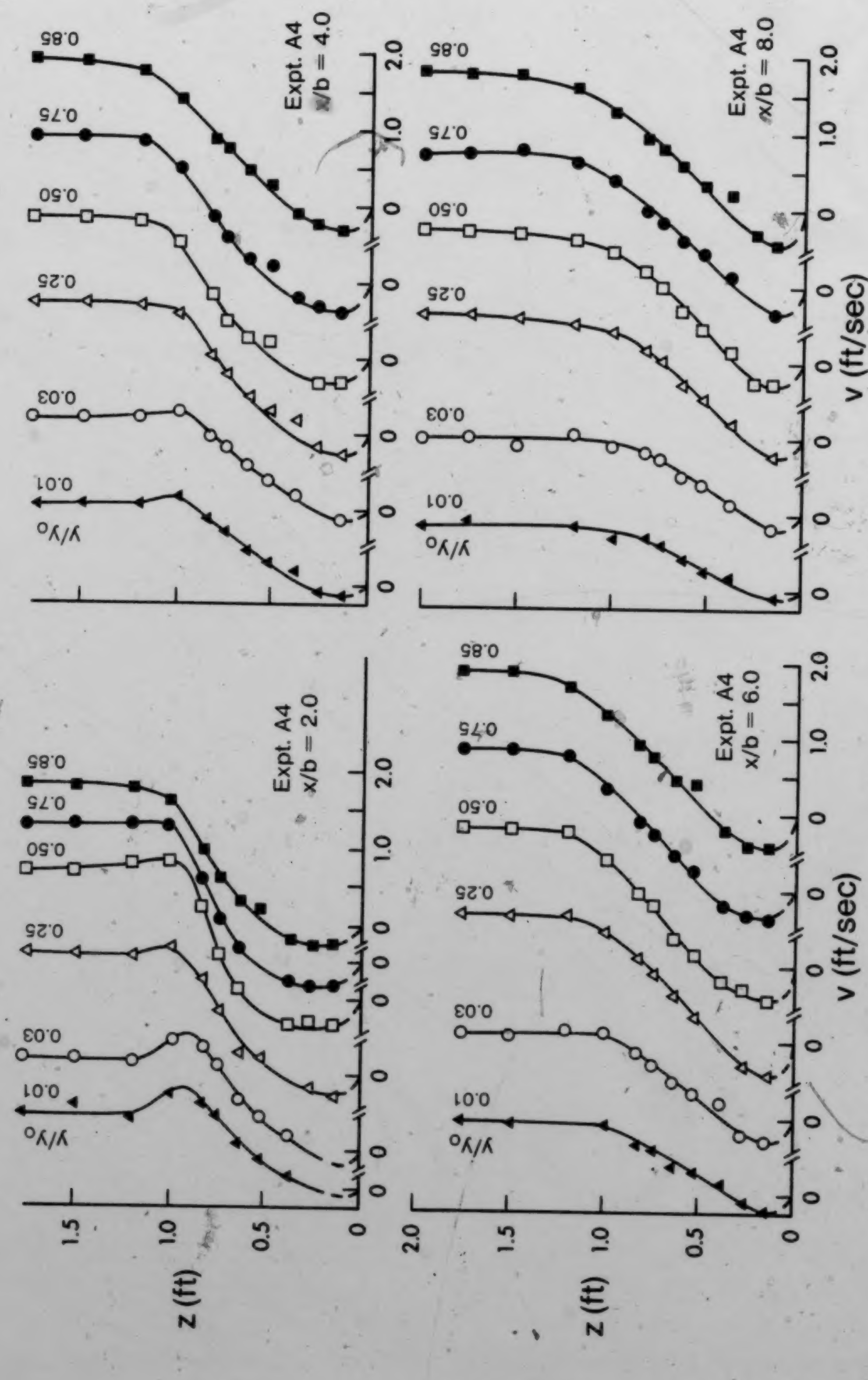

Figure 3.9 Detailed Velocity Profiles in Shear Layer (Expt. A4)

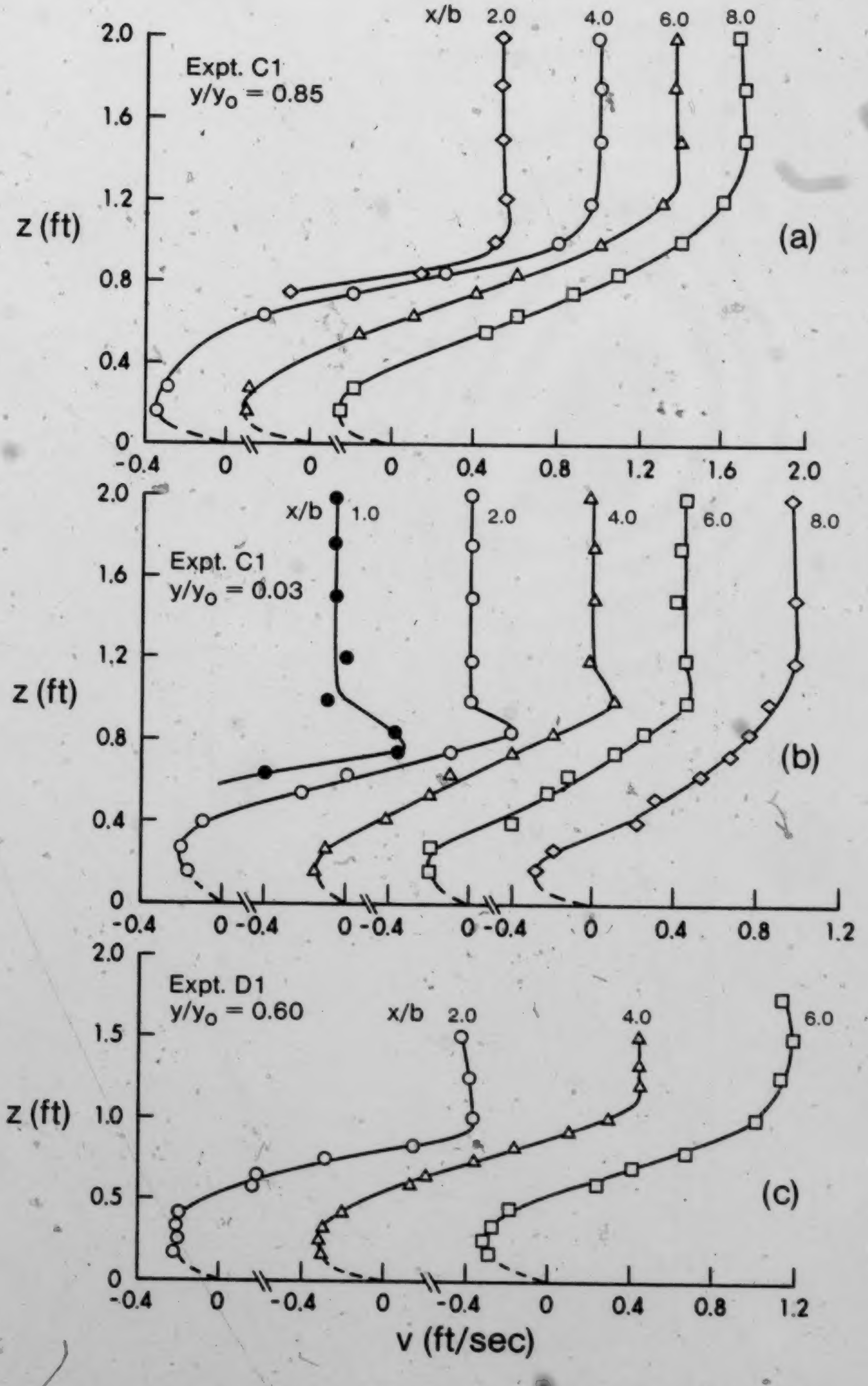

Figure 3.10 Velocity Profiles in Shear Layer (Expts. C1, D1)

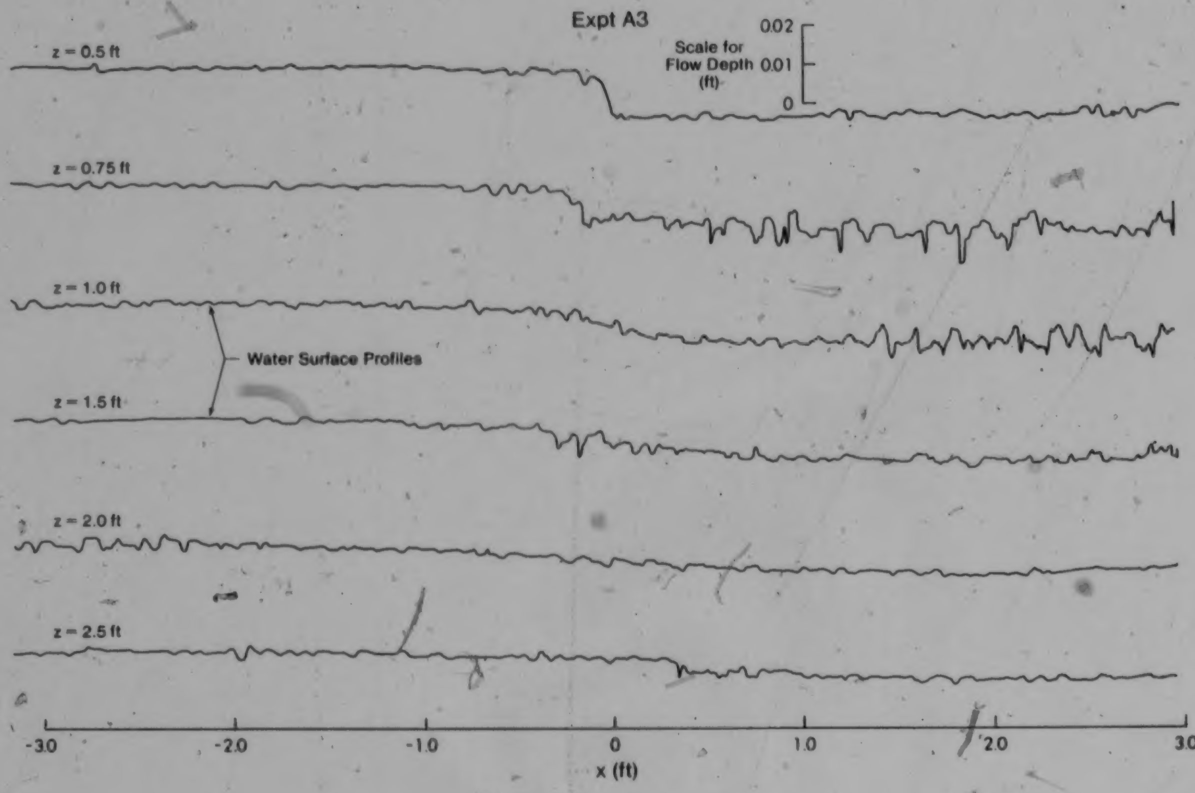

Figure 3.11 (a) Typical Water Surface Profile

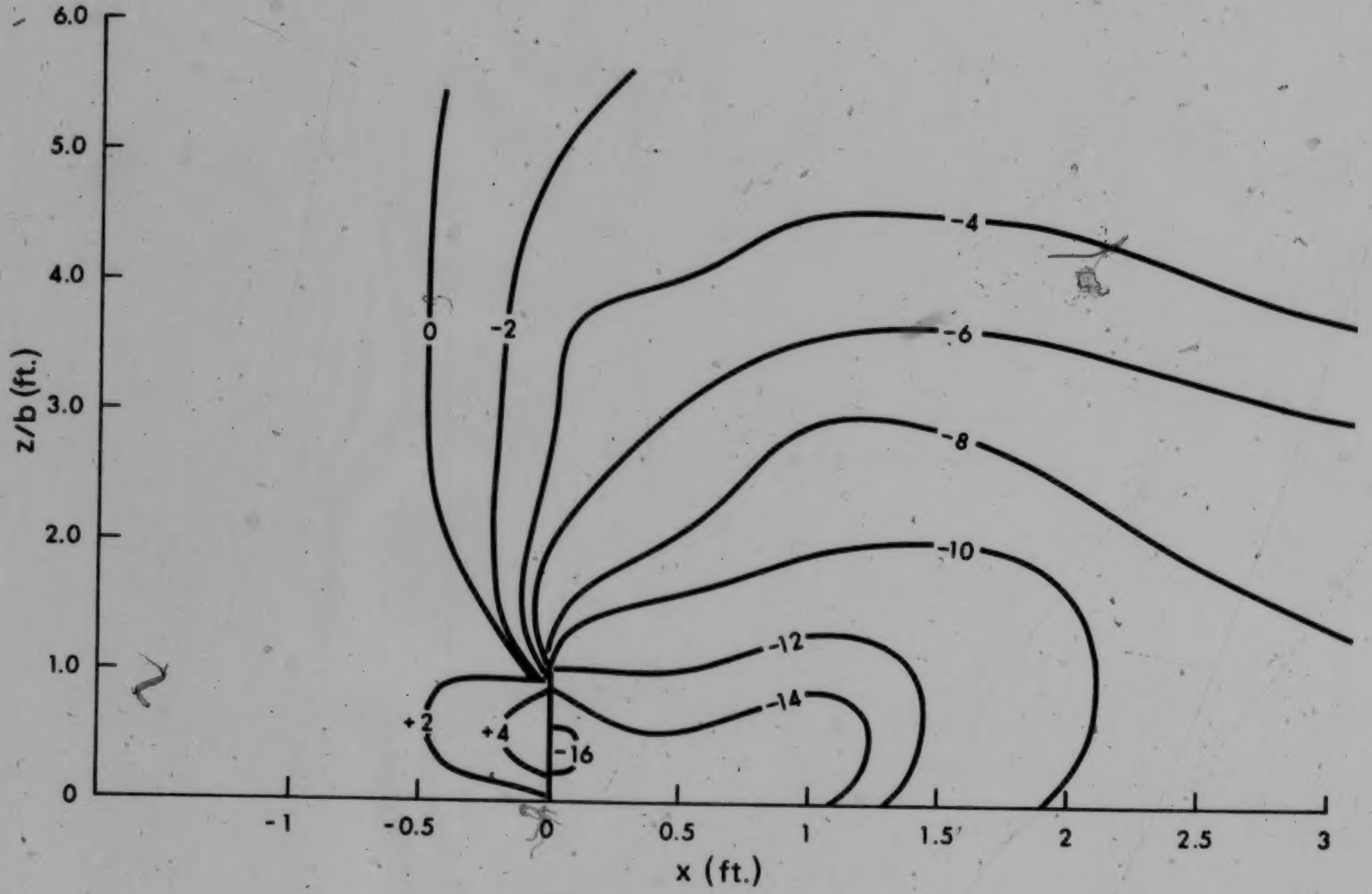

Figure 3.11 (b) Water Surface Topography (Expt A1, Elev. x 10^{-3} Ft. From Approach Depth)

sudden drop near the nose of the groyne but the water surface is almost horizontal upstream and downstream of this drop. The profiles for larger values of z indicate a gradual fall in the water surface levels. Figure 3.11(b) shows a typical water surface topography. There appears to be no obvious correlation between the bed shear stress contour (Figure 3.7) and the water surface topography.

3.2 Analysis of Experimental Results

3.2.1 Approach Flow

The velocity profiles u(y) obtained in the centreplane at x = -3.0 for the experiments with the smooth bed (series A and B) indicated that the flow was fully developed approaching the groyne. It could be called a fully developed open channel flow or a fully developed turbulent boundary layer. These profiles can be plotted in dimensionless form to see whether they satisfy the Karman-Prandtl logarithmic law. Consequently, the dimensionless velocity $\frac{u}{u_*}$ (wherein u_* is the Prandtl shear velocity equal to $\sqrt{\frac{\tau_o}{\rho}}$) was plotted against the dimensionless distance $\frac{yu_*}{\nu}$ in Figure 3.12. The figure shows that for all five experiments (A1-A5), the data agree reasonably well with the equation.

$$\frac{u}{u_*} = 5.75 \log \frac{yu_*}{\nu} + 5.5$$

It was also verified that in series B and E experiments, on smooth bed, the dimensionless velocity profiles at the upstream reference station were satisfied by the same equation. For these experiments therefore the flows were hydrodynamically smooth.

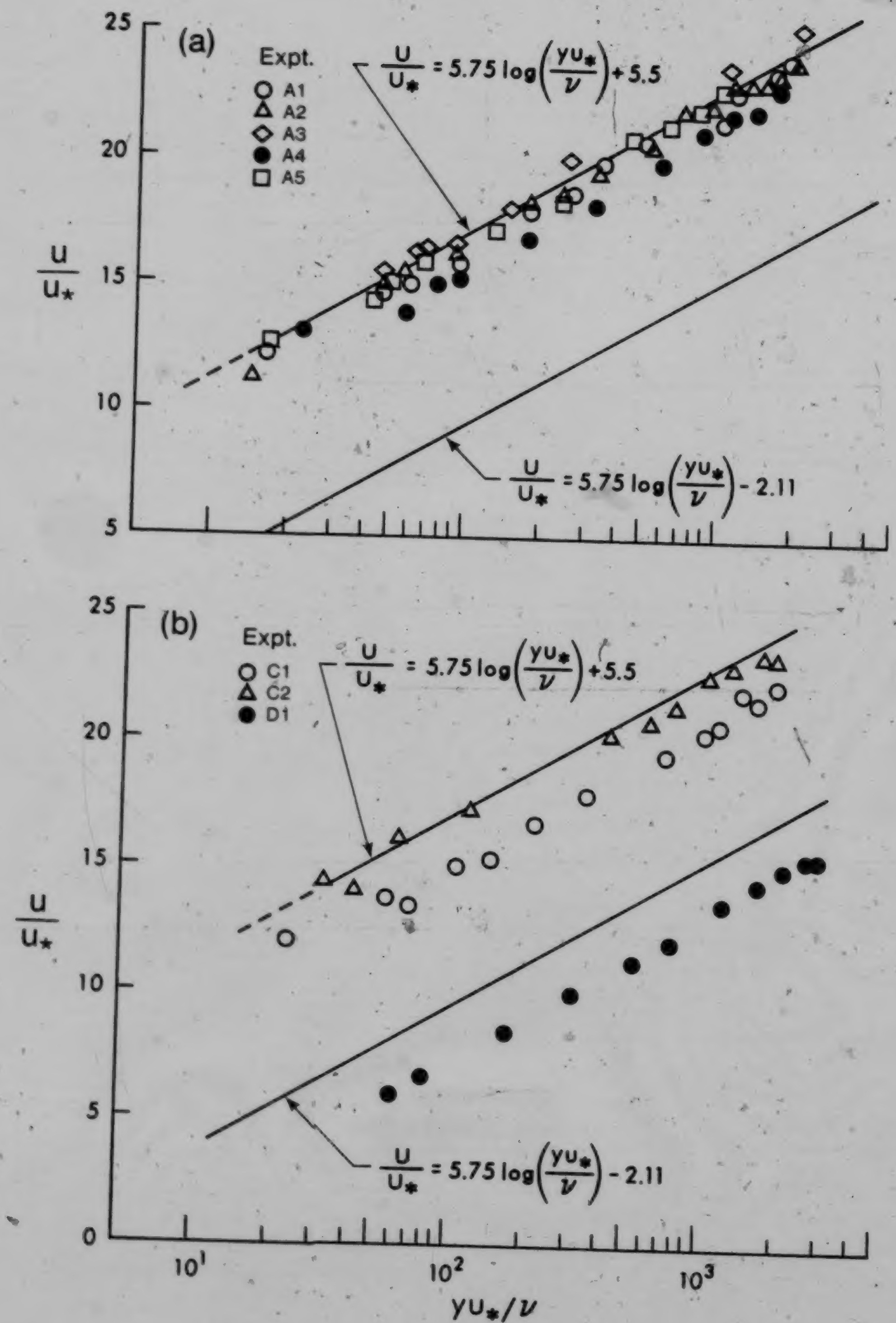

Figure 3.12 Dimensionless Velocity Profiles for the Approach Flow

The results for one sand-paper (experiment C2) showed [see Figure 3.12(b)] that the flow was also hydrodynamically smooth whereas for the second sand-paper (experiment C1) the flow was in the transition from smooth to rough flow. The flow was rough turbulent for the hemispherical roughness as indicated by Figure 3.12(b). In this figure, the equation

$$\frac{u}{u_*} = 5.75 \log \frac{yu_*}{\nu} - 2.11$$

indicating the lower limit for the fully rough turbulent flow was obtained by substituting $\frac{u_* k_s}{\nu} = 70$ in equation 2.9.

3.2.2 The Skewed Boundary Layer

Figure 3.13 shows the velocity distribution in the upper flow layer for experiment A2. To indicate the region of deflected flow caused by the groyne, the stream-lines were computed by graphically integrating the velocity vectors. It can be seen that for this groyne length (0.5 ft.) the flow disturbance extended to the opposite flume wall. The stream line with $\psi = 0$ denotes the stream-line of separation. The region bounded by the upstream reference section, the $\psi = 0$ line, the flume wall opposite to the groyne and the cross-section where the separated streamline reattaches itself to the wall on the side of the groyne could be referred to as the deflected flow region.

3.2.2.1 The Polar Plot Model

In the deflected flow region, for the upstream part (x negative) and for the immediate downstream part up to $\frac{x}{b}$ of about 1.0, the experimental results showed that the velocity profiles were

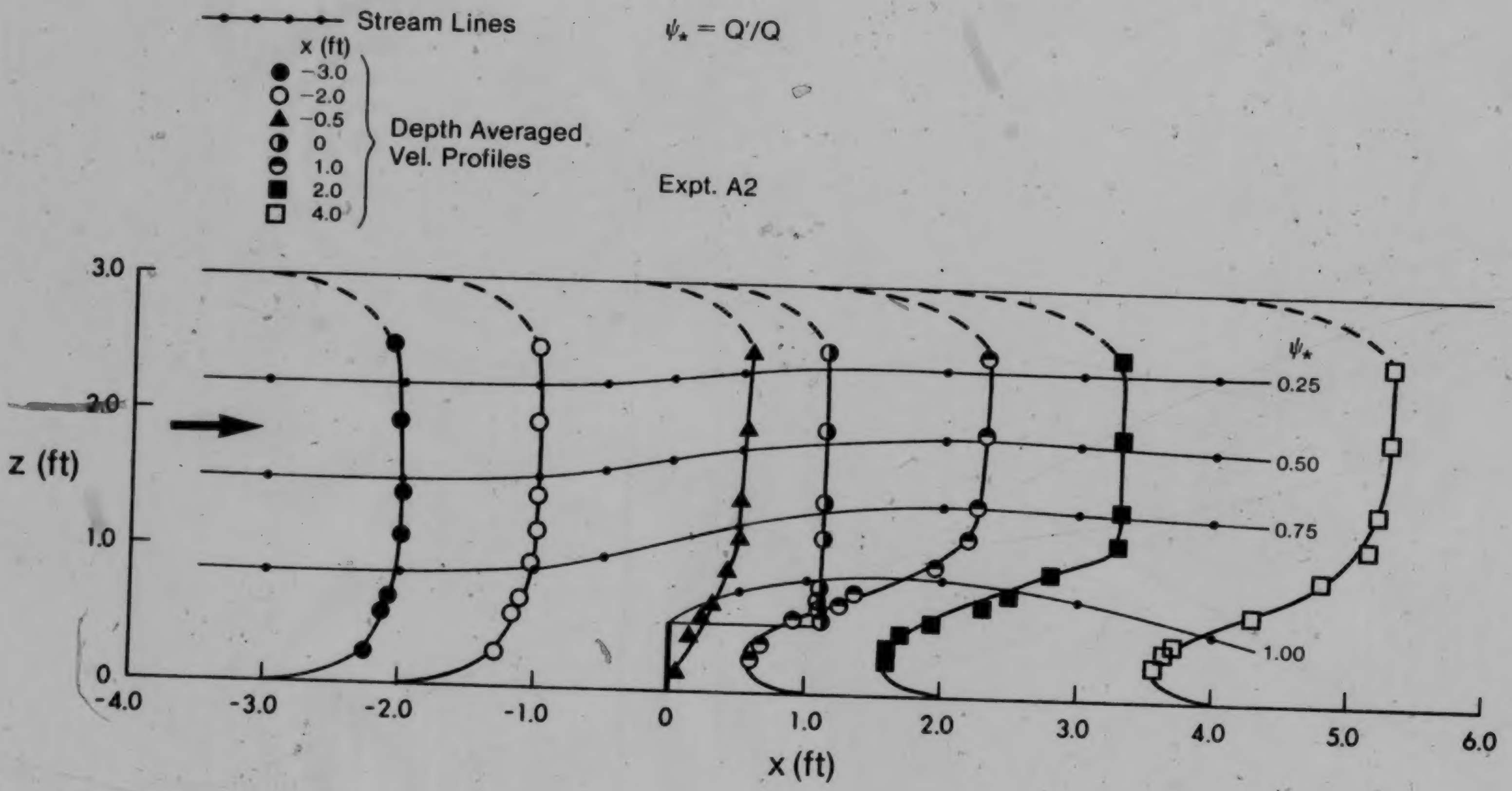

Figure 3.13 Stream Lines Near a Groyne

described by Johnston's polar plots (see Figure 3.4). If y_* is the value of y at the apex of the polar triangle, $\frac{y_* u_*}{\nu}$ was found to vary from about 20 to 300 with all profiles upstream of the groyne having a value less than 150. Johnston (1960) suggested that the highest value of $\frac{y_* u_*}{\nu}$ was about 16. However, Hurnung and Joubert (1963) carried out a more detailed experimental investigation of the phenomenon in a three dimensional boundary layer generated by a circular cylinder and found that $\frac{y_* u_*}{\nu}$ ranged upto 150 in the heavily skewed zone upstream of the cylinder. In the inner region where $y<y_*$ the velocity data (see Figure 3.14) are described reasonably well (considering the rather small thickness of this layer) by the logarithmic law of the wall

$$\frac{u}{u_*} = 5.75 \log \frac{y u_*}{\nu} + 5.5$$

If α is the angle through which the upper layer has turned with respect to the approaching flow and β is the angle of the defect velocity with the velocity vector of the upper layer (see Figure 3.15(a)) Johnston, and Hornung and Jourbert found that for their skewed boundary layers, $\beta \approx 2\alpha$. The results of the present study (shown in Figure 3.16) indicates that $\beta \approx 3\alpha$. Further, if ω is the angle through which the inner layer has turned with reference to the approaching flow (also the angle of bed shear stress), then $(\omega-\alpha)$ represents the excess angle of the inner layer with reference to the upper layer. The variation of $\frac{\omega-\alpha}{\alpha}$ with $z' = \frac{z-b}{b}$ is studied in Figure 3.17(a). The results indicate that for x from -2.0 to 0.5 ft., a mean curve could be drawn through the data and for this mean curve $\frac{\omega-\alpha}{\alpha}$ decreases from about 6 for $z' \approx -0.5$

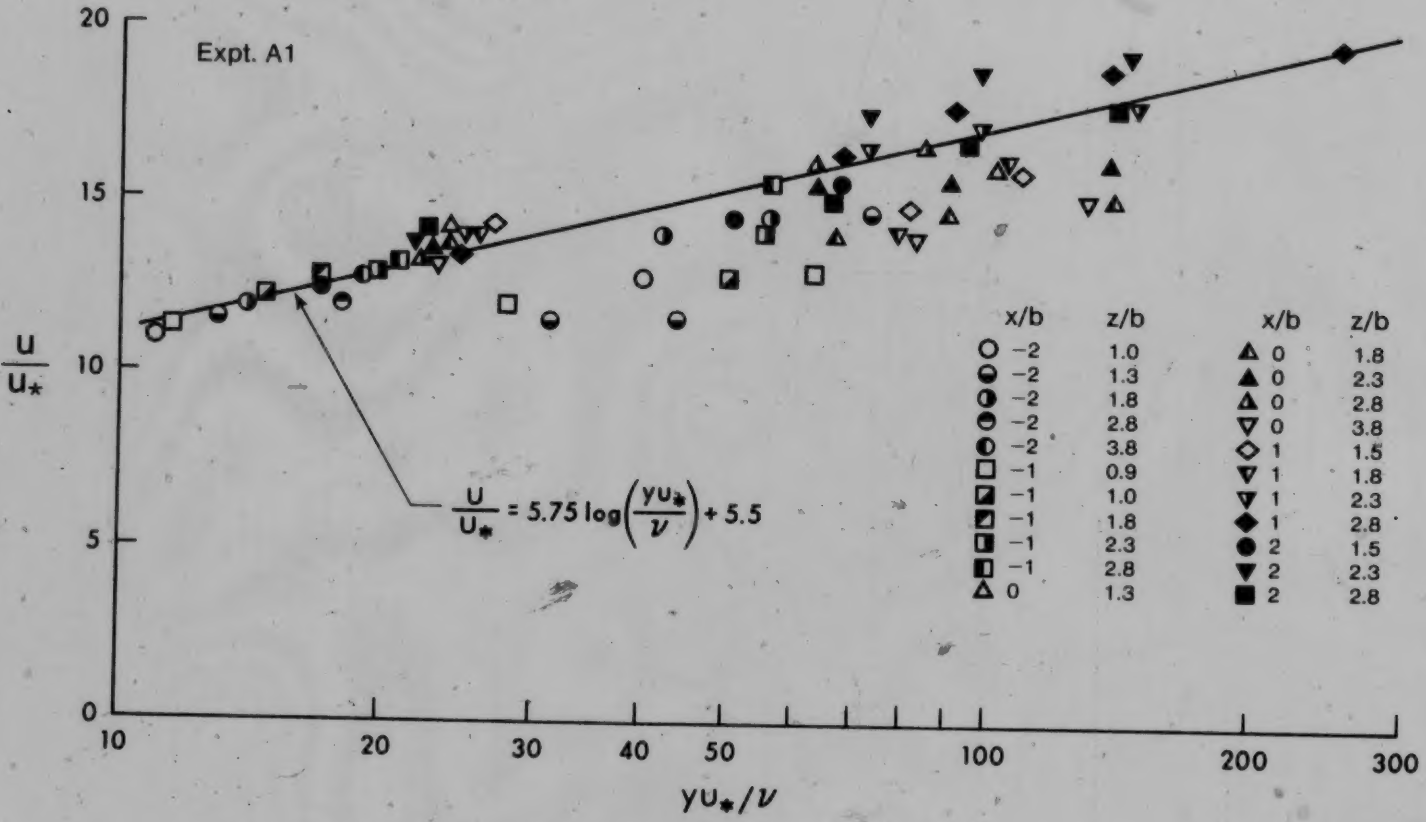

Figure 3.14 Law of the Wall in the Inner Layer

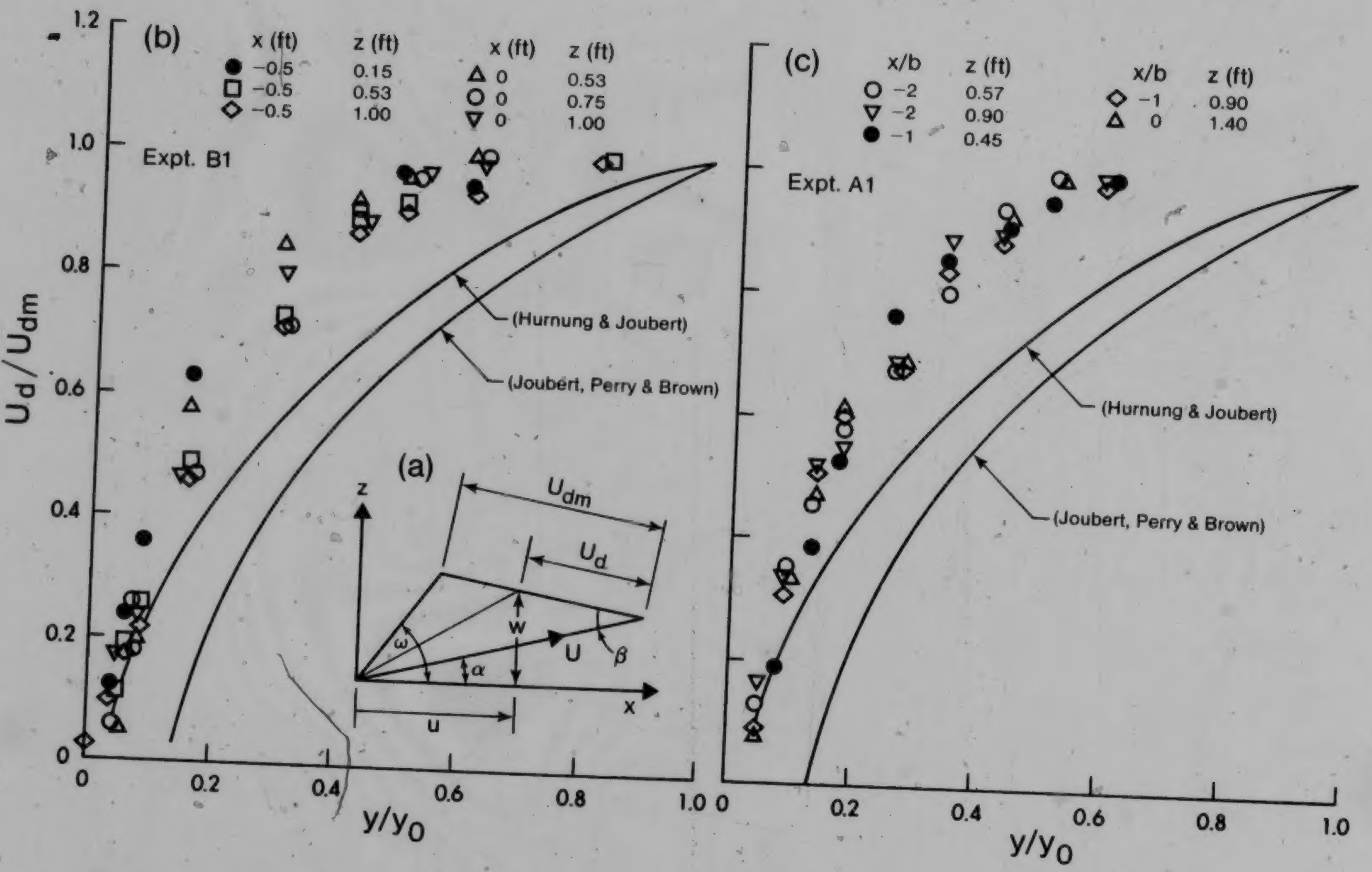

Figure 3.15 Velocity Defect Profiles in Skewed Flow

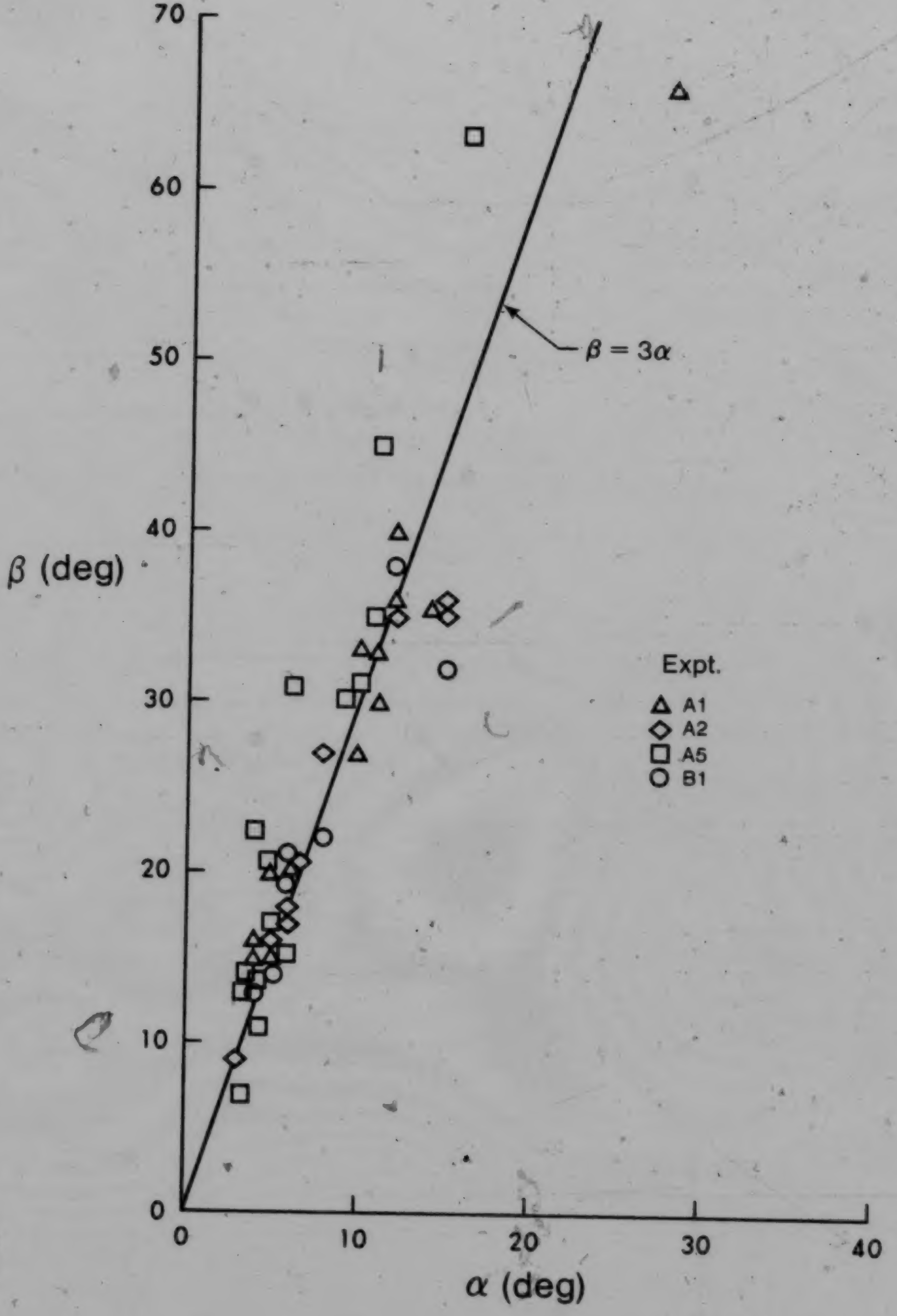

Figure 3.16 Behaviour of the Characteristic Angles in Skewed Flow

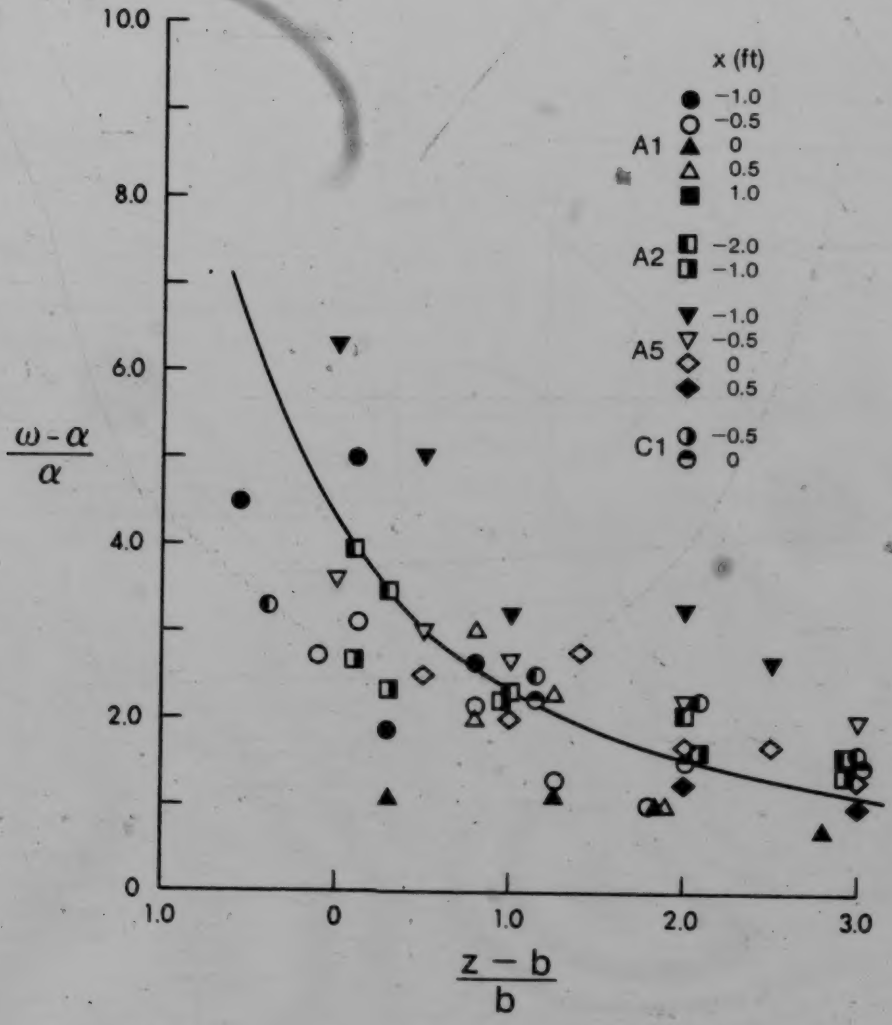

Figure 3.17 Turning Angle of Shear Stress

to about 1.0 for z' = 3.0.

3.2.2.2 The Velocity Defect

With reference to Figure 3.15(a), if U_d is the velocity defect at any normal distance y from the bed and if U_{dm} is the maximum value of U_d, Hornung and Joubert found that in the skewed boundary layer produced by a cylindrical obstacle, the plots of the dimensionless velocity defect $\frac{U_d}{U_{dm}}$ against dimensionless distance $\frac{y}{\delta}$ (where δ is the boundary layer thickness) correlated in a very narrow band. Johnston (1967) plotted his data and some others by this scheme and found that the profiles for each set of data were similar but different from one another or the curve obtained by Hornung and Joubert. The results of experiments A1 and B1 show that the defect profiles for the present study are also similar and different from the profiles of Hornung and Joubert and considerably different from the mean curve from the plot given by Johnston (see Figure 3.15(b and c)). In Figure 3.15(b and c) the distance y from the bed was normalized on the approach flow depth, y_o. The result of a preliminary attempt to predict the defect scale is shown in Figure 3.18 wherein $\frac{U_{dm}}{U}$ is plotted against $z' = \frac{z-b}{b}$ for experiments A1 and A5 with the groyne length b = 6 inches and for experiment B1 with b = 3 inches. Although considerable scatter is evident, it appears possible to draw a mean curve which shows that $\frac{U_{dm}}{U}$ decreases continuously with z' from about 0.7 at z' = 0 to about 0.27 at z' = 3.0.

3.2.2.3 The Upper Potential Flow Layer

The flow layer above the region defined by the triangular model in the skewed zone is referred to as the upper potential flow layer

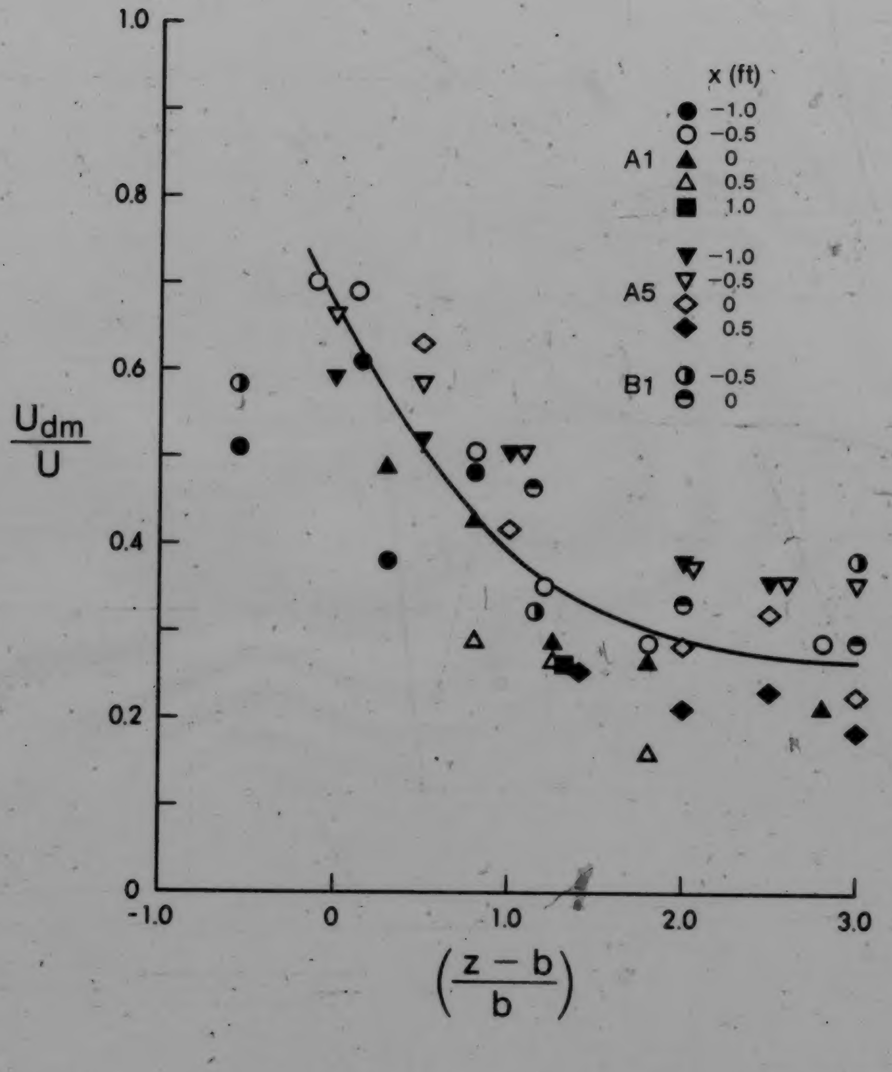

Figure 3.18 Behaviours of the Velocity Defect Scale

neglecting the dip near the surface. To present the measurements on the characteristics of this upper layer, if U_o is the velocity of the upper layer in the approaching flow and if U is its value at any location in the deflected flow region, the variation of $\frac{U}{U_o}$ against $\frac{x}{b}$ is shown in Figure 3.19 for the A series for different values of $\frac{z}{b}$. The mean curves of Figure 3.19 are collected together in Figure 3.20 which shows that for $\frac{z}{b} = 1$ and 1.5, $\frac{U}{U_o}$ decreases below unity while approaching the groyne and increases thereafter to about 1.2 at the groyne section. For $\frac{z}{b} = 2.0$, 3.0 and 4.0, $\frac{U}{U_o}$ does not decrease below unity but increases continuously to reach peak values of about 1.45 downstream of the groyne.

The variation of $\frac{U}{U_o}$ with $\frac{x}{b}$ for various values of $\frac{z}{b}$ for the 3-inch groyne is shown in Figure 3.21 and in a consolidated form in Figure 3.20(b). From these figures, it is seen that these profiles are similar to those for the 6-inch groyne but the maximum values of $\frac{U}{U_o}$ are smaller. Based on the results of Cunha (1971, 1973) it appears the results for the 3-inch baffle for which $\frac{b}{B} \simeq \frac{1}{12}$ or $\frac{B-b}{b} = 0.92$ might represent the asymptotic case, that is, the constriction ratio for which the effect of constriction on the channel flow is small.

The variation of the deflection angle of the upper flow layer α with $\frac{x}{b}$ at various transverse axis $\frac{z}{b}$ for the series A experiments is shown separately in Figure 3.22(a to e) and together in Figure 3.22(f). For these curves, α reaches the maximum value of α_m approximately at the location of the groyne and then decreases steadily to assume a small negative value further downstream. Figure 3.23 shows a similar analysis for the series B experiments with a 3-inch groyne and includes the mean curves for the A series. It is interesting to see that these curves for the 6-inch groyne describes satisfactorily the α variation for the

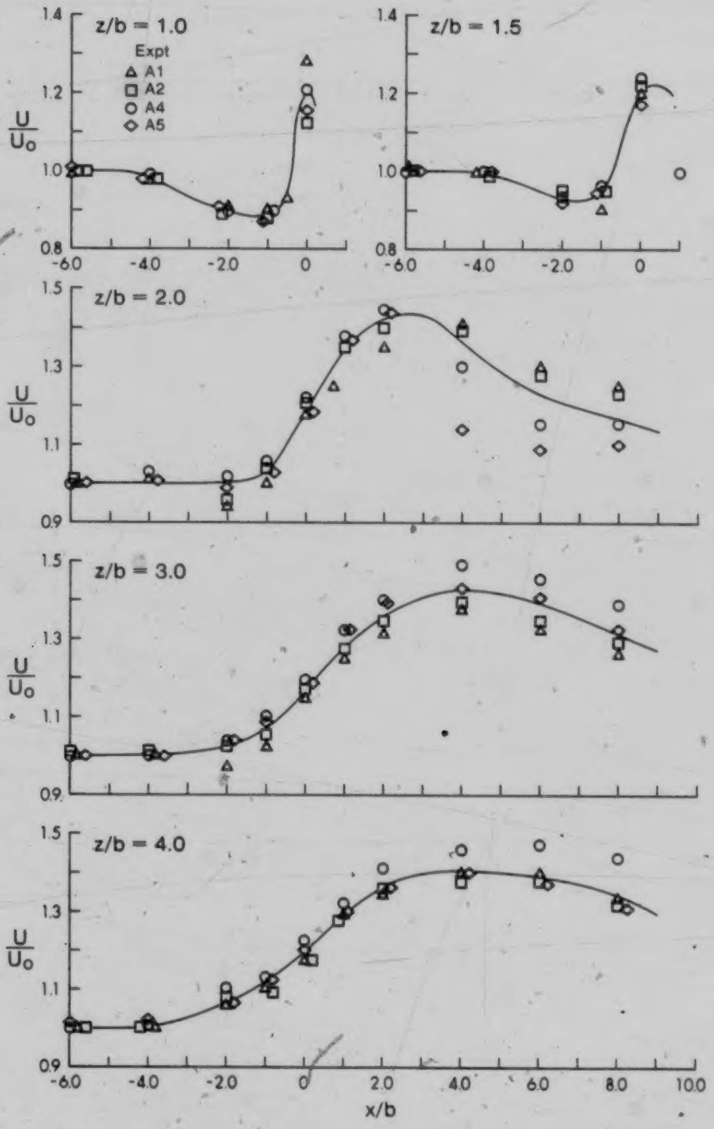

Figure 3.19 Velocity of the Upper Layer (Series A)

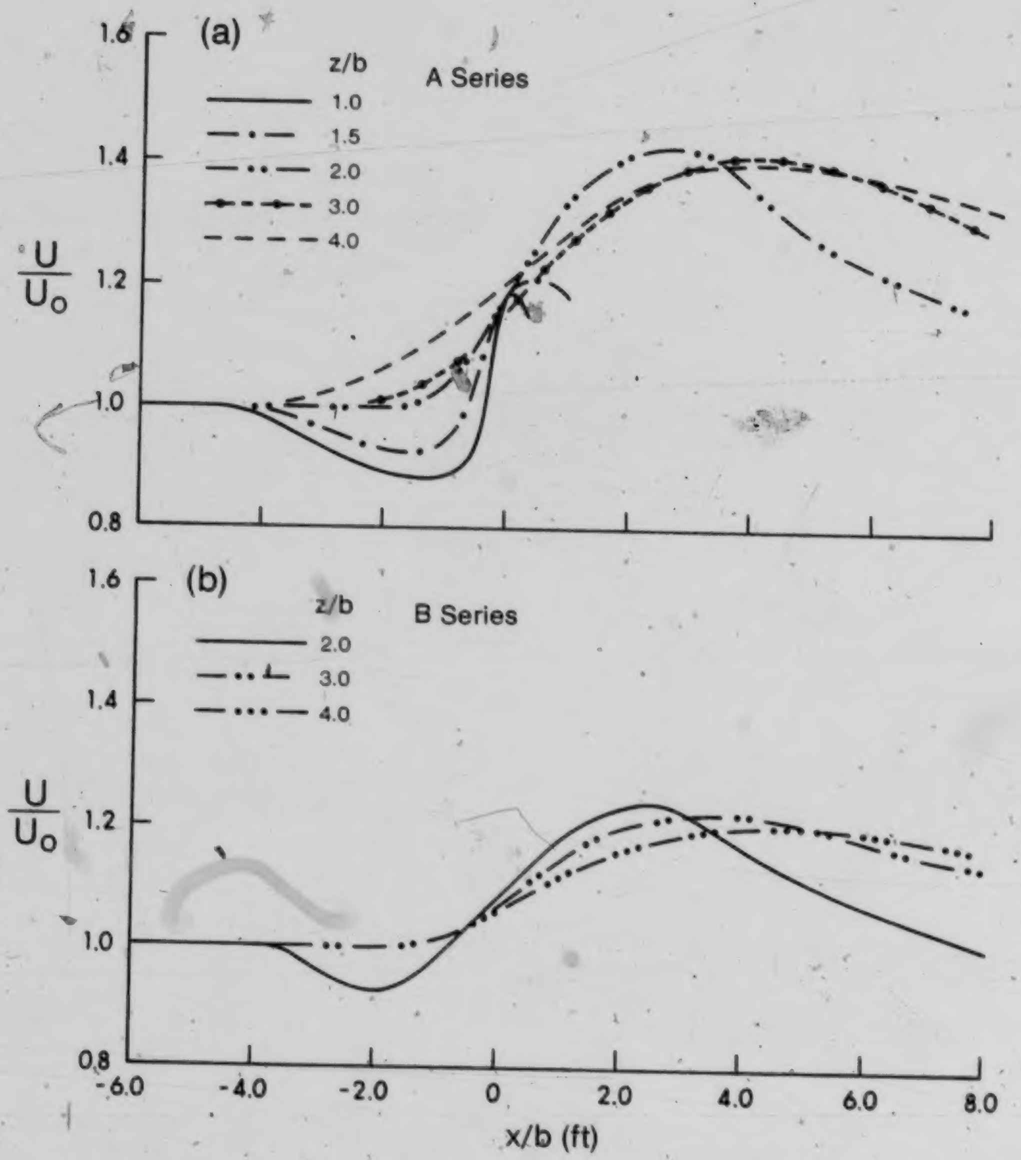

Figure 3.20 Combined Upper Layer Velocity Profiles

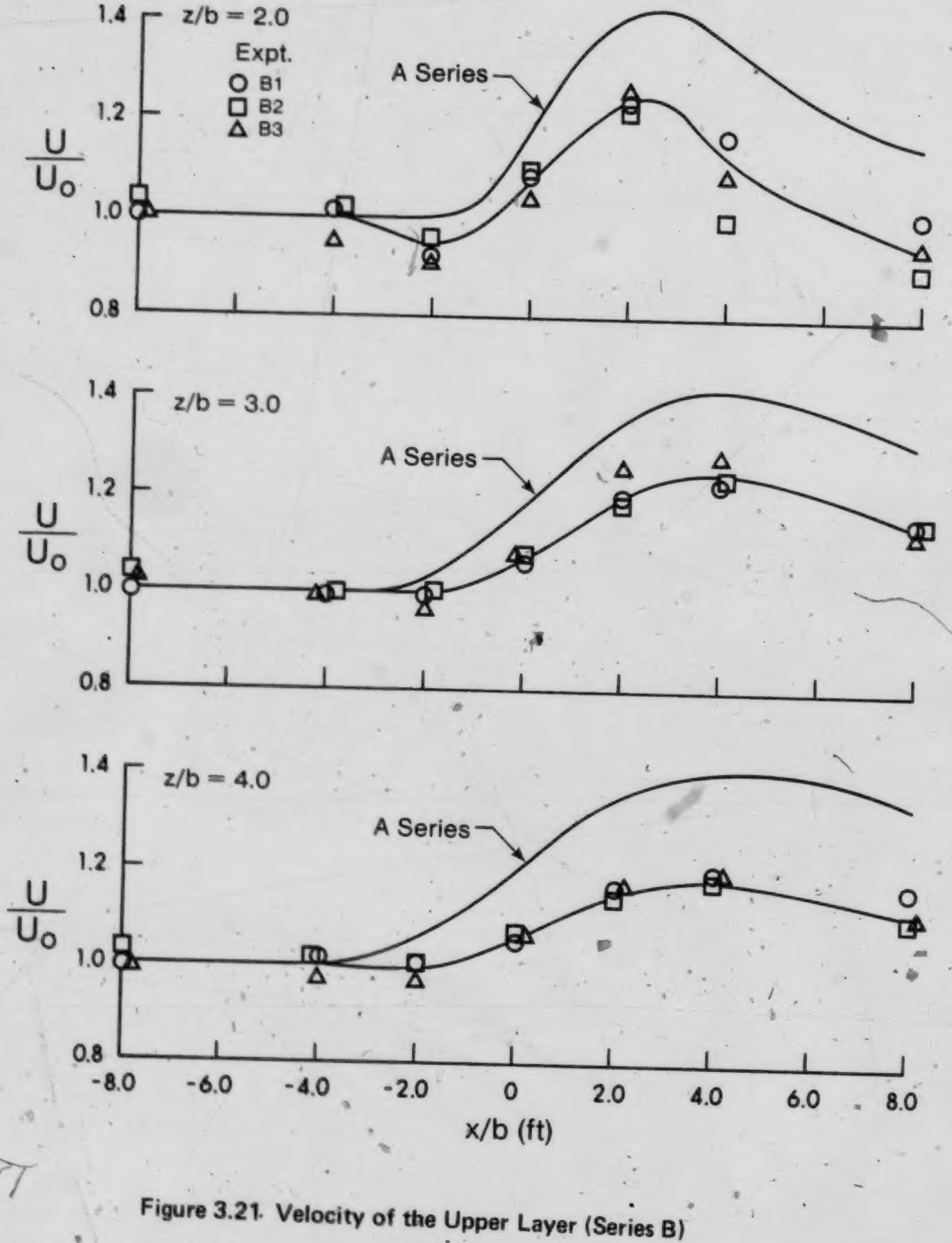

Figure 3.21. Velocity of the Upper Layer (Series B)

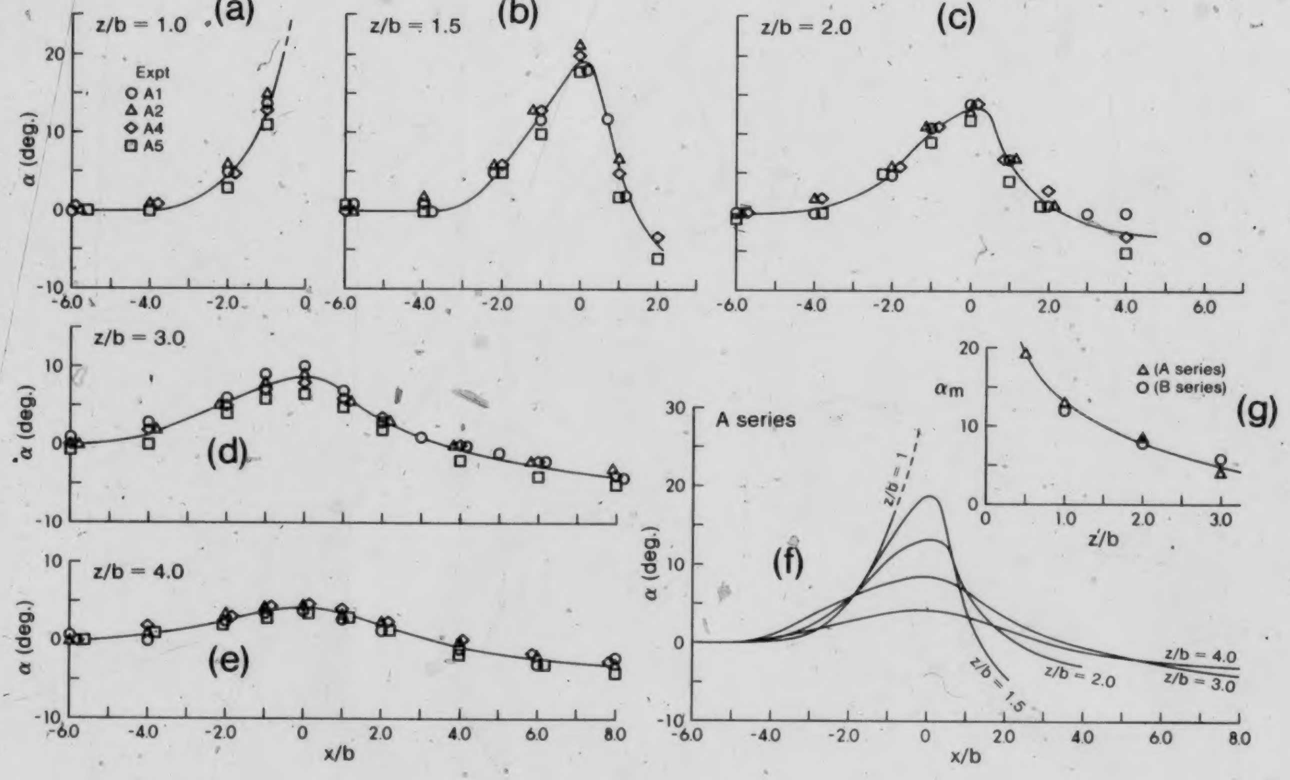

Figure 3.22 Angle of the Deflected Flow (Series A)

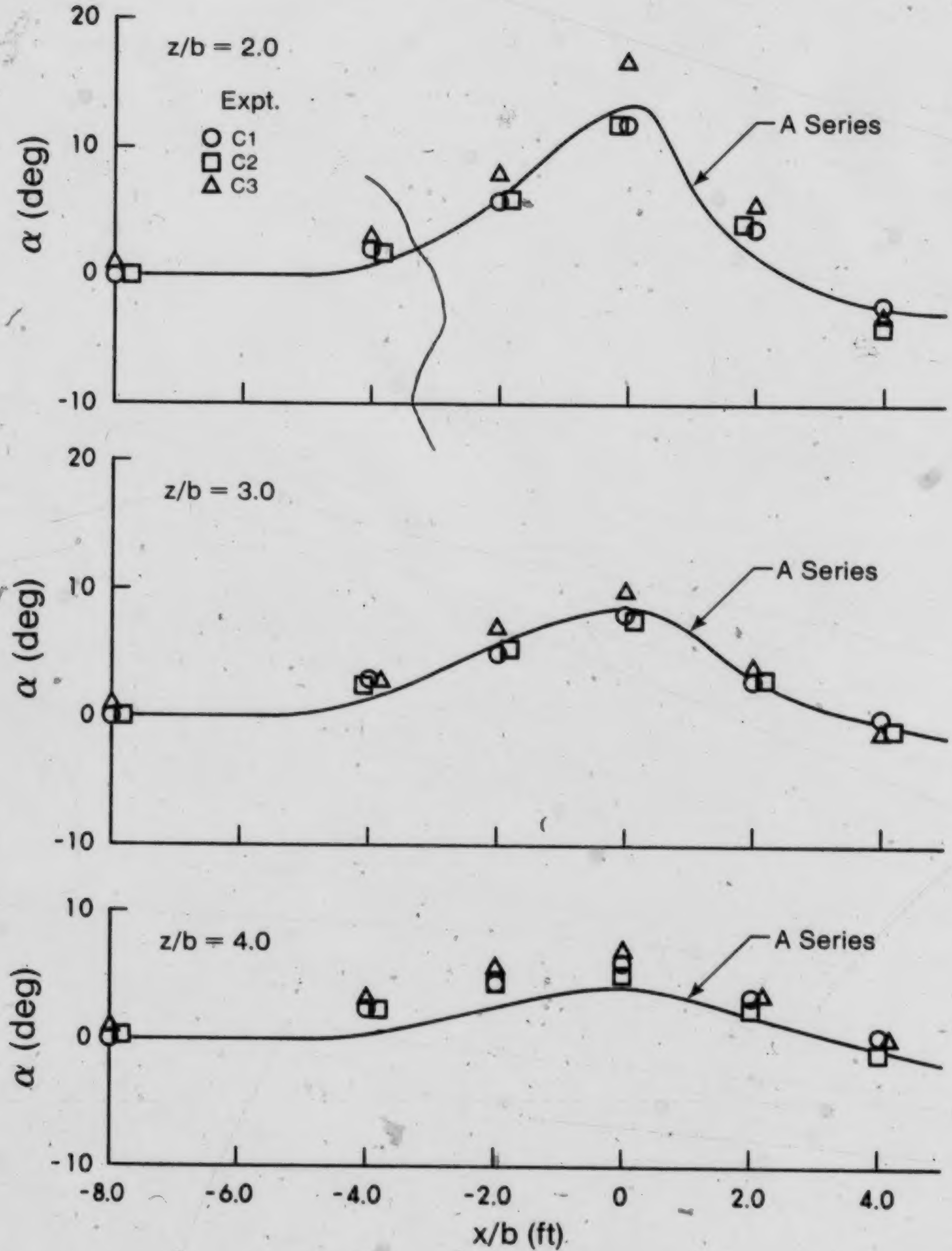

Figure 3.23 Angle of the Deflected Flow (Series B)

3-inch groyne thereby lending some general importance to the α variation curves. For the maximum value of the deflection angle α_m occuring approximately at the groyne, Figure 3.22(g) shows that one curve could be drawn to describe the results of both the 6-inch and 3-inch groynes and that α_m decreases from about 20 degrees at $\frac{z'}{b} = 0.5$ to about 5 degrees at $\frac{z'}{b} = 3.0$.

3.2.3 Bed Shear Stress Field

The typical bed shear stress variations presented earlier (see Figure 3.5) showed that for any given value of $\frac{z}{b}$, the bed stress τ_o increases from τ_{oo} to a maximum value of τ_{om} near the groyne and then decreases on the downstream side. The values of $\frac{\tau_{om}}{\tau_{oo}}$ for the different experiments are shown in Table 2.1. For the A series, this ratio is about 5 whereas for the B series, it is about 3. Thus, the degree of constriction appears to affect the shear stress amplification near the groyne. For the 6-inch groyne with the sand-paper roughness (series C), slightly higher amplification is indicated (Table 2.1), but since in these experiments the flow was not fully rough turbulent, no signicance can be associated with the higher amplification. Maximum shear stress in experiment D could have provided a better assessment on the effect of roughness but the data was not obtained due to intense turbulence causing instrument vibration at the location.

3.2.3.1 Similarity of Shear Stress Curves

The bed shear stress curves shown in Figure 3.5 were analysed for similarity. For the analysis, it was necessary to present the curves in dimensionless form. Thus, the shear stress τ_o, was normalised by the approach shear stress τ_{oo} and x, z, were normalised by the groyne length b. The dimensionless plots resemble those of Figure 3.5 and have not been shown here. However, if $\frac{\Delta\tau_o}{\Delta\tau_{om}}$ is plotted against $\frac{x'}{b}$ wherein $\Delta\tau_o = \tau_o - \tau_{oo}$, $\Delta\tau_{om} = \tau_{om} - \tau_{oo}$, $x' = x - x_m$, x_m being the location of τ_{om}, as shown in Figure 3.24, it is seen that on the upstream side of x_m, a mean curve could be drawn to describe approximately the data of present experiments. On the downstream side of the location of τ_{om}, the $(\frac{\Delta\tau_o}{\Delta\tau_{om}})$ vs. $\frac{x'}{b}$ profiles depend for their shape on the value of $\frac{z'}{b}$. These upstream and downstream profiles were replotted with $(\frac{\Delta\tau_o}{\Delta\tau_{om}})$ versus $\eta_\tau = \frac{x'/b}{(x'/b)_{1/2}}$ where $(x'/b)_{1/2} = (x'/b)$ at $(\frac{\Delta\tau_o}{\Delta\tau_{om}}) = 0.5$ and as shown in Figure 3.25(a) all these profiles could be described by one curve and this curve is described satisfactorily by the exponential equation

$$\frac{\Delta\tau_o}{\Delta\tau_{om}} = e^{-0.693\eta_\tau^2}$$

The variation of the length scale $(x'/b)_{1/2}$ with z'/b is shown in Figure 3.25(b). For the downstream side of x_m, $(x'/b)_{1/2}$ increases with z'/b whereas for the upstream side, $(x'/b)_{1/2} \simeq 1.6$.

3.2.3.2 Shear Stress Amplification Along Various Transverse Locations

The variation of $(\Delta\tau_{om}/\tau_{oo})$ with z'/b for the different experiments is studied in Figure 3.25(c) which shows that a mean curve could be drawn to represent most of the results and $(\Delta\tau_{om}/\tau_{oo})$ decreases continuously as z'/b increases from about 4.0 at $z'/b = 0$ to about 0.75

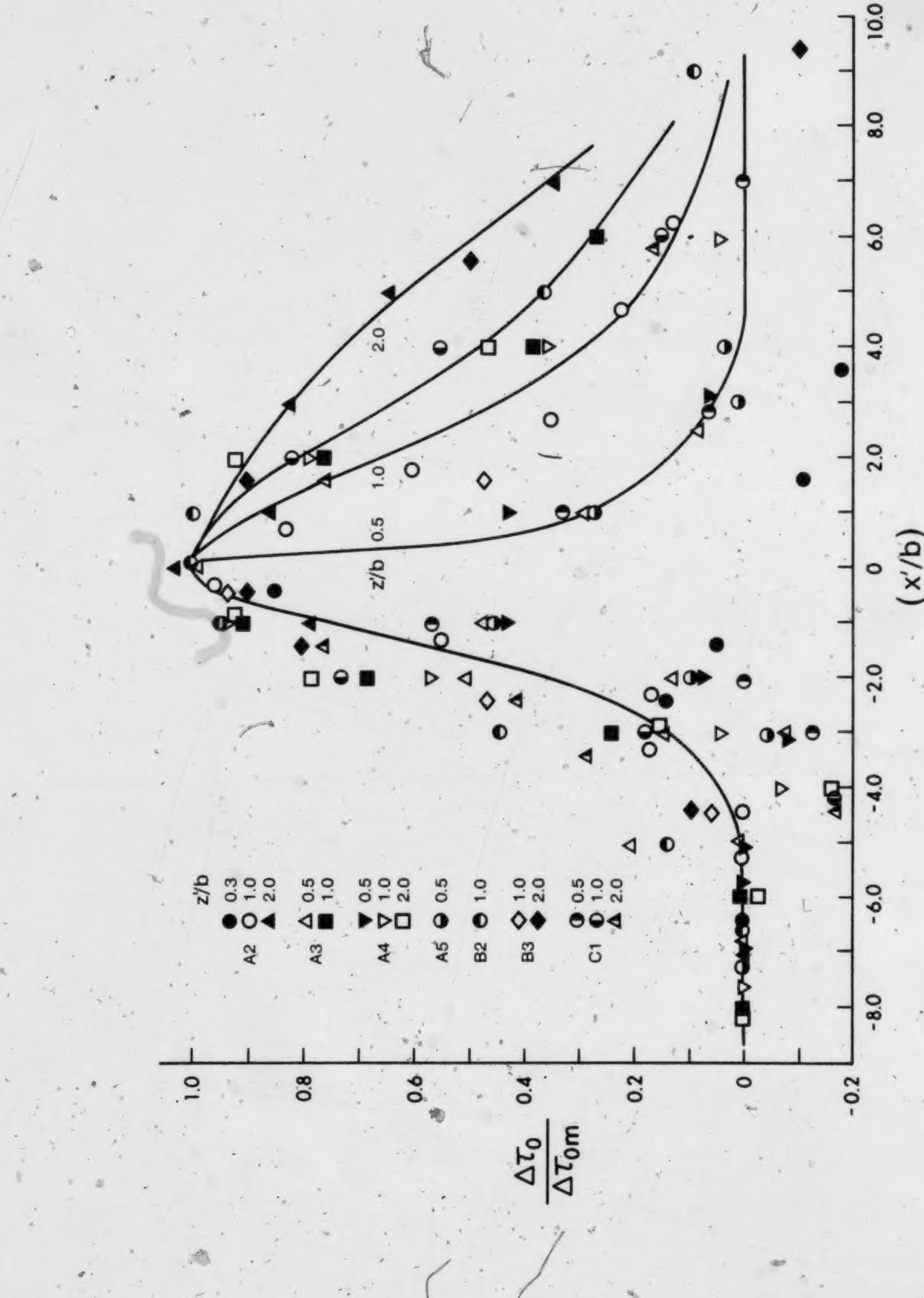

Figure 3.24 Behaviour of Excess Bed Shear Stress

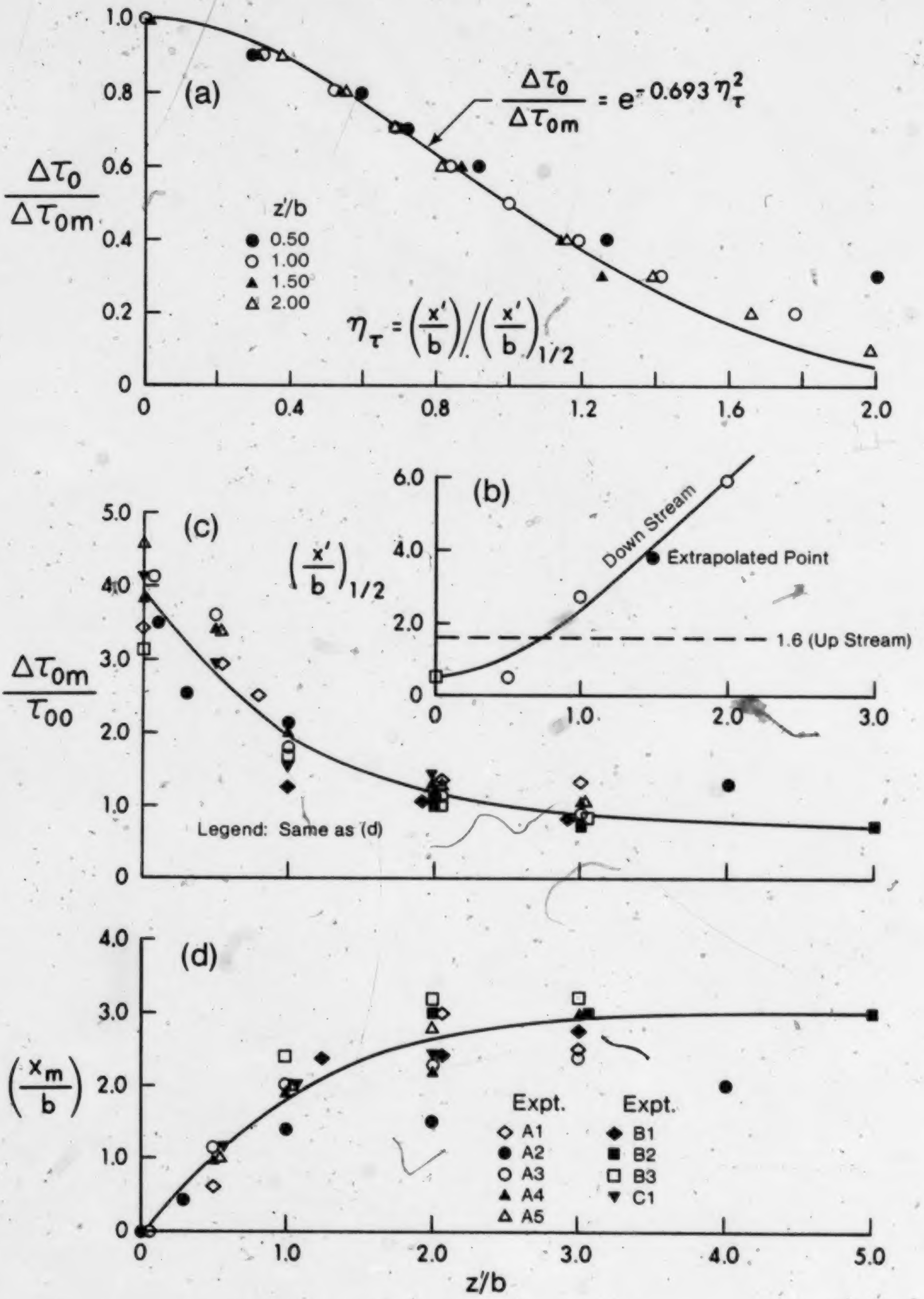

Figure 3.25 Similarity Curves and Scales for Excess Bed Shear Stress

at $z'/b = 5.0$. It would be interesting and useful to perform further experiments with larger values of b/B to test the validity of this curve for the larger values of b/B.

The variation of x_m/b with z'/b is studied in Figure 3.25(d). Here again, it appears that a mean curve could be drawn through the data of most experiments and x_m/b increases continuously with z'/b upto $z'/b \approx 3.0$ and for $z'/b \overset{\sim}{>} 3.0$, x_m/b approaches an asymptotic value of 3.0.

3.2.3.3 Angle of the Shear Stress

If ω is the angle of the shear stress with the longitudinal direction of the undisturbed flow, the variation of ω with x/b for the different values of z/b is shown in Figure 3.26(a) where one curve could be drawn to describe the results of A series of experiments. Figure 3.26(b and c) show that the mean curves drawn in Figure 3.26(a) describe satisfactorily the results of the short groyne and those with the rough beds. If ω_m is the maximum value of ω, Figure 17(b) shows that one curve describes most of the results. In Figure 17(b) it is seen that ω_m decreases from about 60 degrees at $z'/b = 0$ to about 2 degrees at $z'/b \approx 8.5$. With these results, the bed shear field in comparative situations could be calculated.

3.2.4 The Shear Layer

On the downstream side of the groyne, the region that lies between the outer plane of the deflected flow, defined approximately by the separating stream line ($\psi = 0$ in Figure 3.13) and the side wall on the side of the groyne, resembles a shear layer from the configuration

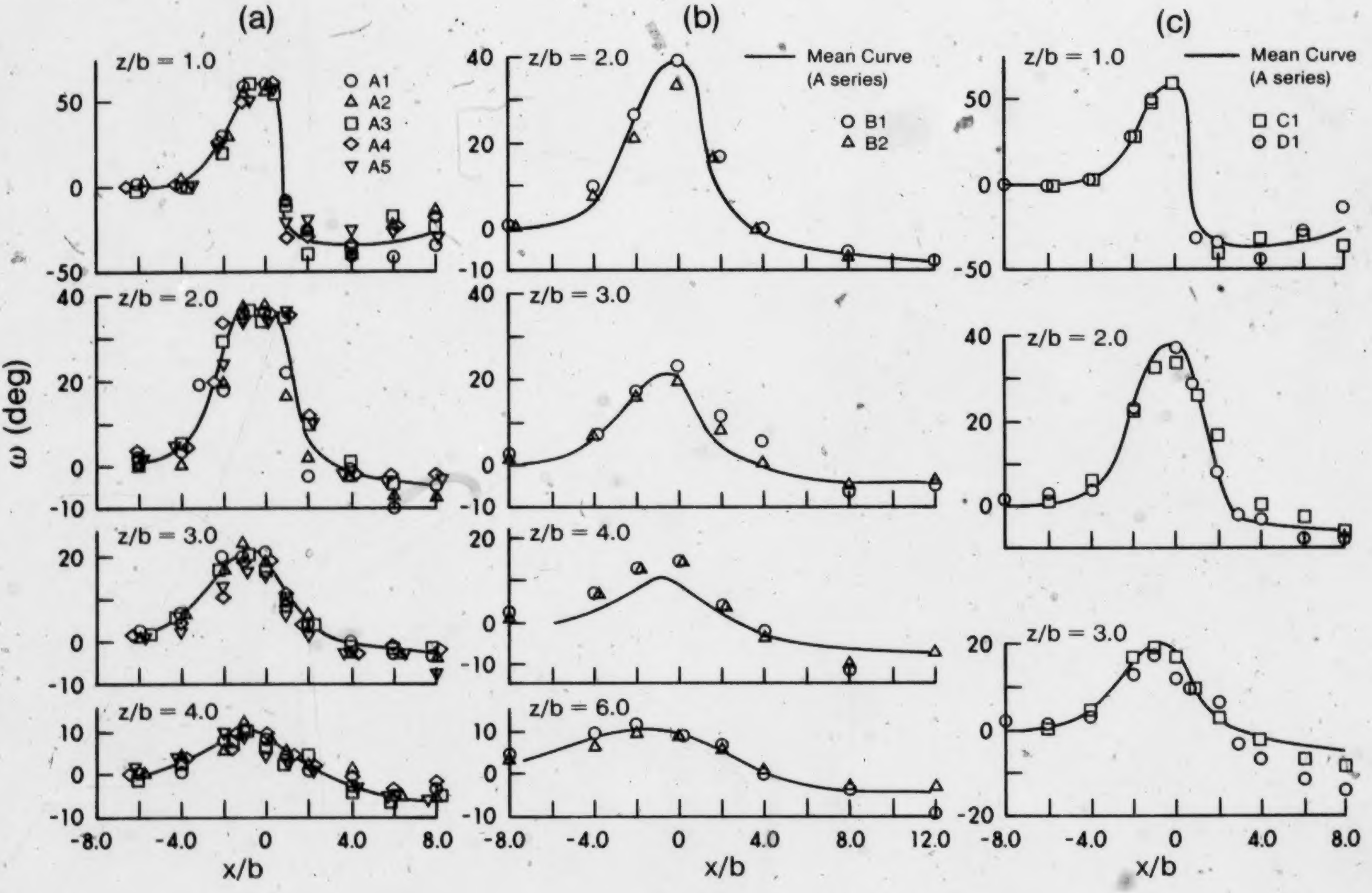

Figure 3.26 Turning Angles for the Bed Shear Stress

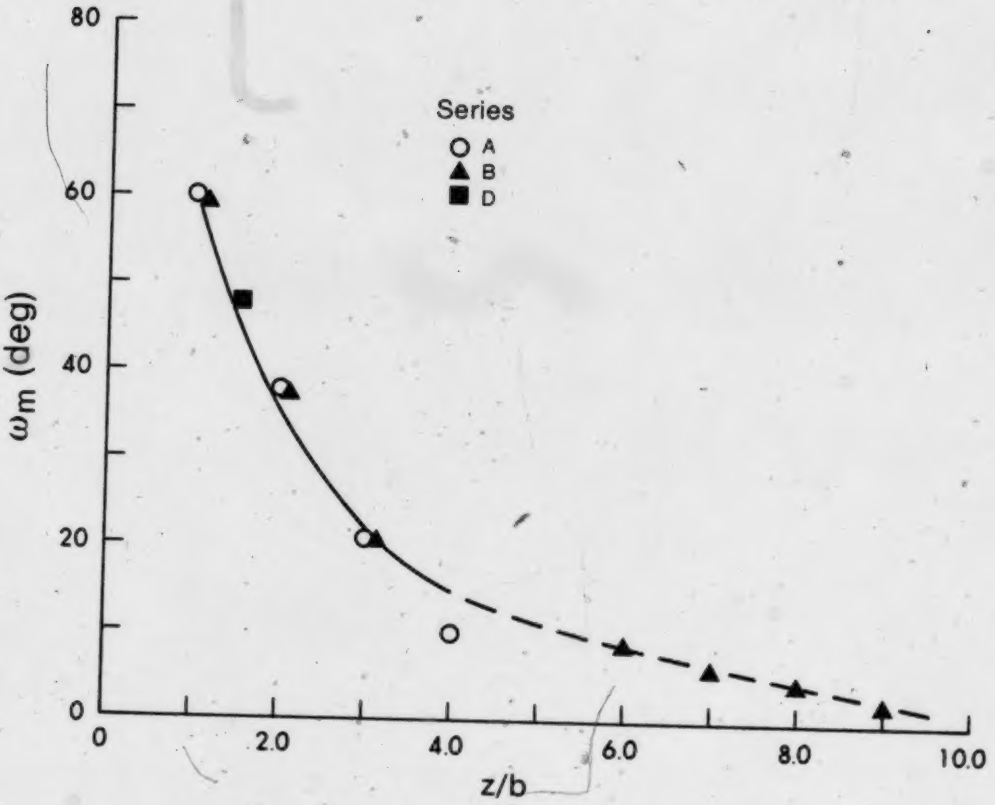

Figure 3.26(d) Variation of Maximum Turning Angle of Shear Stress

of the velocity profiles in that region (see Figure 3.8). The outer edge of the shear layer in any horizontal plane is taken as the point where the velocity either approaches the velocity of the deflected flow (Figure 3.27b) or reaches a maximum value (Figure 3.27a). The inner edge is fixed at the point where the absolute magnitude of the negative velocity reaches the maximum value.

The configuration of the outer boundary of the shear layer for the upper flow layer is shown in Figure 3.28(a) from the results of the A series. This figure also shows the separating stream line as computed from the free-stream line theory (see Appendix A). The stream line for $\psi = 0$ as determined from the actual velocity measurements is also shown. Figure 3.28(b) shows in addition the range of the outer boundary near the bed for the A series of experiments. From these figures it could be said that the outer boundary plane of the shear layer through the depth of flow is not vertical; it is tilted towards the backward flow region near the bed. This phenomenon is also implicit in Figure 3.9 and also verified visually in a dye test. Secondly, the $\psi = 0$ line as determined from velocity measurements in the upper layer is displaced more into the backward flow region than the theoretical free stream line. In general, the theoretical free stream line fairly coincides with the outer boundary of the shear layer close to the bed (Figure 3.28b).

3.2.4.1 Geometry of the Eddy Zone

The theoretical free stream line tends to grow infinitely wide with increasing downstream distance because the theory does not account for the flow interaction in the two zones that the line separates. In reality, the free stream line has two segments as represented in Figure 3.28 by curve 3. In the first segment, the stream line, $\psi = 0$

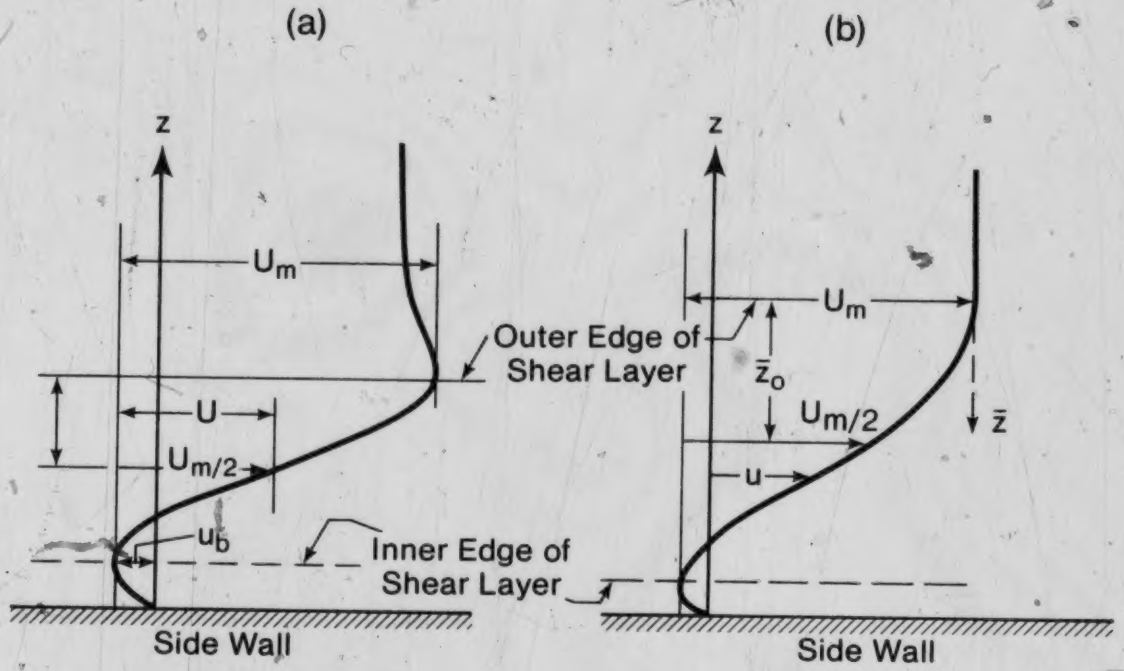
(a)
(b)
z
z
U_m
U_m
Outer Edge of Shear Layer
U
$U_{m/2}$
$U_{m/2}$
u_b
u
$\bar{z}_o$
$\bar{z}$
Inner Edge of Shear Layer
Side Wall
Side Wall

Figure 3.27 Definition Sketch for Shear Layer

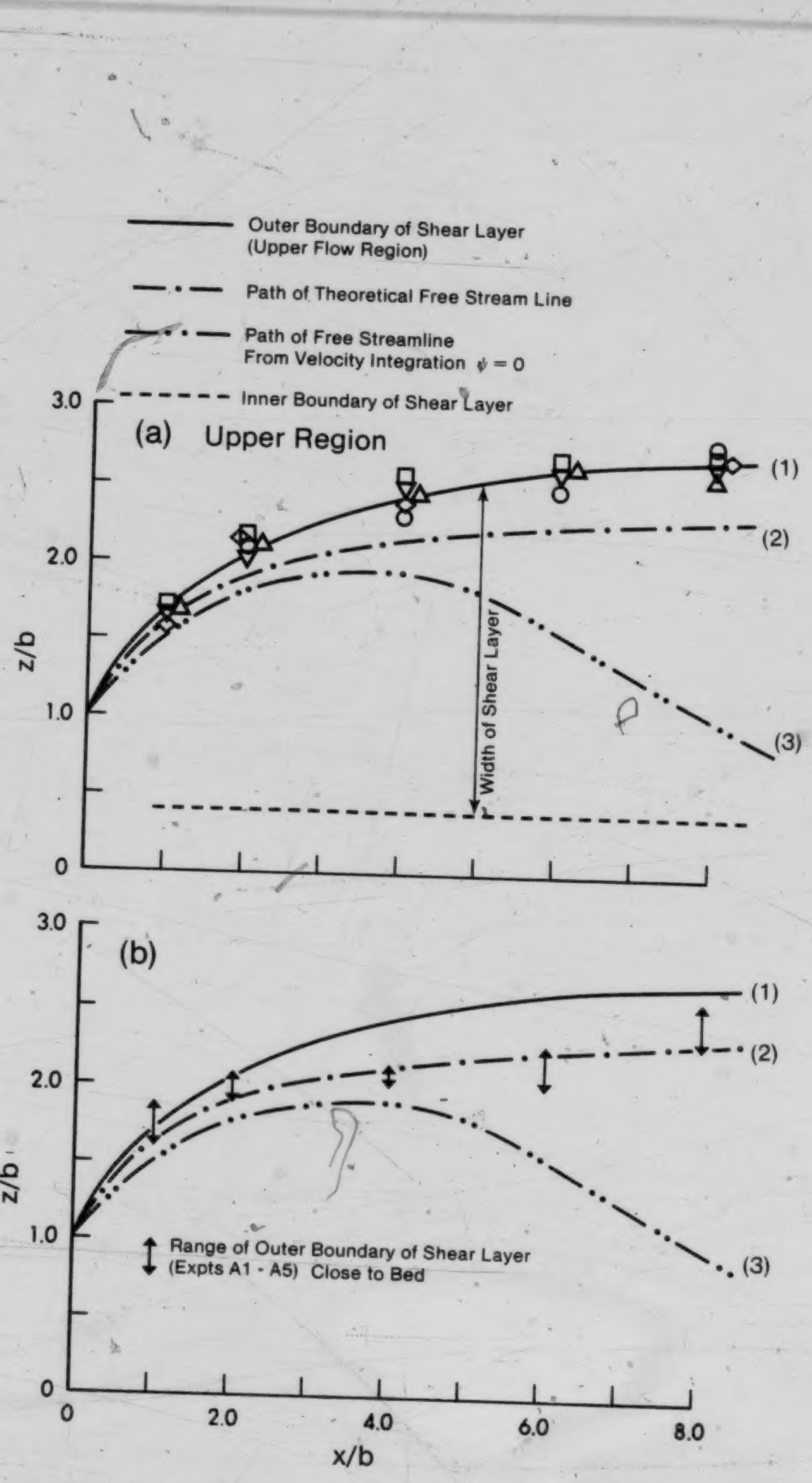

Figure 3.28 Boundaries of the Shear Layer

continuously grows wider from the groyne nose until it attains a maximum width of $z/b \approx 2$ at $x/b \approx 4.0$. The second segment extends from this maximum point to the reattachment point at $x/b = 12$. The region that lies between these segments and the flume wall on the side of the groyne is referred to as the eddy or recirculation zone. Thus, the eddy zone is about six times as long as it is wide. The dimensions of the eddy zone from this study are consistent with those reported by Francis and Pattanaik (1968).

3.2.4.2 Similarity of Velocity Profiles in the Shear Layer

The velocity profiles in the shear layer were tested for similarity by plotting $\frac{U}{U_m}$ against $\frac{\bar{z}}{\bar{z}_o}$ wherein $U = u - (u_b)$, U_m is the maximum value of U, $\bar{z}_o = \bar{z}$ where $U \cong \frac{1}{2} U_m$ (see Figure 3.27). These profiles were picked for two typical levels of $\frac{y}{y_o} = 0.85$ and 0.03. The dimensionless plots are shown in Figure 3.29(a) for the higher level and Figure 3.29(b) for the lower level. Both figures show that the profiles are similar and that the similarity curve is well described by the exponential curve, $\frac{U}{U_m} = e^{-0.693\eta_z{}^2}$ where $\eta_z = \bar{z}/\bar{z}_o$.

If z_i is the distance of the inner boundary of the shear layer, the experimental results showed that $z_i/b \approx 0.4$. If $\bar{b}$ is the width of the shear layer, the variation of $\bar{b}/b$ with x/b for the upper flow region is shown in Figure 3.30(a). The growth of the shear layer for x/b up to 8.0 is approximately linear and the shear layer is somewhat wider in the upper region than in the lower region (see Figure 3.30b). The rather limited results of the B series agreed well with the above results.

The velocity scale U_m for the shear layer for x/b upto about 8 was approximately constant and U_m/V, wherein V is the mean velocity of

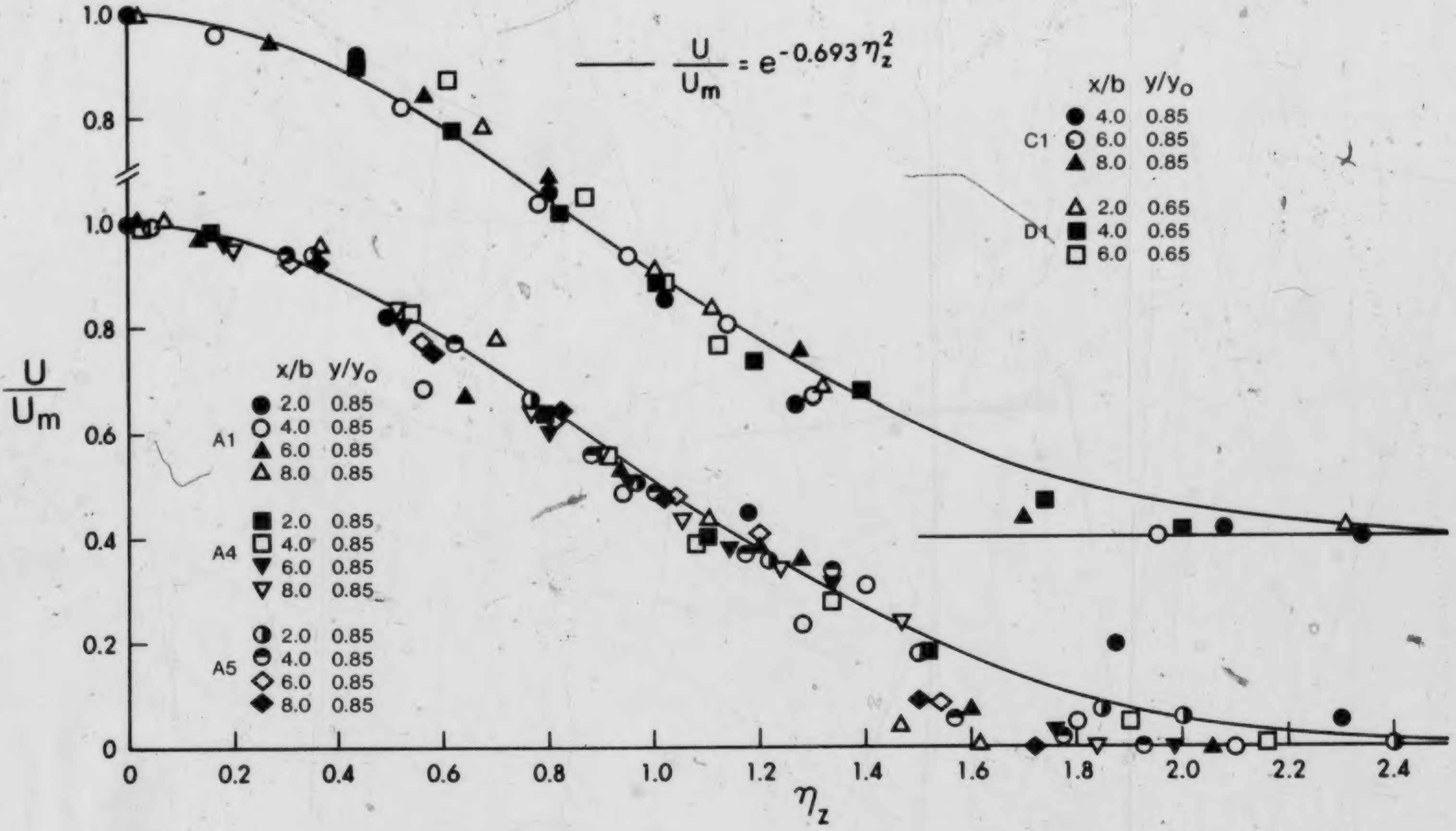

Figure 3.29 (a) Similarity of Velocity Profiles for the Shear Layer (Upper Layer)

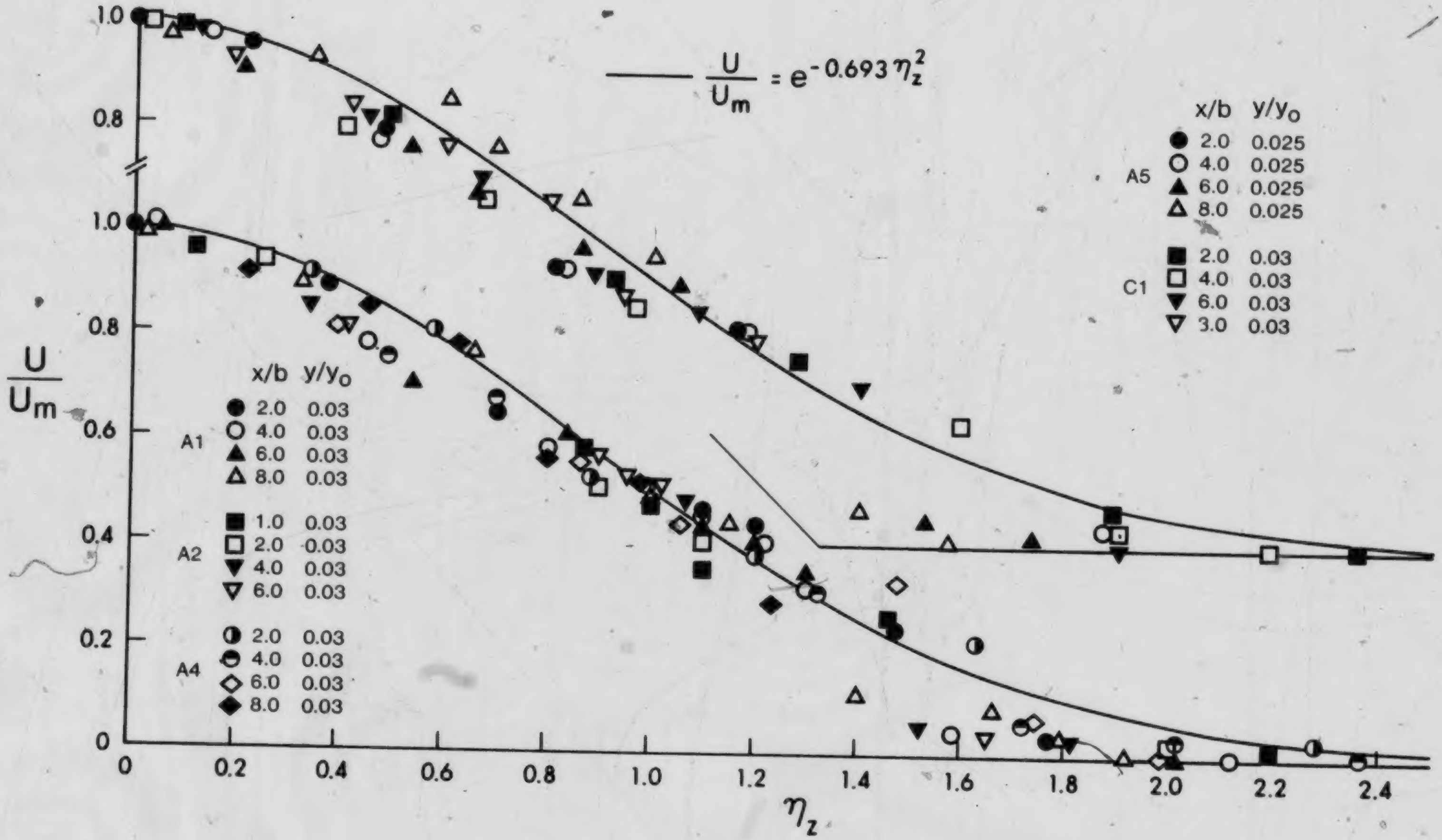

Figure 3.29 (b) Similarity of Velocity Profiles for the Shear Layer (Lower Layer)

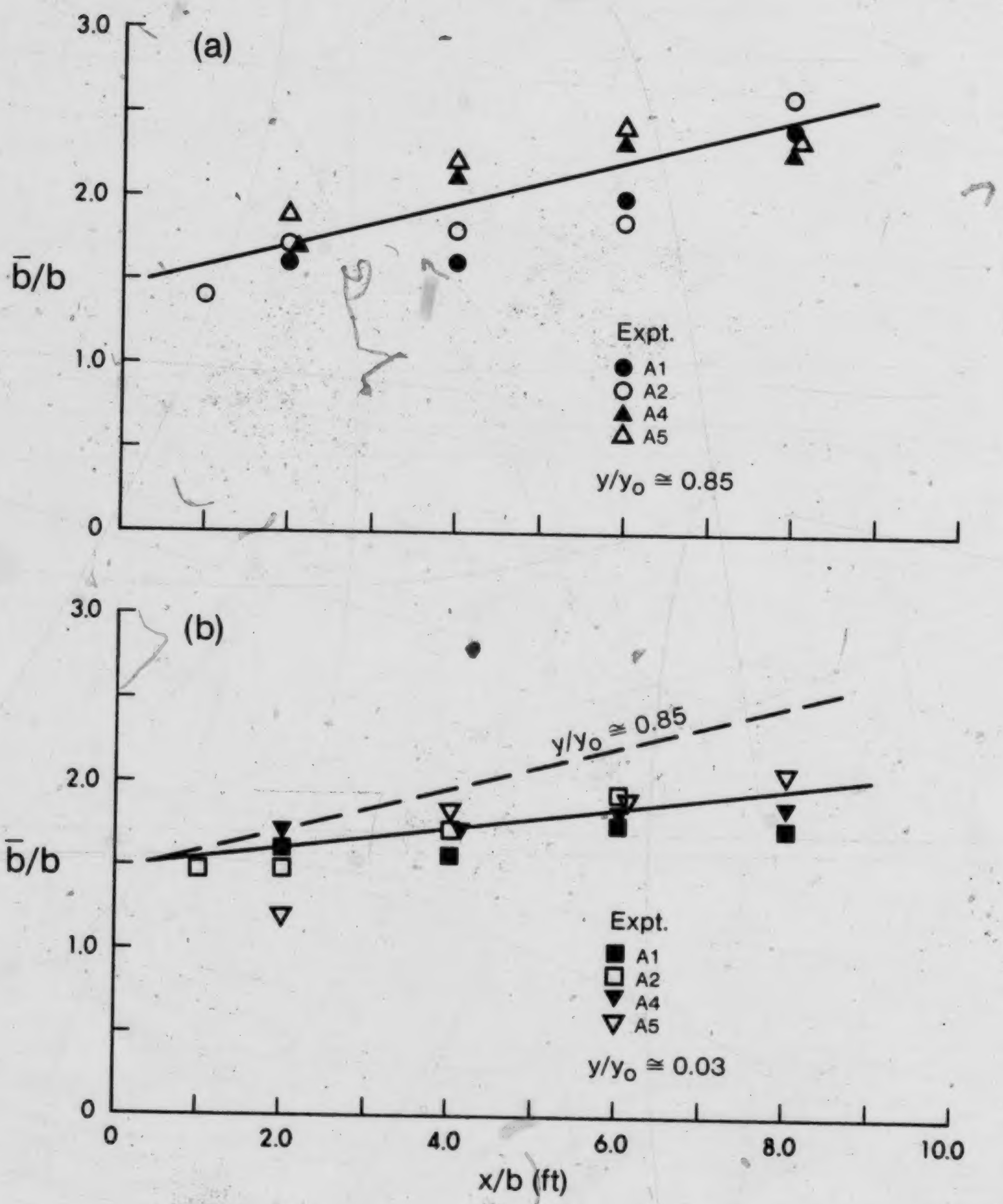

Figure 3.30 Width of the Shear Layer

the approaching flow was equal to 2.06 for the A series and 1.58 for the B series for the upper region. For the lower region, the corresponding values are about 0.75 times the upper region values. To evaluate the variation of U_m/V with b/B, further experiment will have to be made to extend the range of b/B. If u_b is the maximum value of the backward velocity, u_b/U_m was found to be approximately equal to 0.2.

3.2.5 Effect of Groyne Shape

The previous sections have analysed the experimental results for the thin plate groynes in smooth and rough beds. A limited experiment was done to assess the influence of groyne shape (series E experiments).Figure 2.31 shows the typical velocity profiles in the region affected by the presence of the cylindrical groyne. All the characteristics described earlier are evident but the disturbance caused by the cylindrical groyne is not as extensive as for the thin groyne. This can be clearer from Figure 3.5c showing the bed shear stress field. The figure indicates considerable increase of bed shear stress near the nose. The shear amplification ($\tau_o/\tau_{oo} \approx 4.3$) compares favourably with the amplification for the thin groyne of equivalent projection. However, at about $x \geq 2'$ ($x/b \geq 4$) the shear stress has reduced to the undisturbed upstream value for all transverse locations. The length of the eddy zone from the point of separation to the reattachment point was found to be only about 2.5 ft. ($x/b = 5$) compared to x/b of 12 for the thin groynes. These preliminary results indicate the importance of shape particularly for spacing of groynes.

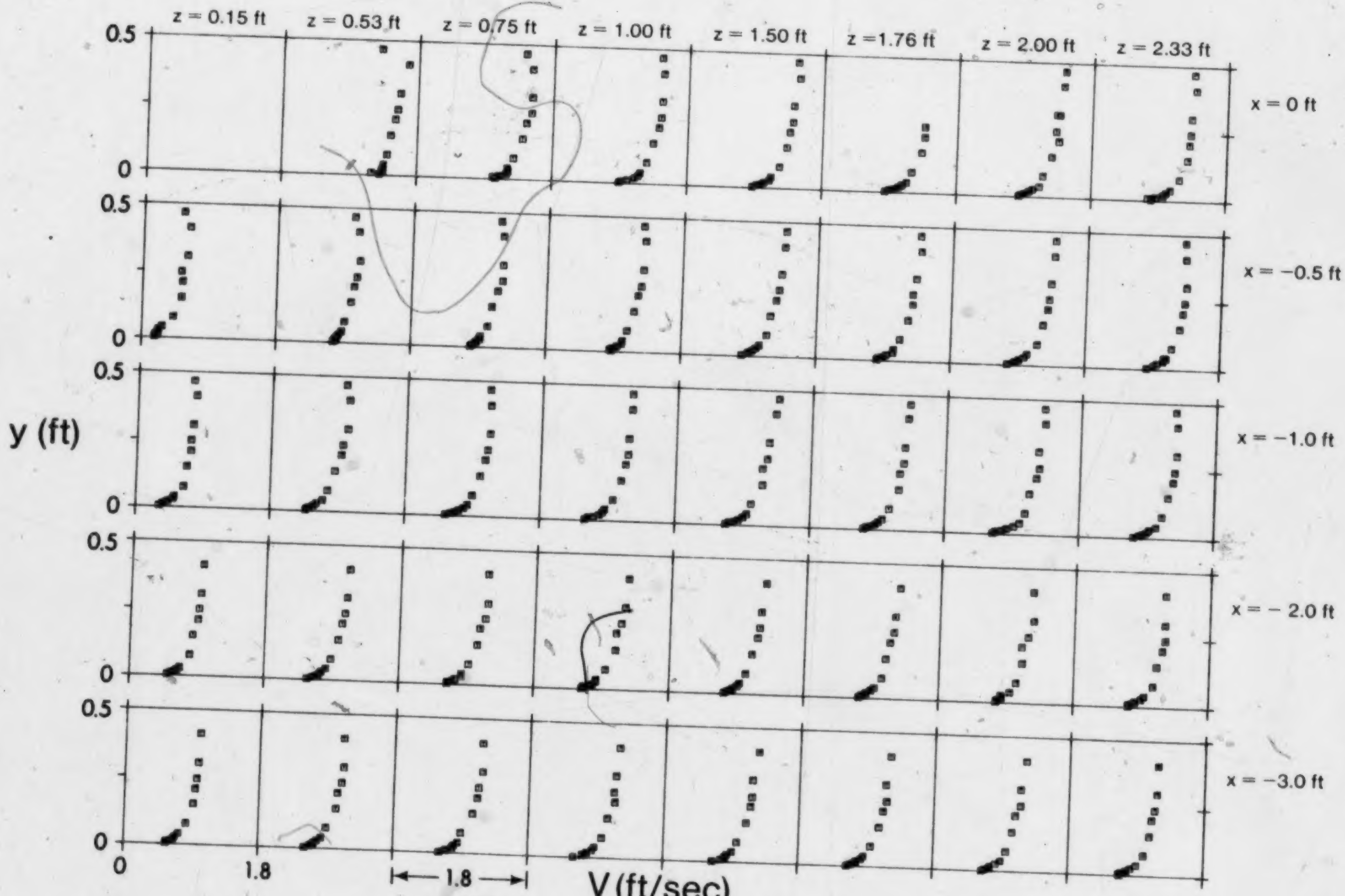

Figure 3.31 (a) Velocity Profile (Expt. E1, Upstream)

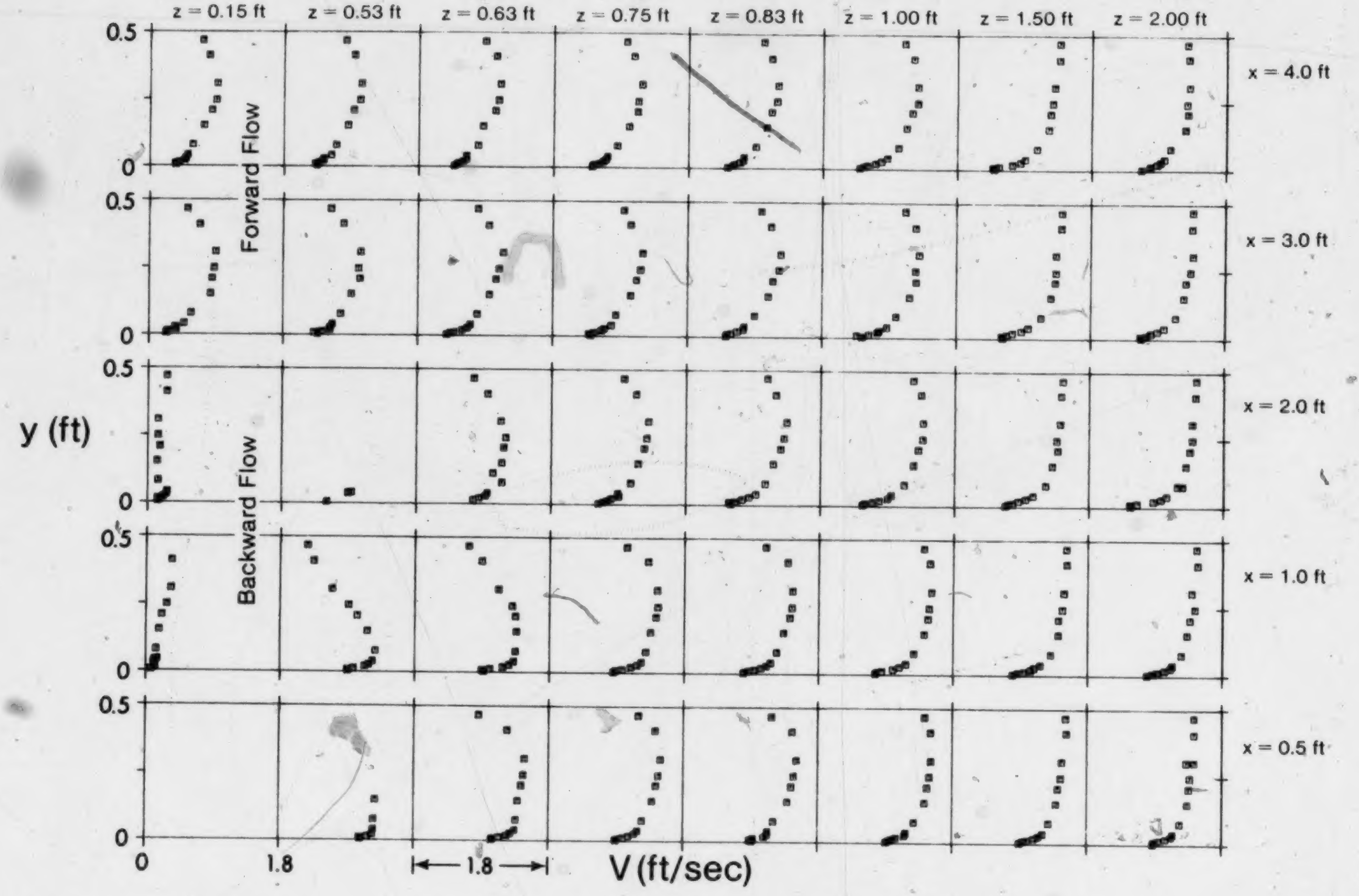

Figure 3.31 (b) Velocity Profiles (Expt. E1, Downstream)

3.3 Energy Consideration

For the thin groyne, the flow separated at its tip and formed vortices behind the structure. Also, near the groyne the water surface dropped suddenly. The vortices and the deformation of the free surface develop to satisfy the momentum and continuity requirements. Consequently, energy is lost and the flow pattern is modified from its upstream condition. A strict analytical solution for the energy loss which is based on the turbulence theory would be difficult. However, Znamenskaya (1967) proposed a method to evaluate energy loss behind dunes. His approach was based on Stoke's formula for energy dissipation rate, ϕ, given as:

$$\phi = 2\mu[(\frac{\partial u}{\partial x})^2 + (\frac{\partial v}{\partial y})^2 + \frac{1}{2}(\frac{\partial u}{\partial z} + \frac{\partial v}{\partial x})^2$$

where u and v are instantaneous velocities. For the different flow layers behind the dune, Znamenskaya computed the energy loss and further developed an empirical relation for the energy loss and the geometry of the dune. Whereas the same approach can be used to compute the energy loss due to the presence of a groyne the data of the present study is not adequate for the analysis.

3.4 Summary

This chapter has shown that when a groyne is placed in a channel, the disturbance caused to the flow is significant unless the projection length or b/B is vanishingly small. The disturbed flow could be analysed by splitting it into a deflected flow region and a shear layer.

In the deflected flow region, the flow could be analysed effectively using the model of a skewed turbulent boundary layer. Johnson's polar plot has been found to be valid. The defect law was also found to be valid. The velocity scale for the defect plot has been determined empirically. The velocity field for the upper layer of the deflect flow has also been analysed empirically.

In the shear layer, the velocity distributions have been found to be similar. The scales for this similarity profile have been evaluated empirically. The bed shear stress in the neighbourhood of the groyne has also been analysed effectively using the similarity technique.

CHAPTER 4

AN EXPLORATORY STUDY OF EROSION NEAR GROYNES

4.1 Introduction and Literature Review

Groynes have been used for many years to guide flows, improve navigation channels and to protect banks from erosion. For each function, scour near the structure is of much concern. A number of studies, mostly of the empirical nature have been conducted to study and develop formulas to predict scour near groynes. Recently, Beckstead (1978) presented an extensive report on the different types of groynes that have been used, and also gave many of the empirical formulas that have been developed to predict the maximum scour. It has been generally found that the maximum scour occurs near the nose of the groyne.

A distinction is made between the scour caused by clear water flow, the so-called 'clear water scour', and scour in sediment transporting flow. The difference according to Laursen (1962) is that at the limit of scour in the clear water case, the boundary shear is reduced to a value that can no longer move the sediment particles (that is the critical tractive force), whereas in the case where sediment is supplied to the scour hole by the stream flow, the boundary shear is reduced to a value such that the capacity to move sediment out of the scour hole is equal to the rate at which sediment enters the scour hole. Also, for a given flow condition and sediment property, maximum depth of scour results when the upstream bed is in a state of incipient motion, that is, when the upstream shear stress is equal to the critical shear stress for that bed material, Gill (1972).

The formulas that have been developed to predict maximum scour could possibly be divided into three groups. In the first group, the maximum depth of scour is expressed as a coefficient times the regime depth for the discharge intensity near the groyne. In the second group, which is based on dimensional analysis and experimental observations in laboratory flumes, the erosion in terms of the depth of approaching flow is expressed as dimensionless functions determined from the variables describing the flow, geometry of the channel including the groyne, the fluid and sediment properties. In the third group, the erosion near the groyne is treated as somewhat similar to that in a long constriction. These methods are discussed in some detail in the next section.

4.2 Regime-Type Formulas

In this group, if $\varepsilon_{m\infty}$ is the maximum depth of scour at the nose of the groyne, Khosla (1936) gave a formula due to Lacey as:

$$(\varepsilon_{m\infty} + y_o) = C[0.90 \frac{q^{2/3}}{f_1^{1/3}}] \qquad (4.1)$$

where f_1 is the Lacey's silt factor (which is a function of the grain size), q is the discharge intensity in the approach channel and C is a coefficient which ranges in value from 1.0 to 3.5 depending on the severity of attack.

Inglis (1949) suggested the formula:

$$(\varepsilon_{m\infty} + y_o) = K\, y_o \qquad (4.2)$$

where y_o is the Lacey regime depth $[0.4(\frac{Q}{f_1})^{1/3}]$ and the multiplying factor K ranges from 1.7 to 3.8.

A revised formula by Blench (1957) is:

$$(\varepsilon_{m\infty} + y_o) = \frac{1.35\ q^{0.74}}{F_b^{1/3}} \qquad (4.3)$$

wherein F_b is the bed factor (again a function of the grain size). Izzard and Bradley (1957) suggested the relation

$$(\varepsilon_{m\infty} + y_o) = 1.40\ q_1^{2/3} \qquad (4.4)$$

where q_1 is the discharge intensity at the groyne. Ahmad (1953) proposed a formula similar in structure to equation 4.4 with the coefficient ranging from 1.2 to 2.25.

4.3 Formulas Based on Dimensional Analysis

Garde, Subramanya and Nambudripad (1961) based on their dimensional argument and experimental observations in laboratory flumes concluded that:

$$\frac{\varepsilon_{m\infty} + y_o}{y_o} = \frac{K}{\alpha} F^n \qquad (4.5)$$

where the coefficient K and exponent n depend upon the drag coefficient of the sediment particles; F is the Froude number. For example, for D=0.29mm, K=4.0 and n=2/3. α is the constriction ratio $\frac{B-b}{b}$. The formula by Mukhamedov et al (1971) conforms in structure to equation 4.5.

Liu, Chang and Skinner (1961) found distinct formulas for clear water scour and scour with continuous sediment transport. For the former the suggested formula is :

$$\frac{\varepsilon_{m\infty}}{y_o} = K\frac{F}{\alpha} \tag{4.6}$$

and with sediment supply, the formula is:

$$\frac{\varepsilon_{m\infty}}{y_o} = C\left(\frac{b}{y_o}\right)^{0.4} F^{1/3} \tag{4.7}$$

The coefficients K and C were 12.5 and 2.15 respectively. Cunha (1971) suggested the equation:

$$\frac{\varepsilon_{m\infty}}{y_o} = K\left(\frac{b}{y_o}\right)^m \left(\frac{h}{y_o}\right)^n \left(\frac{w}{u_*}\right)^r$$

where h is the height of groyne above the bed and w is the fall velocity of sediment particle. The coefficient K and the exponents m, n, r varied with the angle, θ of the groyne to the bank. For example, for $\theta = 90$ degrees, $K = 1.65$, $m = 0.30$, $n = 0.95$ and $r = 0.15$.

4.4 Analogy to Long Constriction

Laursen (1963) and Gill (1972) assumed that the scour near a groyne or abutment could be predicted by treating the flow as similar to that in a long constriction. Expanding on Straub's earlier work (1934), Gill showed that for long constriction:

$$\frac{\varepsilon_{m\infty} + y_o}{y_o} = \left(\frac{B}{B-b}\right)^{6/7} \left[\frac{1}{\left(\frac{B}{B-b}\right)^{1/n}\left\{1 - \frac{\tau_c}{\tau_{oo}}\right\} + \frac{\tau_c}{\tau_{oo}}}\right]^{3/7} \qquad (4.8)$$

The above equation was derived using a generalized bed load equation given as:

$$\frac{q_s}{D\sqrt{gD\Delta\rho/\rho}} = c^*\left(\frac{\tau}{\tau_c} - 1\right)^n \; ; \; \frac{\tau_{oo} - \tau_c}{\tau_{oo}} = o \text{ for } \frac{\tau_1}{\tau_{oo}} \geq 1 \qquad (4.9)$$

where c^* is an empirical constant, n is the exponent and q_s is the sediment discharge per foot width. For scour at groynes, Gill modified equation 4.8 by multiplying the right hand side by an empirical coefficient α_* and with $n = 3$ found out that α_* is only a function of D/y_o. With these, for $\tau_{oo} < \tau_c$

$$\frac{\varepsilon_{moo} + y_o}{y_o} = 8.375 \left(\frac{D}{y_o}\right)^{0.25} \left(\frac{B}{B-b}\right)^{6/7} \left(\frac{\tau_{oo}}{\tau_c}\right)^{3/7} \qquad (4.10)$$

For $\tau_{oo} >> \tau_c$

$$\frac{\varepsilon_{moo} + y_o}{y_o} = 8.375 \left(\frac{D}{y_o}\right)^{0.25} \left(\frac{B}{B-b}\right)^{(6/7)-(3/7)^n} \qquad (4.11)$$

4.5 Aim of Present Work

From the above, it would appear that much effort has been made to determine an empirical formula for predicting the maximum scour near groynes although none of the methods available at present can claim much success under all conditions or beyond the range of data used to obtain the particular formula. The aim of the present study is not to produce another empirical formula to predict equilibrium scour depth but to observe the process of erosion in detail and to understand it in the light of the work presented in Chapter 3. It was also hoped to see whether the development of the erosion process possessed the similarity property which could later be used in the construction of an analytical method.

4.6 Experimental Equipment

The same flume described earlier was used for the scour survey. The flume bed was covered with coarse sand to a depth of nine inches near the test section. The coarse sand extended 15 feet upstream of the groyne and ten feet downstream. A metal plate with a slope of five horizontal to one vertical was attached to the upstream end and a wooden sand trap was placed immediately downstream.

An electronic bed level detector was used to measure the scour. Details of this instrument have been presented by Peterson (1978). The probe maintained a constant distance above the bed and worked on an optical principle. Light was fed through optical fibers and reflected back from the bed into a photo cell which operated a servo-mechanism. The bed detector was connected to an autograph recorder. Scour information was retrieved from the recorder chart. The experiments were conducted for clear water scour only.

The coarse sand used in the scour experiment had a gradation between Number 10 and 20 sieves. The median diameter, D was 1.4 mm. Its specific gravity was about 2.65. The critical shear velocity u_{*c} based on Shield's Function is 0.04 lb/ft^2 and the critical particle Reynolds Number, $(u_{*c}D/\nu)$ is 16. The angle of repose of the sand determined under saturated condition was 33 degrees.

4.7 Experimental Procedure

The sand was placed in the flume and levelled. The desired flume slope was set. The required discharge was established, and the flow depth adjusted until approximately uniform flow was obtained. Flow was then stopped and re-established after installing the groyne and after the bed material around the groyne and other disturbed areas was tamped to its original elevation.

The history of the scour was measured at intervals by running the bed level detector across a section immediately upstream of the groyne nose. The time interval was short at the beginning of the experiment but was increased as the scouring process slowed down. Figure 4-1 shows a typical record of scour history. The bed level detector did not disturb the flow to any noticeable extent, and consequently the scour was measured without stopping the flow. Equilibrium scour was assumed if the depth of scour remained unchanged for about 12 hours. When equilibrium scour was achieved, the scour was measured in the same manner at other cross-sections and used to prepare a contour plot of the scour hole. All the six experiments were performed in clear water flow; the approach shear stress varied from 0.0030 lb/ft^2 to 0.0109 lb/ft^2. Other pertinent flow variables are summarized in Table 4-1.

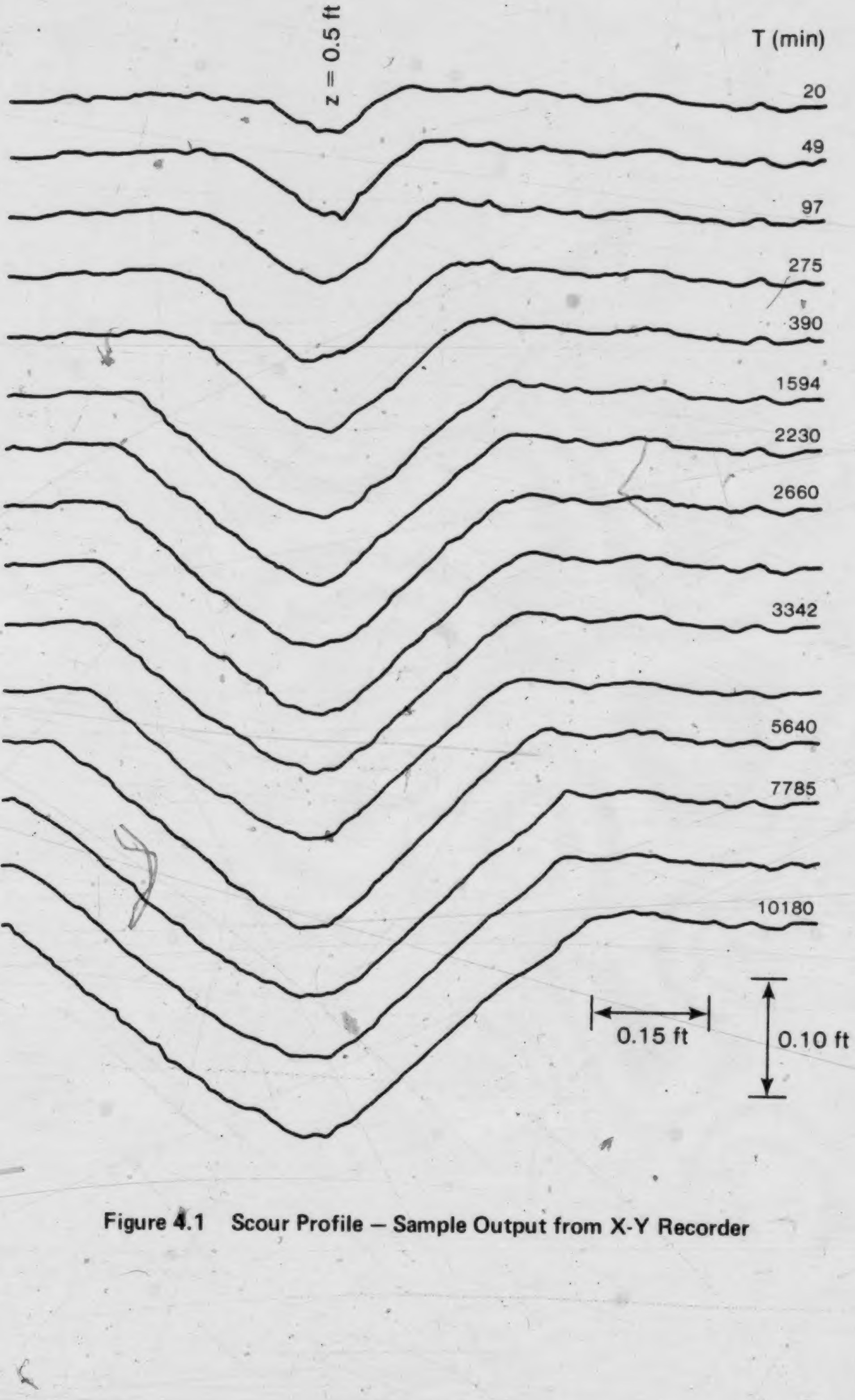

Figure 4.1 Scour Profile – Sample Output from X-Y Recorder

Table 4.1 Summary of Scour Experiments

Run No. / Parameter	1	2	3	4	5	6
Discharge (cfs)	1.025	1.025	1.00	1.025	1.15	0.8
Depth (d ft)	0.505	0.410	0.385	0.350	0.436	0.385
Ave. Velocity (V ft/sec)	0.67	0.81	0.84	1.05	0.83	0.68
Approach Shear Stress (lb/ft^2)	0.0031	0.0047	0.0070	0.0081	0.0069	0.0040
Froude No. $V/\sqrt{gd}$	0.17	0.22	0.24	0.31	0.22	0.19

4.8 Experimental Results

The velocity profiles in the approaching flows are shown in Figure 4.2. The results indicate that the flow is fully developed and is proportional to log y. The profiles are plotted in dimensionless form in Figure 4-3 which shows that the profiles satisfy the Karman-Prandtl logarithmic law. For experiments 3, 5 and 6, the data agree reasonably well with the equation:

$$\frac{u}{u_*} = 5.75 \log \frac{yu_*}{\nu} - 2.11 \tag{4.12}$$

and indicate that the flows were rough turbulent whereas for the other experiments the points are located somewhat higher.

The experiments showed that the maximum scour always occurred near the nose of the groyne. If ε_m is the maximum depth of erosion or scour below the original bed level, the variation of ε_m with time t is shown in Figure 4-4. The figure shows that for a certain part of erosion period, ε_m increases linearly with log t and eventually ε_m approached its equilibrium value of $\varepsilon_{m\infty}$ which will be referred to as the equilibrium scour. This equilibrium scour was achieved, for different experiments, from 8 to 24 days.

The time sequence for the development of the scour hole is shown as contour-type plots in Figure 4-5 (a to d) for experiment 6, while Figure 4-5(e) shows a typical cross section evolution immediately upstream of the groyne nose for the same experiment. The contour plans of the scour hole at the equilibrium stage are shown in Figure 4-6 for all the six experiments. Figure 4-7 (a and b) show the profiles of the scour holes for the equilibrium stage, at the groyne nose, i.e. $\varepsilon_\infty(z)$ and

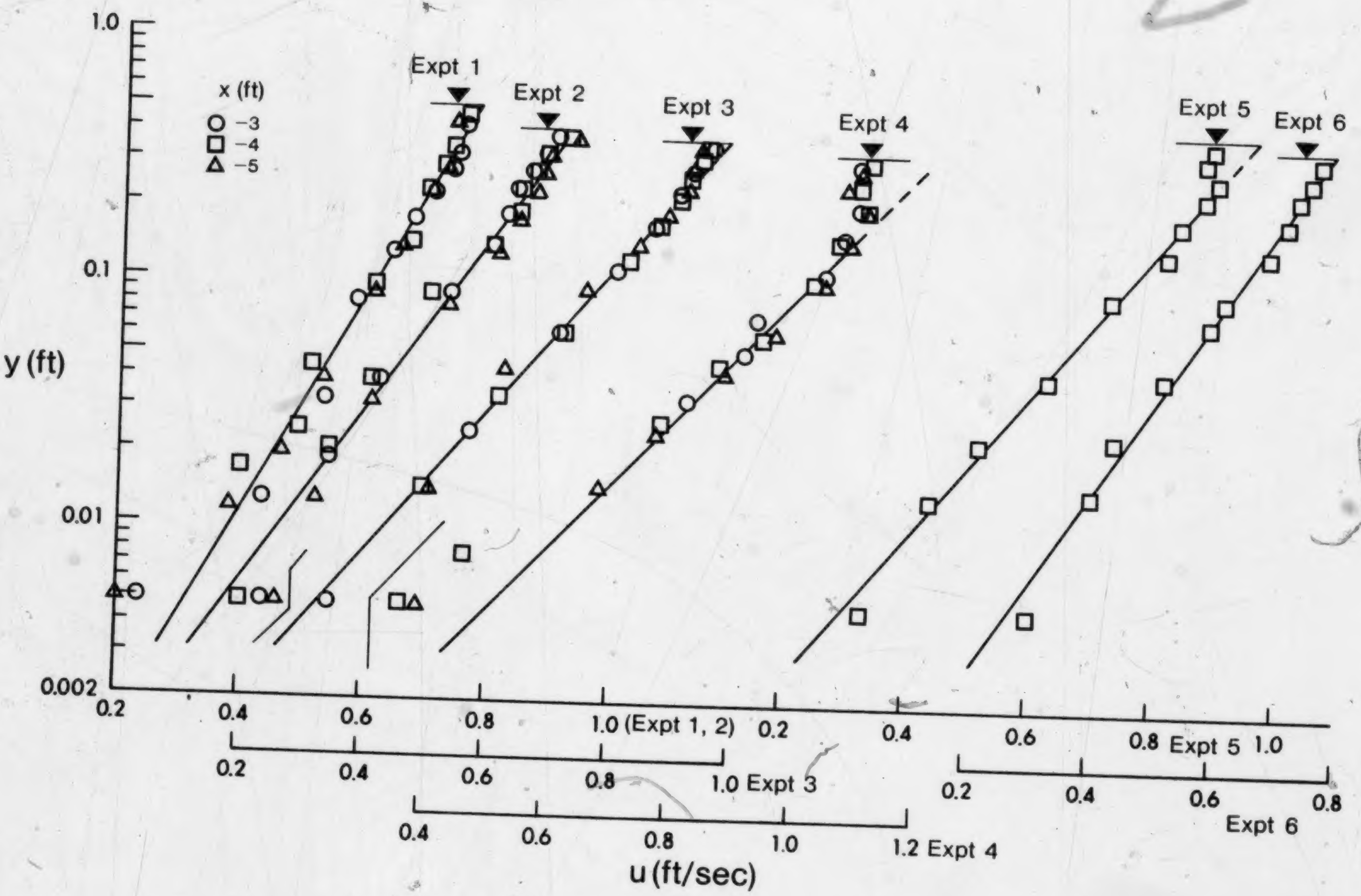

Figure 4.2 Velocity Profiles for the Approach Flow

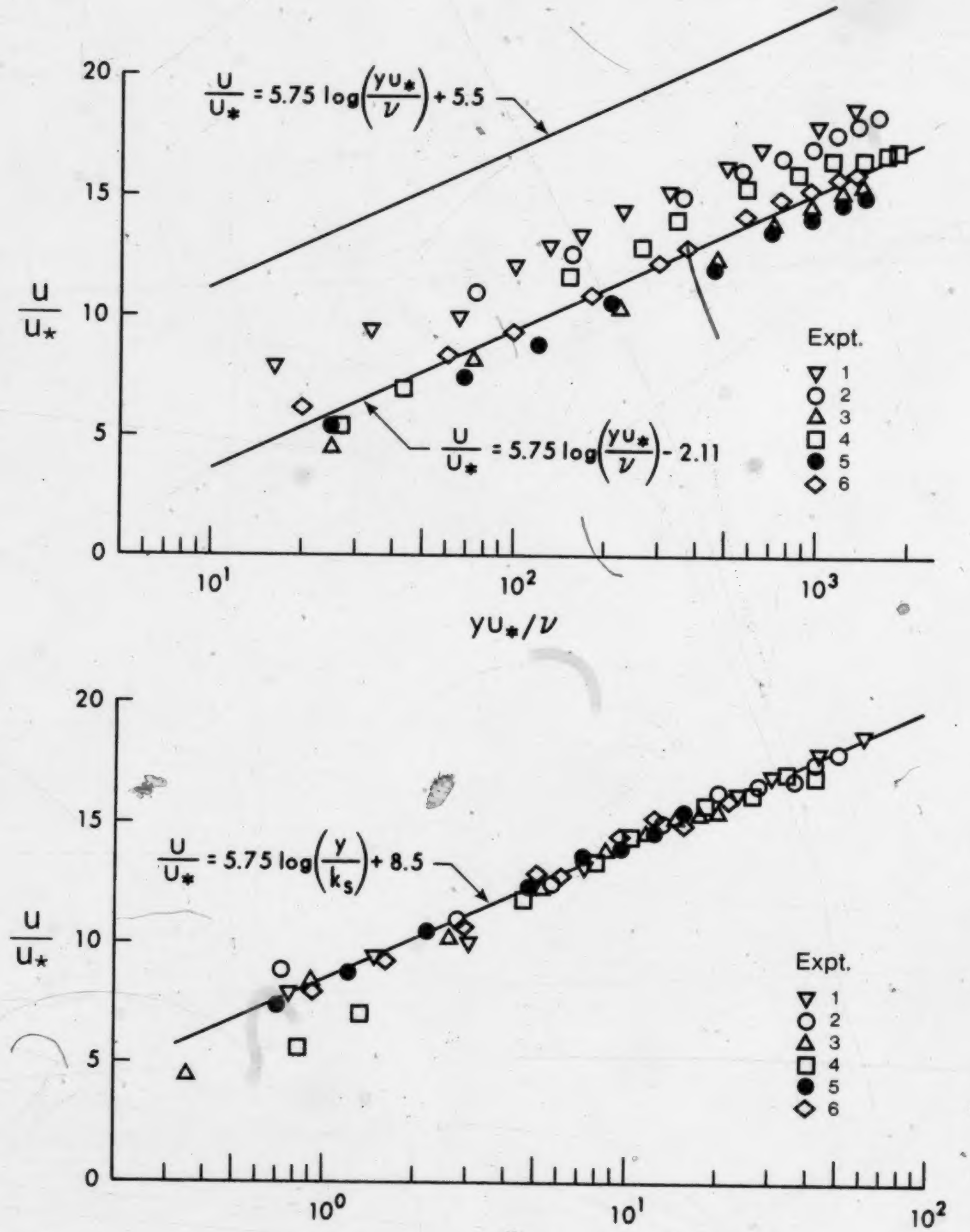

Figure 4.3 Dimensionless Velocity Profiles

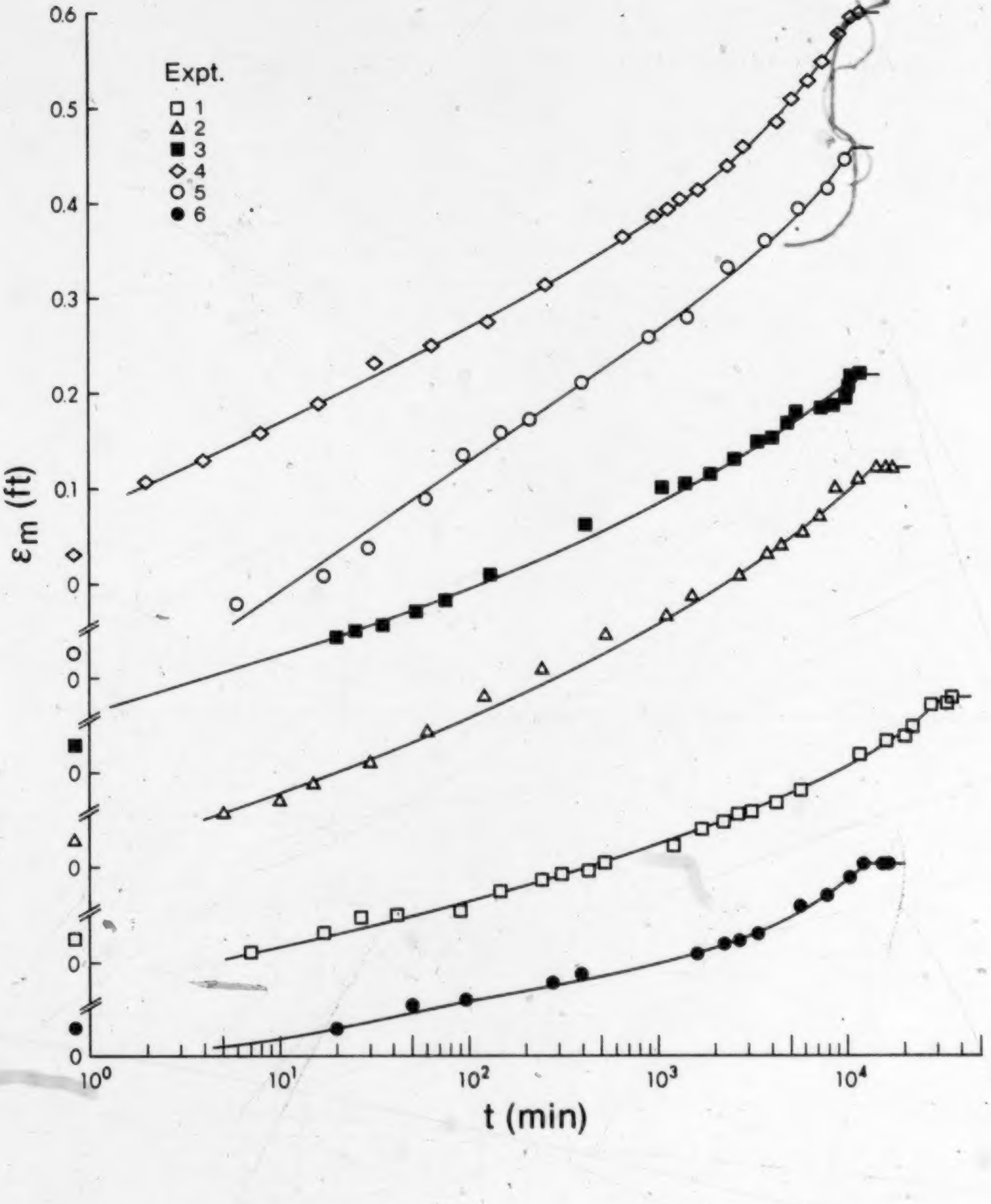

Figure 4.4 Variation of Scour Depth with Time

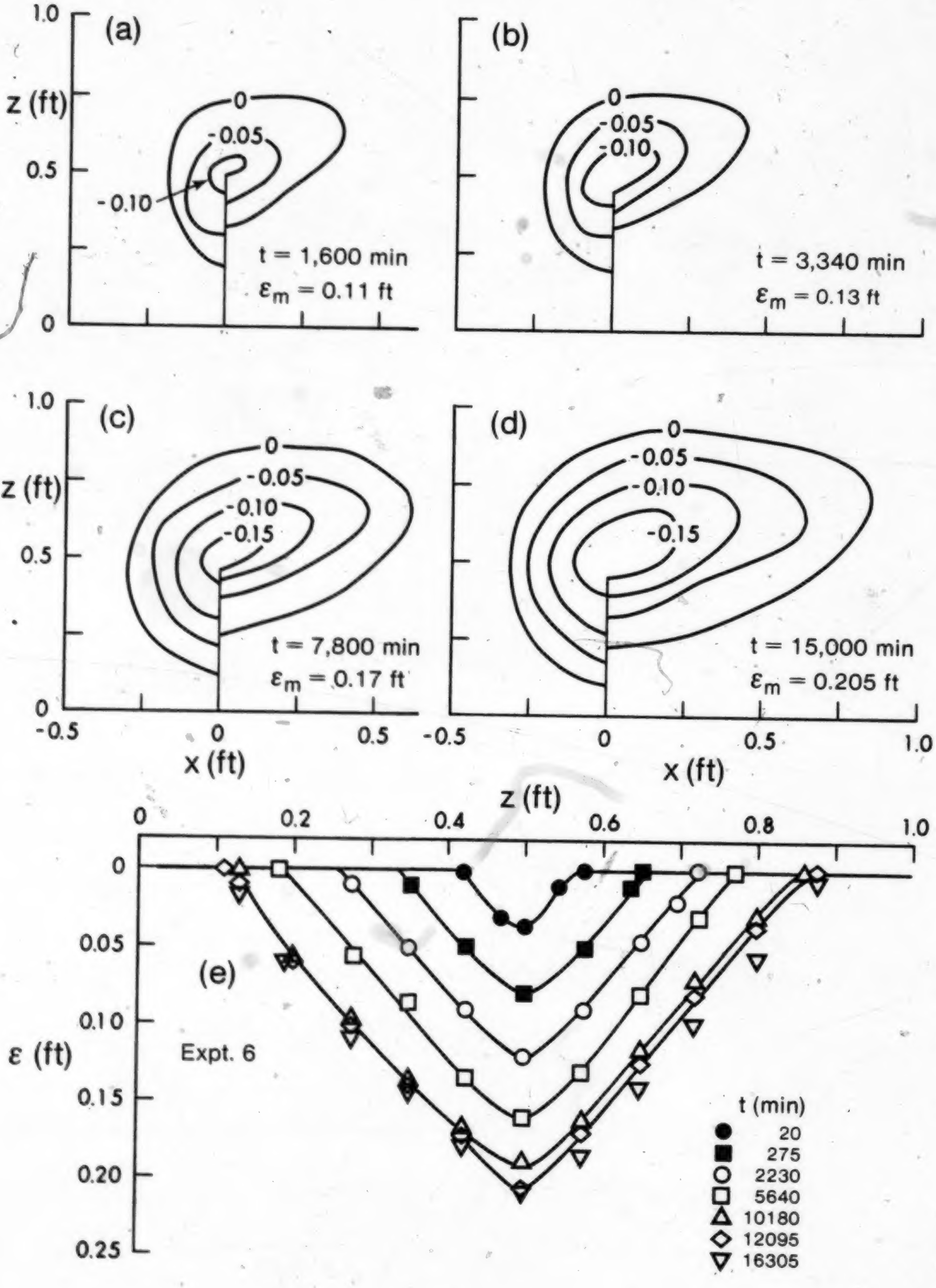

Figure 4.5 Time Sequence of Scour Development (Expt. 6)

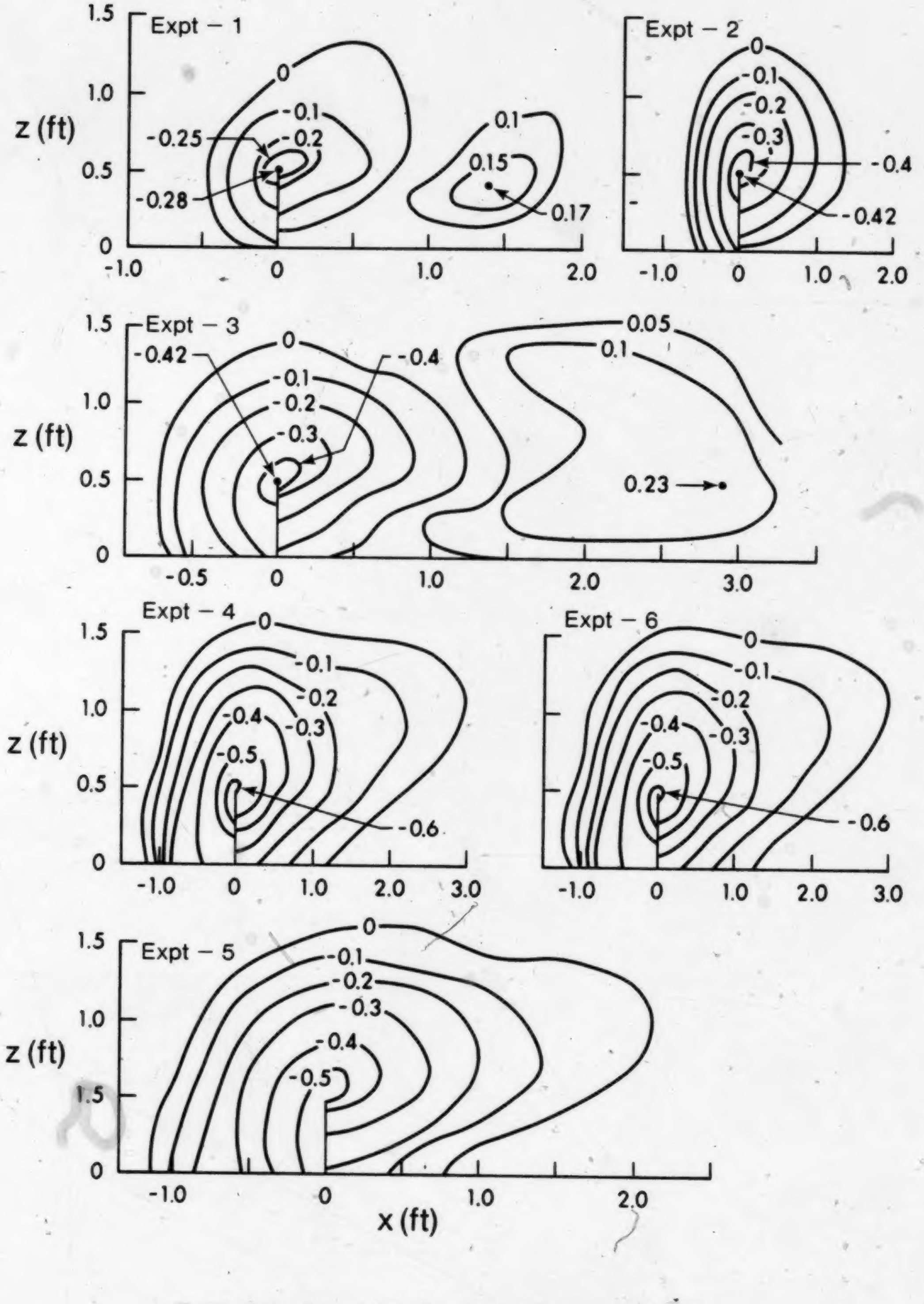

Figure 4.6 Scour Hole Contour at Equilibrium State

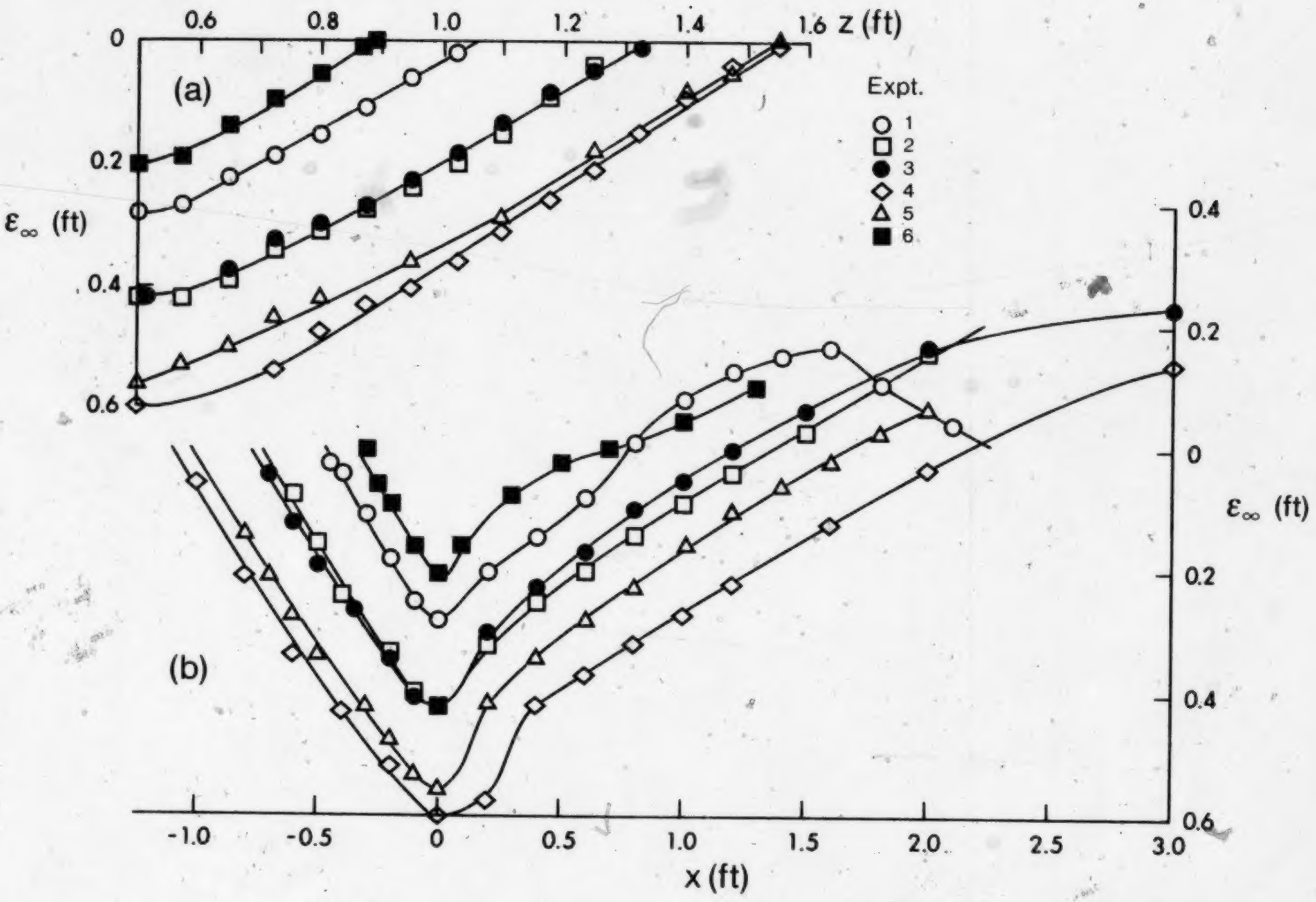

Figure 4.7 Profiles of Scour Hole at Equilibrium State

$\epsilon_\infty(x, z=b)$ respectively, for all the six experiments.

4.9 Visual Observation of Scour Process

The description following was observed in clear water scour. Once the experiment was started, the bed around the groyne nose began to scour. This is the same region where the maximum shear stress was measured in the rigid bed. For the flow regime tested (Froude number from 0.17 to 0.31), the bed material was transported or carried out of the scouring area mainly by rolling motion; upward movement of bed material was not very strong. In the initial stages of the scour process, the eroded material piled up in the downstream lip of the hole and was eventually pushed further upstream as the scour progressed. Thus some bed zones shifted from depositional to erosional, reflecting the changes of the flow pattern and shear stress field from their initial conditions. In the early period of the scour process, the depth increased rapidly with time and the side slopes appeared to stand at the angle of repose for the bed material. Further scour around the toe caused local steepening of the slope in that region and some material was observed to slump into the hole and subsequently carried away by the flow. By this process, the hole enlarged even to the flow region where the shear stress was not considered competent to cause scour. Measurements in a rigid bed show that the shear stresses near the upstream face of the groyne are small compared to the mean approach shear stress. Therefore, some distance upstream of the groyne, the bed would not be expected to erode, but the process of undermining followed by slumping as described above explains why scour extended to this region.

4.10 Analysis of Experimental Results

4.10.1 Variation of ε_m with Time

Considering firstly the growth of ε_m with time, Figure 4.4 showed that for a large part of the scouring process, $\varepsilon_m \propto \log t$. Studies on erosion by jets (Rajaratnam and Berry, 1977) have indicated that the erosion process is similar in time if expressed in proper dimensionless forms. This is done in Figure 4.8 wherein $\varepsilon_m/\varepsilon_{m\infty}$ is plotted against t/t_* where $t_* = t$ when $\varepsilon_m/\varepsilon_{m\infty} = 0.75$. Figure 4.8 indicates that as an approximation, erosion process with time could be considered to be similar. This curve clearly indicates three phases in the erosion process, a linear log phase (i.e. phase 2), pre-log phase, and end process (phase 3). In the case of erosion by jets, the curve is convex upwards near the end state whereas in the present work on groynes, it is seen to be concave upwards near the end state.

A preliminary attempt to predict the time scale, t_* is made using dimensional arguments whereby it is postulated that:

$$t_* = f_1(u_{*o}\ \rho,\ D,\ g\Delta\rho,\ B,\ b,\ \nu) \qquad (4.13)$$

where u_{*o} is the shear velocity, $\sqrt{\frac{\tau_{oo}}{\rho}}$ of the approach flow. Using the Pi-theorem, equation 4.13 could be reduced to:

$$\frac{t_* u_{*o}}{D} = f_2\left(\alpha = \frac{B-b}{B},\ \frac{u_{*o} D}{\nu},\ \frac{u_{*o}}{\sqrt{gD\,\frac{\Delta\rho}{\rho}}},\ \frac{B}{D}\right) \qquad (4.14)$$

or

$$\frac{u_{*o} t_*}{D} = f_3\left(\alpha,\ \frac{u_{*o}}{\sqrt{gD}}\right) \qquad (4.15)$$

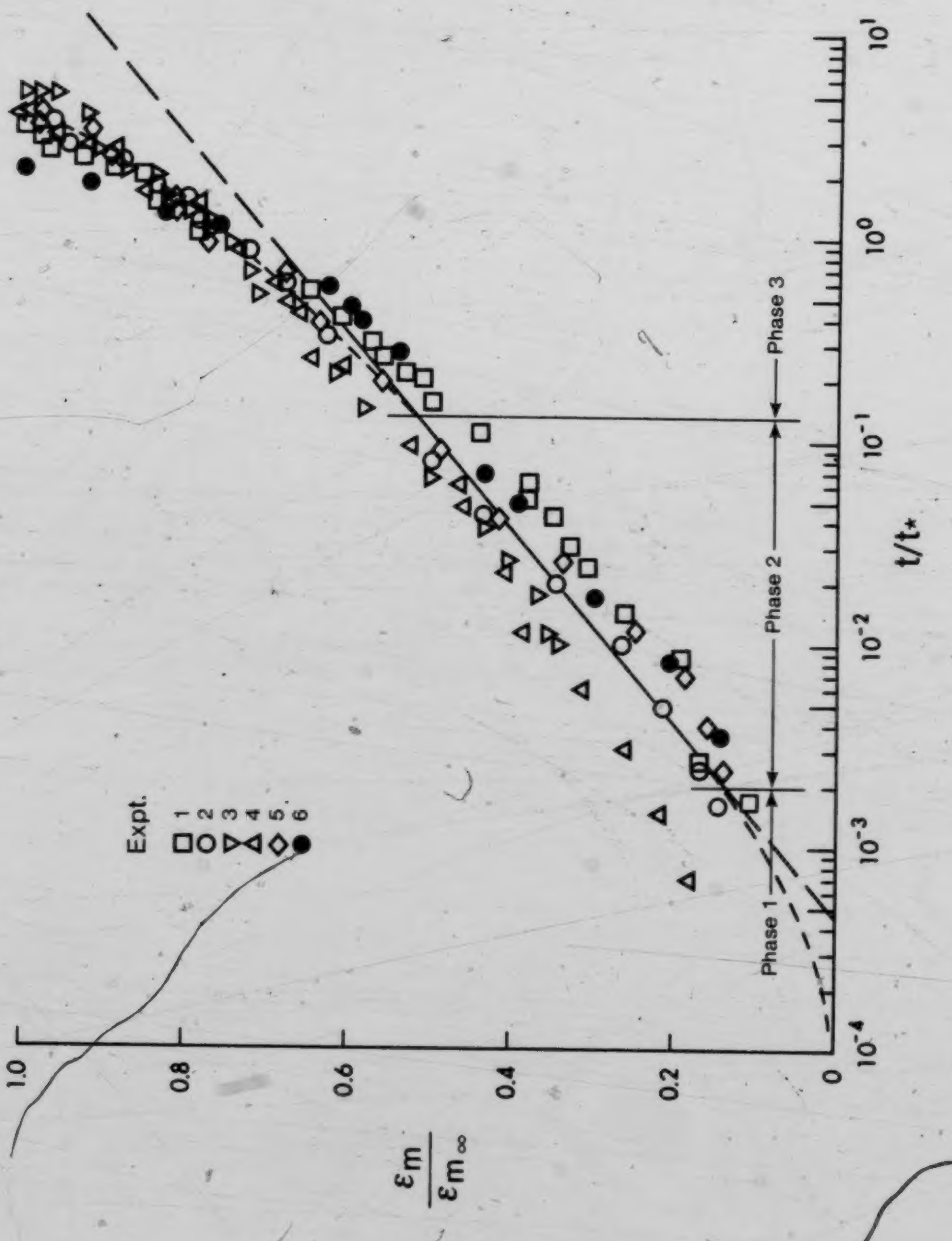

Figure 4.8 Similarity of Scour Depth Development

for a given $\frac{\Delta\rho}{\rho}$ and $\frac{u_{*o}D}{\nu}$ greater than the limiting value for the turbulent flow. Figure 4.9 shows the plot of $\frac{u_{*o}t_*}{D}$ against $\frac{\sqrt{gD}}{u_{*o}}$ for the six experiments. The dimensionless time scale would appear to be a function of $\frac{\sqrt{gD}}{u_{*o}}$ but further experimental observations are needed to establish the functional form more precisely. The scour depth scale $\varepsilon_{m\infty}$ for Figure 4.8 is considered in section 4.10.3.

4.10.2 Cross-section and Geometry of the Scour Hole

Figure 4.5 showed the contour and cross-section of the scour hole from transitional state to equilibrium or end state. It can be seen that the scour area increased with time but had an essentially consistent pattern during its growth to the final equilibrium state. The scour holes are slightly skewed to the downstream of the groyne, in conformity with the shear stress pattern.

At the equilibrium state, the cross-sectional profiles, $\varepsilon_\infty(z)$ make an average angle of 32 degrees, with the horizontal plane approximately equal to the angle of repose for the bed material, which is about 33 degrees. If $\overline{z}'$ is the width of the scour hole from the groyne nose, the ratio $\overline{z}'/\varepsilon_{m\infty}$ was found to be approximately 1.9. For $z' = z-b$, Figure 4.10(a) shows the plot of $[\varepsilon/\varepsilon_m]_\infty$ versus $z'/\overline{z}'$. It is seen that all these transverse profiles are similar.

The longitudinal profiles of the scour hole $\varepsilon_\infty(x)$ at the groyne nose ($z = 0.5$) were shown in Figure 4.7b. These profiles are analysed for geometrical similarity in two parts. For the upstream part ($x < o$), if $\overline{x}'$ is the upstream extent of scour, Figure 4.11(a) shows the plot of $[\varepsilon/\varepsilon_m]_\infty$ versus $x'/\overline{x}'$, where x' is the distance measured from the groyne.

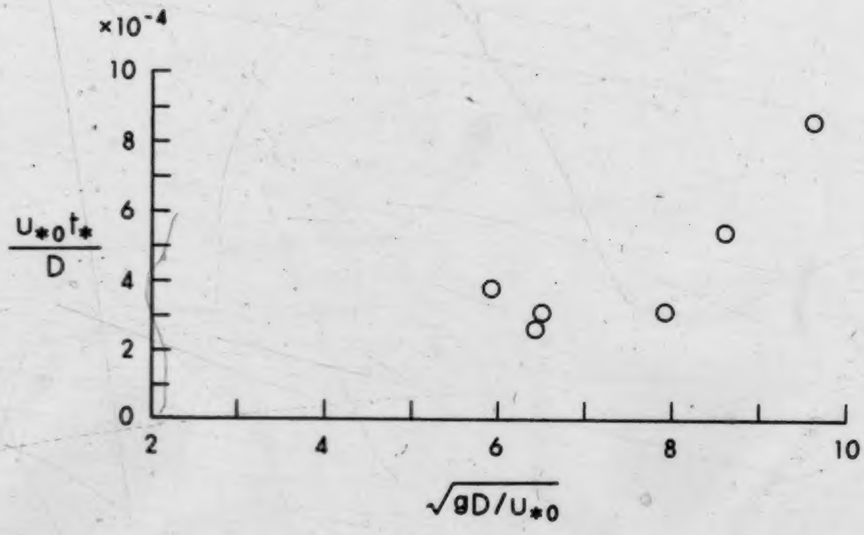

Figure 4.9 Time Scale for Scour Depth Development

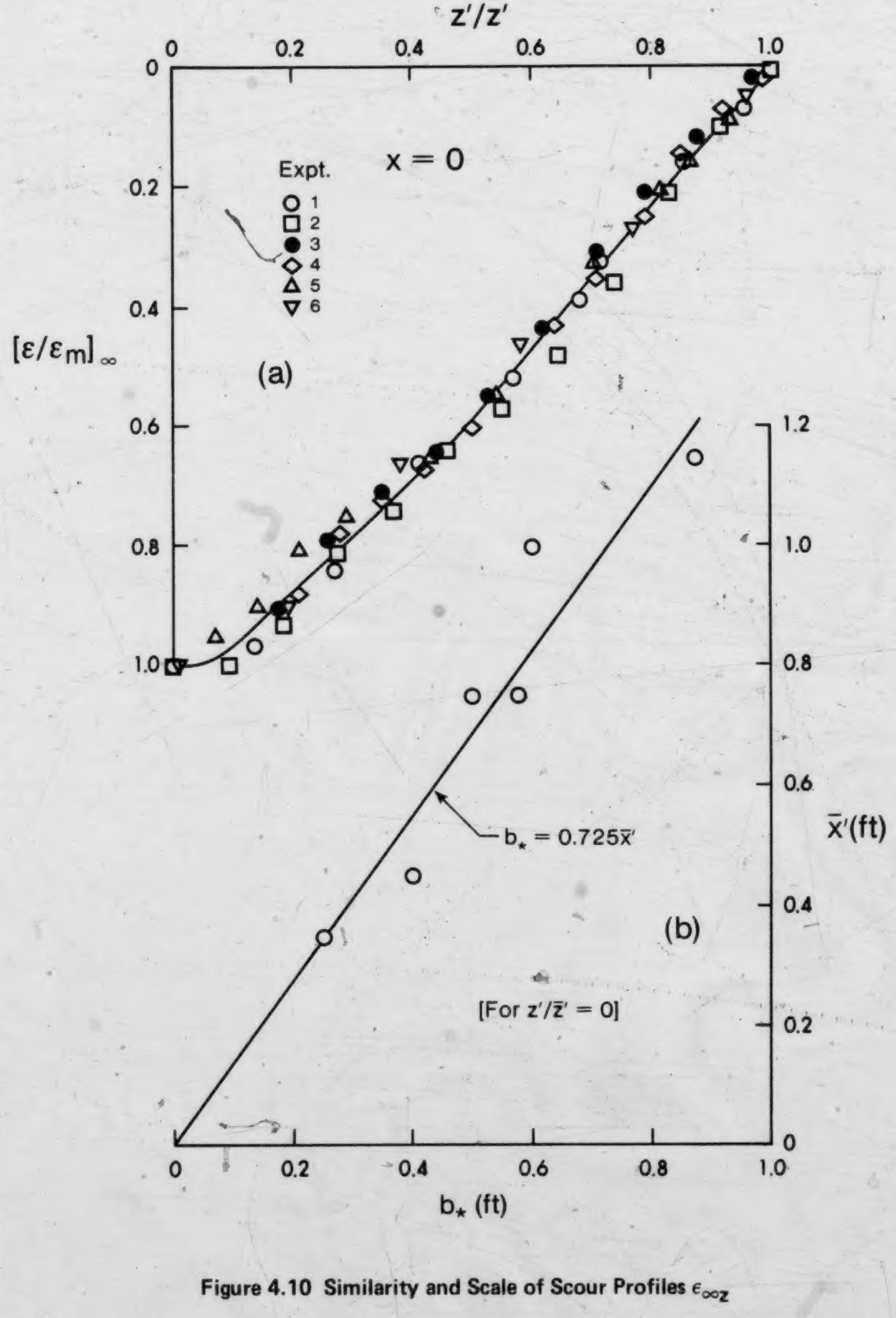

Figure 4.10 Similarity and Scale of Scour Profiles $\epsilon_{\infty z}$

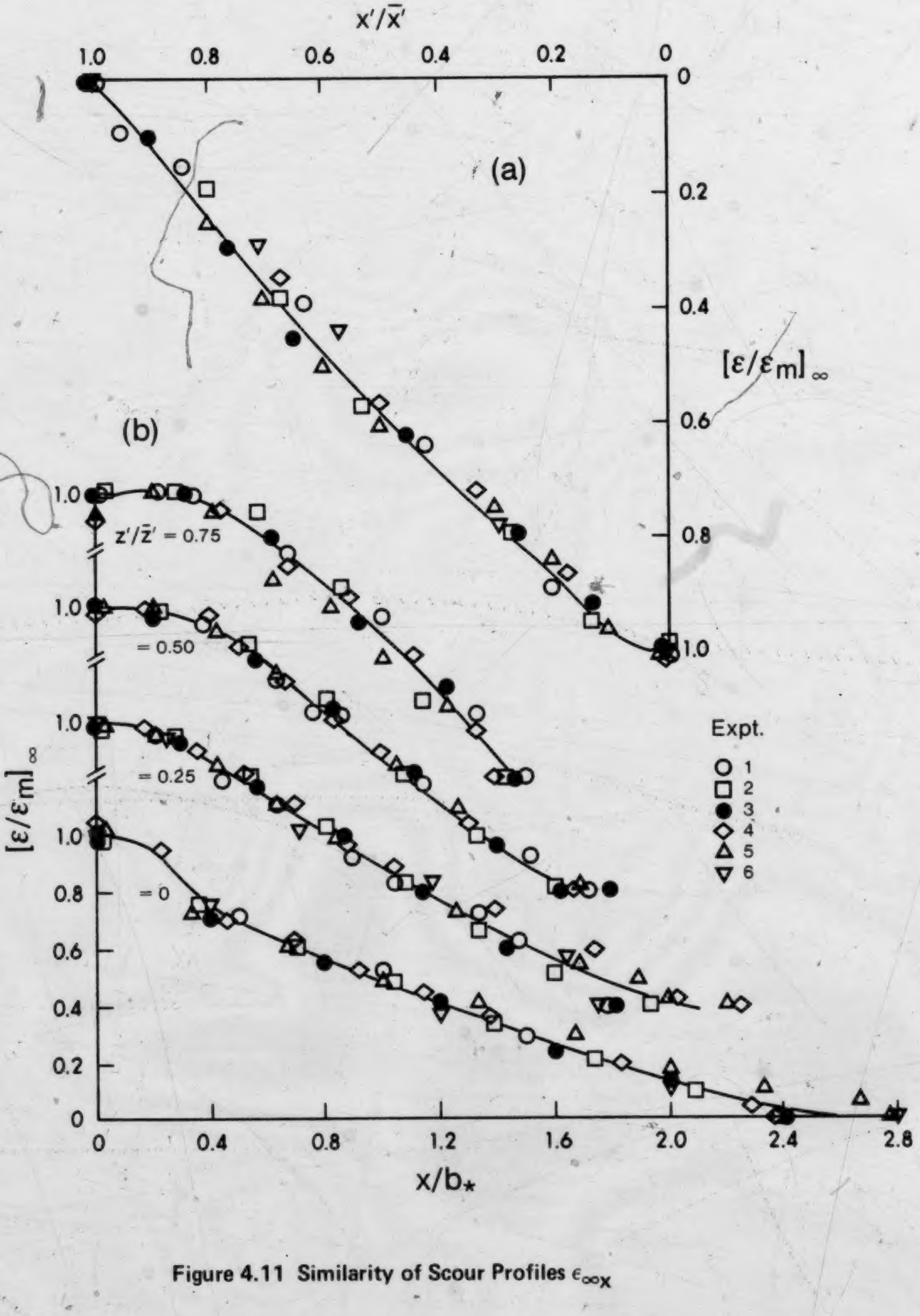

Figure 4.11 Similarity of Scour Profiles $\epsilon_{\infty x}$

Again, the profiles are similar (see Figure 4.11a) and $\overline{x}'/\varepsilon_{m\infty} \approx 1.9$. For the downstream part, the plot of $[\varepsilon/\varepsilon]_\infty$ against x/b_* (where b_* is the value of x where $\varepsilon_\infty = 1/2\ \varepsilon_{\infty m}$) is shown in Figure 4.11(b). The figure indicates that for any longitudinal section, the scour hole profile is similar. From Figure 4.10(b), $b_* = 0.725\ \overline{x}'$. Using the figures discussed in this section, and the empirically derived length scales, it is possible to establish the aerial extent of scour.

4.10.3 The Equilibrium Depth of Erosion $\varepsilon_{m\infty}$

From our knowledge of sediment transport, and of the erosion process near a groyne, we could write:

$$\varepsilon_{m\infty} = f_1[u_{*o}, \rho, D, g\Delta\rho, B, b, \nu] \tag{4.16}$$

Using the Pi-theorem, equation 4.16 could be reduced to:

$$\frac{u_{*o}}{\sqrt{g\varepsilon_m \frac{\Delta\rho}{\rho}}} = f_2[\alpha = \frac{B-b}{B}, \frac{u_{*o}D}{\nu}, \frac{u_{*o}}{\sqrt{gD \frac{\Delta\rho}{\rho}}}, \frac{B}{D}] \tag{4.17}$$

If the flow is in the rough turbulent stage, $\frac{u_{*o}D}{\nu}$ will be of minor importance; B/D is unlikely to be important when $\frac{B}{D}$ is very large. For a given value of $\frac{\Delta\rho}{\rho}$, equation 4.17 could be reduced to:

$$\frac{u_{*o}}{\sqrt{g\varepsilon_m}} = f_3[\alpha, \frac{u_{*o}}{\sqrt{gD}}] \tag{4.18}$$

Since $\tau_c \propto D$, the dimensionless group $\frac{u_{*o}}{\sqrt{gD}}$ could be shown to be proportional to τ_{oo}/τ_c in the rough turbulent regime.

Considering first, the cases where $\tau_{oo} < \tau_c$, i.e. when there is no noticeable transport of bed material from upstream of the groyne, the present observations as well as those of Gill (1972) and Cunha (1971) are shown plotted in Figure 4.12(a). It is interesting to note that in the range of $u_{*o}/\sqrt{gD}$ from about four to ten, $u_{*o}/\sqrt{g\varepsilon_{m\infty}}$ is independent of $u_{*o}/\sqrt{gD}$ and depends mainly on α. For the present work, with $\alpha = 0.83$, $u_{*o}/\sqrt{g\varepsilon_{m\infty}} \simeq 0.015$. For the data of Cunha and Gill, with α being equal to 0.85 and to 0.87 respectively, $u_{*o}/\sqrt{g\varepsilon_{m\infty}} \simeq 0.0185$, which is about 20% larger than 0.015.

Considering next flows with $\tau_{oo} > \tau_c$, i.e. where there is general bed material transport from upstream, Figure 4.12(b) shows a plot of the readily available data with $u_{*o}/\sqrt{g\varepsilon_m}$ against τ_c/τ_{oo} From Figure 4.12(b) it is seen that for $\tau_c/\tau_{oo} \gtrsim 0.25$, one mean curve could be drawn through the data and this curve appears to approach asymptotically the $u_{*o}/\sqrt{g\varepsilon_m}$ value for no bed transport from Figure 4.12(a). For $\tau_c/\tau_{oo} \lesssim 0.25$, there is considerable scatter and a preliminary investigation using the concept of stream power revealed a diversity of upstream bed forms (from ripple to anti-dune) for the various experiments. Further research is needed to test the credibility of the scheme presented here.

4.11 Summary

The analysis and visual observation presented in this chapter showed that when a groyne is placed in a loose boundary channel, the flow could be modified to cause erosion near the structure. The maximum depth of scour occurs near the nose of the groyne. When the flow carries no bed load, the maximum depth of scour is found to depend on the

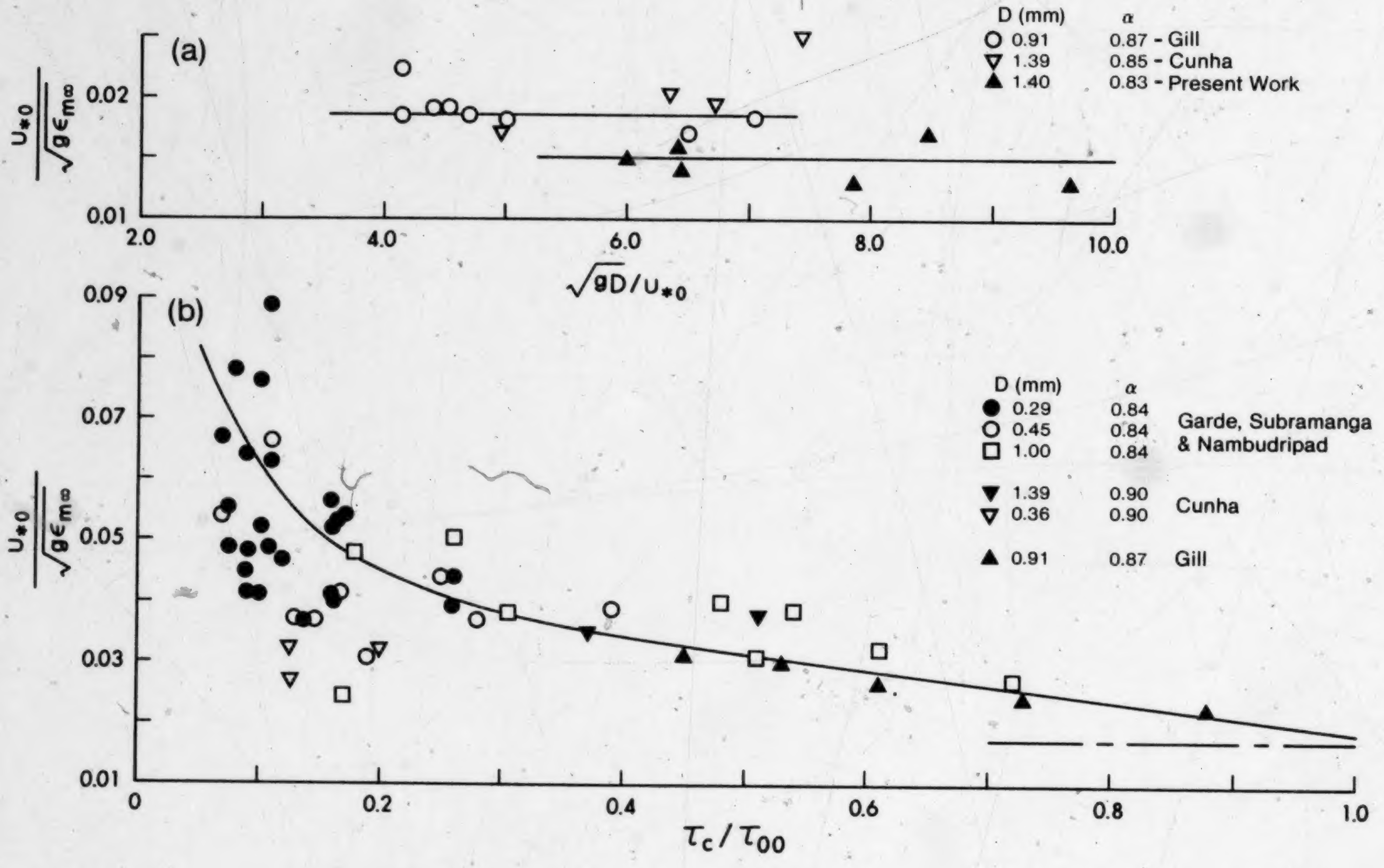

Figure 4.12 Criterion for Equilibrium Scour Depth

constriction ratio. The development of scour depth with time could be approximately considered to be similar. In the equilibrium state, the scour profiles are similar along any equivalent longitudinal or transverse sections when plotted with proper scales.

CHAPTER 5

CONCLUSIONS AND RECOMMENDATIONS

5.1 Summary

Groynes are widely used to protect river banks from erosion and to guide the flow in a defined channel. To advance our competence in groyne design, and to predict the impact on river systems due to the presence of groynes, we need an understanding of the nature and structure of the turbulent flow near groynes. In this work, which is exploratory and experimental in nature, the time-averaged turbulent flow near a thin plate groyne is studied in a rectangular fixed bed channel. This is followed by a preliminary study of erosion process near the groyne with the aim to understand the process of erosion in the light of the flow structure.

5.2 Conclusion

This study has shown that when a groyne is placed in a channel it causes a significant disturbance to the flow for a shorter distance upstream and for a longer distance downstream. In the disturbed and highly skewed flow regions, the conventional Pitot and Preston tubes are not appropriate for measuring the velocity and bed shear stress fields. The yaw probe was successfully used to measure both the flow velocity and the bed shear stress.

The disturbed flow was analysed by splitting it into a deflected flow region and a shear layer. For the deflected flow region, the skewed turbulent boundary layer model by Johnson was found to be valid for the kind of flow studied here. The defect-velocity vectors normalized on the velocity defect vector at the apex of the Johnson's polar plot conformed to the scheme suggested by Hornung and Joubert and the velocity scale for the defect plot was determined empirically. Also, empirical curves describing the velocity field for the upper flow layer in the deflected flow region were established.

The flow separating from the tip of the groyne was found to reattach itself to the flume wall at an approximate distance of 12 times the groyne length. Flow disturbance extended to about two times the groyne length upstream. The downstream extent of disturbance was not determined but Francis and Pattanaik suggested that normal channel flow is re-established at about 40 times the projection length downstream.

As the flow goes around the groyne, the boundary layer thickness is suppressed to a very thin layer near the nose due to extreme turbulence and the velocity distribution become almost uniform. There is also a lowering of the water surface at the nose of, and behind the groyne.

In the shear layer, the velocity distributions for any horizontal plane were found to be similar. The scales for this similarity profile were evaluated empirically.

The maximum bed shear stress occurred near the groyne nose. The shear stress amplification τ_{om}/τ_{oo} depended on the opening ratio $\frac{B-b}{B}$. For b/B = 0.17 τ_{om}/τ_{oo} was about 5, and for the three inch groyne b/B = 0.08, the same ratio was about 3. However, all the bed shear stress measurements in the neighbourhood of the groyne were analysed effectively using the similarity technique.

There were no discernible effects in the observed flow characteristics due to roughness. For a cylindrically shaped groyne, the disturbed flow region was remarkably smaller compared to the region affected by the thin plate model.

For the constriction ratios studied here, the maximum depth of scour occurred at the location of the maximum shear stress (i.e. at the groyne nose). Erosion progressed to a region of low shear stress, upstream of the groyne, by the process of undermining followed by slumping of the scour hole surface. Das (1972) found that in a constricted channel, maximum bed scour occurs at the channel centre when the constriction ratio is greater than about 0.4. In his study, both the maximum bed scour and the maximum velocity were located at the section of the vena-contracta. These phenomena may be associated with the jet concept.

The curve describing the history of scour indicated three phases in the erosion process. These were a linear log phase (ε_m α proportional to log t), a prelog phase and an end process. The entire erosion process with time was found to be similar. The geometry of the scour hole was consistent for all phases.

The equilibrium depth of scour in clear water flow was found to depend mainly on the constriction ratio, α. For a given α it would appear that $u_*/\sqrt{g\varepsilon_{m\infty}}$ is a constant. This relationship has been deduced from very limited data and must be used with reasonable judgement.

5.3 Recommendations

There is immense scope to advance on the work presented here. The present study considered only two constriction ratios ($b/B = 0.17$

and 0.08). Further experiments will have to be made to cover a wider range of b/B so as to determine the lower limit for which the effect of constriction on both flow and scour would be minimal and the upper limit for which a general bed scour could become significant.

The simple groyne geometry studied here is only a necessary first step to understand some nature of the flow and scour around the obstruction. In practice, groynes have reasonable thickness, and various nose shapes; they are often inclined at certain angle to the approach flow and constructed as a group. Further experiments of the nature presented here are required for these practical cases. Using these results, the equations of motion could possibly be simplified for the different flow regions and different flow layers and then semi-empirical prediction methods could be developed.

To advance our knowledge of the erosion process, experimental work on mapping the velocity and bed shear stress fields in the scour hole for different stages of its development, should be carried out.

LIST OF REFERENCES

1. Ahmad, M., "Experiments on Design and Behaviour of Spur Dikes," Proceedings, Minnesota International Hydraulic Convention, University of Minnesota, Minneapolis, Minnesota, 1953.

2. Beckstead, G., "Groyne Design," M.Sc. Thesis, Colorado State University, Fort Collins, Colorado, July 1978.

3. Blench, T., "Regime Behaviour of Canals and Rivers," Butterworths Scientific Publications, London, 1957.

4. Cunha, L., "Local Scour of Obstacles Protruding From River Banks," Ph.D. Thesis, University of Lisbon, Portugal, 1971.

4a. Das, B., "End-Dump Closure of Alluvial Channels," Ph.D. Thesis, University of Alberta, Edmonton, 1972.

5. Einstein, H. and El-Samni, A., "Hydrodynamic Forces on a Rough Wall," Rev. Mod. Phys. Volume 21, 1949.

6. Francis, J., Pattanaik, A., and Wearne, S., "Observations of Flow Patterns Around Some Simplified Groyne Structures in Channels," Tech. Note 8, Proceedings, Institution of Civil Engineers, London, Dec. 1968.

7. Garde, R., Subramanya, K., and Nambudripad, K., "Study of Scour Around Spur-Dikes," Jour. of Hyd. Div., ASCE, Vol. 87, No. HY6, Nov. 1961.

8. Gill, M., "Erosion of Sand Beds Around Spur Dikes," Jour. of Hyd. Div., ASCE., Vol. 98, No. HY9, Sept. 1972.

9. Head, M. and Rochenberg, I., "The Preston Tube as a Means of Measuring Skin Friction," Jour. of Fluid Mechanics, Vol. 14, Part 1, 1962.

10. Hjorth, P., "Studies on the Nature of Local Scour," Dept. of Water Resources Engineering, University of Lund Bulletin, Series A, No. 46, 1975.

11. Hollingshead, A., "Boundary Shear Stress Distribution in Open Channel Flow," Ph.D. Thesis, University of Alberta, Dept. of Civil Engineering, Edmonton, Alberta, Spring 1972.

12. Hornung, H., and Joubert, P., "The Mean Velocity Profile in Three-Dimensional Turbulent Boundary Layers," Jour. of Fluid Mechanics, Vol. 15, Part 3, 1963.

13. Inglis, C., "The Behaviour and Control of Rivers and Canals," Research Publication 13, Parts 1 & 2, Central Waterpower, Irrigation and Navigation Research Station, Poona, India.

14. Izzard, C., and Bradley, J., "Field Verification of Model Tests on Flow Through Highway Bridge and Culverts," Proc. 7th Hydraulic Conference, Bulletin 39, Studies in Engineering, State University of Iowa, Iowa City, 1958.

15. Joglekar, D., "Manual on River Behaviour Control and Training," Publication No. 60, Central Board of Irrigation and Power, New Delhi, Sept. 1971.

16. Johnston, J., "On the Three-Dimensional Boundary Layer Generated by Secondary Flow," Trans. ASME Series D, Vol. 82, 1960.

17. Johnston, J.,Discussion of "Critical Review and Current Developments in Three-Dimensional Turbulent Boundary Layers," (Joubert, Perry and Brown), Fluid Mechanics of Internal Flow, Elsevier Publishing Company, Amsterdam, Netherlands, 1967.

18. Joubert, P., Perry, A., and Brown, K., "Critical Review and Current Developments in Three-Dimensional Boundary Layers," Fluid Mechanics of Internal Flow, Elsevier Publishing Company, Amsterdam, Netherlands, 1967.

19. Khosla, A., Bose, N., and Taylor, E., "Design of Weirs on Permeable Foundations," Publication No. 12, Central Board of Irrigation, New Delhi, Sept. 1936.

20. Lacey, G., "Stable Channels in Alluvium," Proc. of the Institution of Civil Engineers Paper No. 4736, Vol. 229, 1929.

21. Laursen, E., Discussion of "Study of Scour Around Spur-Dikes," (Garde et al) Proc. ASCE, Jour. of Hyd. Div., No. HY3, pg. 225, 1962.

22. Laursen, E., "An Analysis of Relief Bridge Scour," Jour. of Hyd. Div. Proc. ASCE Vol. 89, No. HY3, May 1963.

23. Liu, H., Chang, F., and Skinner, M., "Effect of Bridge Constriction on Scour and Backwater," Publication No. CER60HKL22, Civil Enginering Section, Colorado State University, Fort Collins, Colorado, Feb. 1961.

24. McMillan, F., "Experiments on Pitot Tubes in Shear Flows," Aeronautical Research Council Report and Memoranda No. 3028, 1957.

25. Melville, B., "Local Scour at Bridge Sites," Report No. 117, University of Auckland, School of Engineering, Sept. 1975.

26. Montes, J., and Ippen, A., "Interaction of Two-Dimensional Turbulent Flow with Suspended Particles," Report No. 164, Ralph M. Parsons Laboratory for Water Resources and Hydrodynamics, Dept. of Civil Eng. MIT, Jan. 1973.

27. Mukhamedov, A., Abduraupov, R., et al.,"Study of Local Scour and Kinematic Structure of Flow Around Solid and Through Spur-Dikes," Proc. IAHR, 14th Congress, Paris, Aug-Sept., 1971.

28. Nash, J., and Patel, V., "Three-Dimensional Turbulent Boundary Layers," SBC Technical Books, Sybucon Inc., Atlanta, Scientific and Business Consultants, 1972.

29. Nwachukwu, B., Gitzel, R., and Peterson, A., "An Application of Microcomputer in the Control, Measurement and Analysis of Hydraulic Testing," Proc. Specialty Conference on Computer Applications in Hydrotechnical Engineering, Toronto, Ontario, May 18-19, 1978.

30. Patel, V., "Calibration of the Preston Tube and Limitations on its Use in Pressure Gradients," Jour. of Fluid Mech., Vol. 23, Part 1, 1965.

31. Perry, A., and Joubert, P., "A Three-Dimensional Turbulent Boundary Layer," Jour. of Fluid Mech., Vol. 22, Part 2, 1965.

32. Peterson, A., "Bed Level Detection," Department of Civil Engineering Publication No. HY1978-E1, University of Alberta, 1978.

33. Preston, J., "The Determination of Turbulent Skin Friction by Means of Pitot Tubes," Jour. of Royal Aeronautical Society, Vol. 58, 1954.

34. Rajaratnam, N., and Berry, B., "Erosion by Circular Turbulent Wall Jets," Jour. of Hydraulic Research Vol. 15, No. 3, 1977.

35. Rajaratnam, N., and Muralidhar, D., "Yaw and Pitch Probes," Hydraulic Instrumentation Series, Dept. of Civil Engineering, University of Alberta, Edmonton, Alberta, Sept. 1967.

36. Rajaratnam, N., and Muralidhar, D., "Yaw Probe Used as Preston Tube," Tech. Note, the Aeronautical Journal of the Royal Aeronautical Society, Vol. 72, Dec. 1968.

37. Stratford, B., "The Prediction of Separation of the Turbulent Boundary Layer," Jour. of Fluid Mech., Vol. 5, Jan. 1959, Pg. 1.

38. Stratford, B., "An Experimental Flow with Zero Skin Friction Throughout its Region of Pressure Rise," Jour. of Fluid Mech., Vol. 5, Jan. 1959, Pg. 17.

39. Straub, L., "Effect of Channel Contraction Works Upon Regime of Moveable Beds," Transactions, American Geophysical Union, Part II, 1934.

40. Vallentine, H., "Applied Hydrodynamics," Butterworths Scientific Publications, London, 1967.

41. Zaghloul, N. and McCorquodale, J. "A Numerical Model for Flow Past a Spur-Dike," Proceedings, First Canadian Hydraulics Conference, Edmonton, May 1973.

42. Znamenskaya, N.S., "The Analysis and Estimating of Energy Losses by Instantaneous Velocity Distribution of Streams with Movable Bed," Proceedings, Intern. Assoc. For Hydraulic Research, Vol. No. 1, Paper A4, Colorado State University, 1967.

APPENDIX A

THEORETICAL FREE STREAM LINE THEORY

The flow near a model thin groyne may be compared to the flow through one half of a symmetical two-dimensional nozzle. The free stream line analysis for such flow could be performed by successive transformations as outlined by Vallentine (1967). Considering Figure A1, the successive transformations from the physical z-plane to a parallel flow from left to right, the so called w-plane are

$$\zeta = \frac{dz}{dw} = \left|\frac{1}{v}\right| e^{i\theta} \tag{1}$$

$$\zeta' = \ell n\ \zeta = \ell n \left|\frac{1}{v}\right| + i\theta \tag{2}$$

$$t = \text{Cosh}\ \frac{\pi}{\beta}\ (\zeta' + i\beta) \tag{3}$$

$$w = \ell n\left(\frac{t+k}{t+1}\right) \tag{4}$$

For the configuration of Figure A1, it can be shown that

$$k = \frac{e^{\ell n\left(\frac{\beta}{\pi}\right)^{\pi/\beta}} - e^{-\ell n\left(\frac{\beta}{\pi}\right)^{\pi/\beta}}}{2} \tag{5}$$

$$= \frac{\left(\frac{\beta}{\pi}\right)^{\pi/\beta} + \frac{1}{\left(\frac{\beta}{\pi}\right)^{\pi/\beta}}}{2} \tag{6}$$

If velocity is assumed constant along the free stream line (N to I), then $\zeta' = i\theta$ where θ varies from $-\beta$ to 0. Therefore,

$$t = \text{Cosh}\left[\frac{\pi}{\beta}\ i\theta + i\pi\right] = -\ \text{Cos}\left(\frac{\pi}{\beta}\ \theta\right) \tag{7}$$

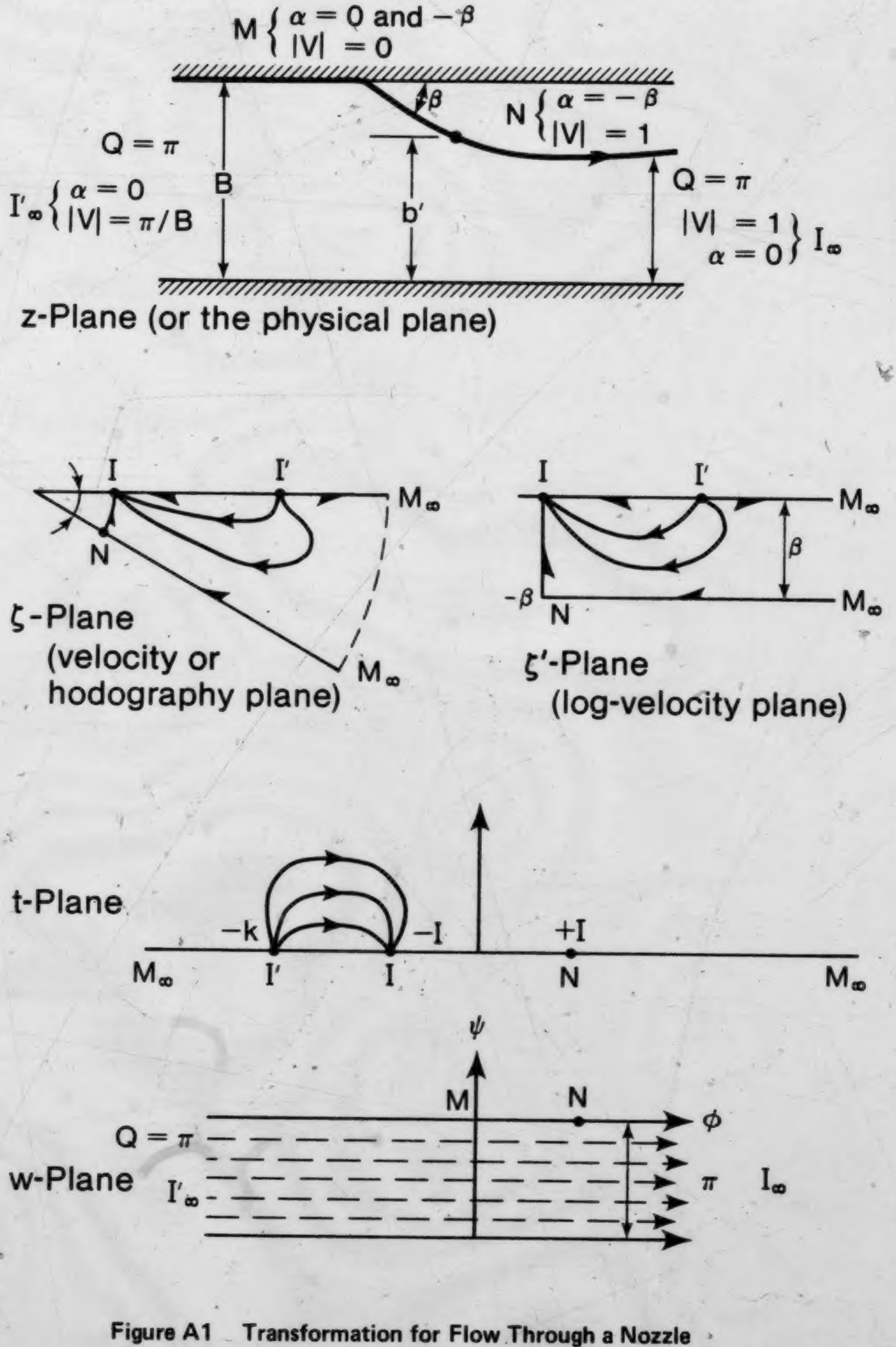
M { α = 0 and −β
|V| = 0
β
N { α = −β
|V| = 1
Q = π
I'∞ { α = 0
|V| = π/B
B
b'
Q = π
|V| = 1
α = 0 } I∞
z-Plane (or the physical plane)
I
I'
M∞
N
ζ-Plane
(velocity or
hodography plane)
M∞
I
I'
M∞
β
−β
N
M∞
ζ'-Plane
(log-velocity plane)
t-Plane
−k
−I
+I
M∞
I'
I
N
M∞
ψ
M
N
φ
Q = π
w-Plane
I'∞
π
I∞

Figure A1 Transformation for Flow Through a Nozzle

$$dt = \frac{\pi}{\beta} \text{Sin}(\frac{\pi}{\beta} \theta)\, d\theta \tag{8}$$

If s is the distance from the point of separation along the stream line, from potential flow theory

$$ds = dw = [\frac{1}{t+k} - \frac{1}{t+1}]dt \tag{9}$$

$$= \frac{\pi}{\beta} [\frac{1}{k-\text{Cos}(\frac{\pi}{\beta}\theta)} - \frac{1}{1-\text{Cos}(\frac{\pi}{\beta}\theta)}] \text{Sin}(\frac{\pi}{\beta}\theta)\, d\theta \tag{10}$$

$$dx = ds\, \text{Cos}\theta$$

$$= \frac{\pi}{\beta} [\frac{1}{k-\text{Cos}(\frac{\pi}{\beta}\theta)} - \frac{1}{1-\text{Cos}(\frac{\pi}{\beta}\theta)}] \text{Cos}\theta\text{Sin}(\frac{\pi}{\beta}\theta)d\theta \tag{11}$$

$$dy = ds\, \text{Sin}\theta$$

$$= \frac{\pi}{\beta} [\frac{1}{k-\text{Cos}(\frac{\pi}{\beta}\theta)} - \frac{1}{1-\text{Cos}(\frac{\pi}{\beta}\theta)}] \text{Sin}\theta\text{Sin}(\frac{\pi}{\beta}\theta)d\theta \tag{12}$$

From equations 6, 11 and 12 the theoretical free stream line could be obtained by numerical integration for any angle β of the groyne.

Sample Results

Figure A2 shows the computed free stream lines for five groyne angles. It can be seen that the stream lines are displaced into the main stream as the groyne angle increased from 30 degrees to 120 degrees. The computed streamlines for 120 and 150 degrees coincide. Therefore, for $b/B = 1/6$, optimum stream line displacement is obtained for 120

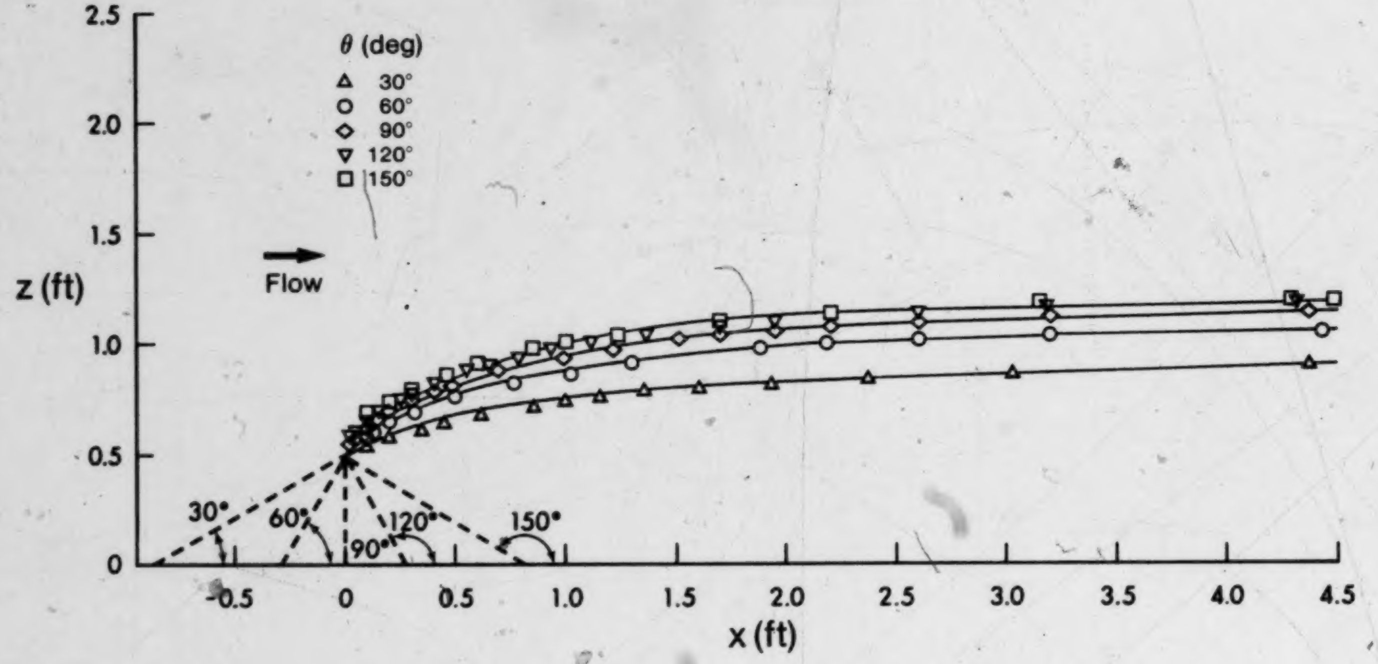

Figure A2 Theoretical Free Stream Lines

degree groyne.

In practice, a groyne pointing downstream is referred to as "attracting" groyne. Similar terms for groynes pointing upstream and perpendicular to the bank are "deflecting" and "repelling" respectively. From Figure A2 it is obvious that this terminological demarcation has no basis since the stream line changes continuously from a lower angle (downstream pointing groyne) to a higher angle (upstream pointing groyne).